Computational Approaches for Segmenting Cartilage Morphology and Simulating Knee Joint Contact Pressure during Human Walking

by

Kwang Won Choi

A dissertation submitted in partial fulfillment of

the requirements for the degree of

Doctor of Philosophy

(Mechanical Engineering)

At the

UNIVERSITY OF WISCONSIN-MADISON

2014

Date of final oral examination: May 6th 2014

The dissertation is approved by the following members of the Final Oral Committee:

Darryl G. Thelen, Professor, Mechanical Engineering, Biomedical Engineering
Heidi-Lynn Ploeg, Associate Professor, Mechanical Engineering, Biomedical Engineering
Dan Negrut, Associate Professor, Mechanical Engineering
Krishnan Suresh, Associate Professor, Mechanical Engineering
Richard Kijowski, Associate Professor, Radiology
Joseph Towles, Assistant Scientist, Mechanical Engineering

Acknowledgements

I would like to express my thanks to the following people for their support through the course of my study.

First, I would like to thank my advisor, Professor Darryl Thelen, for his guidance, help and patience during the journey of this project. Without his support, the work could not have been accomplished. I would also like to express my gratitude and appreciation to all my committee members: Professor Heidi-Lynn Ploeg, Professor Dan Negrut, Professor Krishnan Suresh and Professor Richard Kijowski. My thanks extend to all professors and colleagues at UW-Madison, particularly to Professor Vadim Shapiro, Dr. Chiwa Song, Dr. Joseph Towles and Dr. Jason Franz. I would also like to thank all the lab colleagues, former and present: Jarred Kaiser, Laura Slane, Carrie Francis, Fang Liu.

Second, I want to give my special thanks to my family for their unconditional love. I thank them for supporting me all the time, so I could finish this study because of their help and love.

Finally, I would like to thank my God, who always guides me in the right direction. Financial support for this study was provided by the National Institutes of Health (grant #AR062733) and National Science Foundation (grant # 0966535).

Abstract

Cartilage morphology is both an indicator of tissue health, and an important biomechanical determinant of internal joint mechanics. However, direct measurement of cartilage morphology and joint loading is not feasible. Thus, it is necessary to develop computational imaging and modeling tools to investigate the relationship between cartilage morphology and knee mechanics during human movement. Such tools are relevant clinically for tracking changes in morphology that can arise secondary to injury, surgical treatment and rehabilitation. Further, computational biomechanical modeling tools are beneficial in research for predicting the influence that interventions can have on joint loading patterns. The overall goal of this work was to develop, validate and use new computational approaches to accurately characterize in vivo cartilage morphology from MRI images and simulate tibiofemoral cartilage loading patterns during human walking. This goal was achieved by completing the following four objectives.

Objective 1. Develop an Accurate and Repeatable Semi-Automated Segmentation Algorithm for Reconstructing Articular Cartilage Morphology from Magnetic Resonance Images

Cartilage morphology is a vital indicator of tissue health. For example, in osteoarthritis, cartilage tissue is observed to undergo thickening in the early stages of the disease followed by thinning in the later stages. Advances in magnetic resonance (MR) imaging sequences can be used to obtain high resolution images of cartilage morphology that

are useful for assessing subtle changes in cartilage thickness. However, segmenting out the entire cartilage volume from stacks of images remains a time-consuming task due to the inherent challenge in automatically identifying tissue boundaries. Further, the anatomical accuracy and repeatability of 3D cartilage models based on manual segmentation have been questioned. We introduce a semi-automated cartilage segmentation algorithm for creating 3D cartilage geometry models from MR images within a few seconds. The algorithm first uses region growing to segment out the bone tissue, edge detection to delineate tissue boundaries and then a novel radial projection scheme to identify the inner and outer surface of the cartilage. This sequence is repeated across a stack of MR image slices, resulting in a 3D reconstruction of the entire cartilage volume. We validated the segmentation algorithm by showing it produced unbiased porcine knee cartilage thickness estimates that were within 0.4mm of direct cartilage thickness measures obtained via a laser scanner. The segmentation algorithm was also successfully used to segment tibia and femoral articular cartilage surfaces from MR images collected on human subjects. Good computational performance was achieved with the automated algorithm requiring a couple orders of magnitude less time than a manual segmentation approach.

Objective 2. Introduce a Computationally Efficient Collision Detection Algorithm to enable the Calculation of Complex Cartilage Contact Pressure Patterns within Biomechanical Simulations of Movement

The location and magnitude of knee joint articular contact pressure are important factors that can affect the long-term health of cartilage tissue. The objective of the study was to develop a computationally efficient discrete element analysis (DEA) algorithm that would allow for surface pressure to be computed based on the depth of penetration between two articulating elastic surfaces. The primary computational challenge in using DEA with complex geometries involves determining the regions of surface overlap, a process that involves finding the face on a target surface that is intersected by a ray cast from a face on the parent surface. We accelerated the collision detection process by using a hierarchical bounding volume approach, in which the target surface was successively subdivided into regions that fit within tight fitting bounding boxes. Ray-box intersection tests then allowed us to quickly traverse the surface and identify the leaf node containing the triangle intersected by a ray. The parallelized algorithm was subsequently implemented on a graphics processor unit (GPU), providing nearly 10 fold increase in computation speed when high resolution cartilage surface meshes were used. The collision detection algorithm was shown to be sufficiently fast to enable simulations of tibiofemoral contact loading patterns within a multibody dynamic simulation of walking.

Objective 3. Investigate the Accuracy of Simulated Tibiofemoral Contact Loads Obtained via the Co-Simulation of Neuromuscular Dynamics and Knee Mechanics

This study introduced a framework for co-simulating neuromuscular dynamics and knee joint mechanics during gait. A knee model was developed that included 17 ligament

bundles and a representation of the distributed contact between a femoral component and tibial insert surface. The knee was incorporated into a forward dynamics musculoskeletal model of the lower extremity. A computed muscle control algorithm was then used to modulate the muscle excitations to drive the model to closely track measured hip, knee, and ankle angle trajectories of a subject walking overground with an instrumented knee replacement. The resulting simulations predicted the muscle forces, ligament forces, secondary knee kinematics, and tibiofemoral contact loads. Model-predicted tibiofemoral contact forces were of comparable magnitudes to experimental measurements, with peak medial (1.95 body weight (BW)) and total (2.76 BW) contact forces within 4–17% of measured values. Average root-mean-square errors over a gait cycle were 0.26, 0.42, and 0.51 BW for the medial, lateral, and total contact forces, respectively.

Objective 4. Investigate the Influence of Cartilage Thickness on Simulated Tibiofemoral Contact Pressure Patterns during Normal Human Walking

Cartilage has a spatially varying micro- and macro-structural arrangement that is well adapted to the loading seen in vivo. It is believed that injury- and surgery-induced changes in knee mechanics may disrupt this loading and subsequently lead to cartilage thinning. This degenerative process may be cumulative, with changes in cartilage morphology affecting tissue loads in a way that exacerbates the problem. This pilot study was undertaken to investigate the influence that cartilage thickness can have on cartilage pressure patterns in human walking. Gait simulations were performed with

combined tibiofemoral cartilage thickness ranging from 2 to 10 mm. Peak tibia plateau contact pressures increased nonlinearly with cartilage thinning, with a 51% increase in pressure predicted in the thin cartilage condition (2mm of total contact cartilage thickness) compared to the nominal cartilage model (6mm of total contact cartilage thickness). As a result, net contact areas decreased substantially with cartilage thinning, by 43% in the thin cartilage condition relative to the nominal condition.

The computational tools developed in this study will enable future investigations of cartilage loading on heterogenous cartilage thickness maps derived from images on individual subjects. Such studies are important for understanding and treating biomechanical factors that can contribute to cartilage tissue degeneration.

Table of Contents

List of Figures

List of Tables

Chapter 1: Introduction

The knee joint is one of the largest and most complex joints in the human body (Kulowski 1932) (Figure 1) (Figure 2). The knee joint joins the femur with the tibia and the patella and consists of two articulations: the tibiofemoral joint and the patellofemoral joint (Elaine N. Marieb 2008). Soft tissues connect the knee bones to the muscles around the knee that move the joint and provide stability to the knee (Elaine N. Marieb 2008). The anterior cruciate ligament (ACL) restrains excessive forward movement of the tibia in relation to the femur and also it limits excessive tibial rotation and acts as a secondary restraint to both valgus and varus stresses (Liu-Ambrose 2003) (Figure 3) (Figure 4). The posterior cruciate ligament (PCL) prevents the posterior dislocation of the tibia in relation to the femur (Kannus, Bergfeld et al. 1991) (Figure 4) (Figure5). The medial and lateral collateral ligaments (the fibular collateral ligament and the tibial collateral ligament) prevent the femur from sliding from side to side (Gardiner, Weiss et al. 2001) (Figure 5)

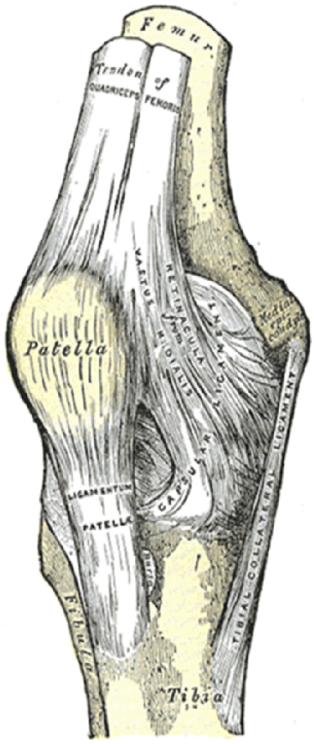

Figure 1. Right knee-joint. Anterior view. (Gray 1918)

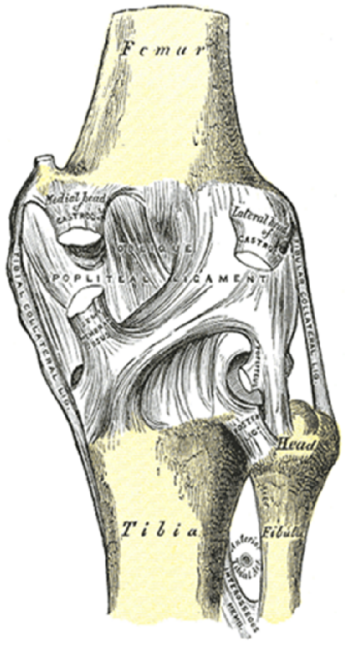

Figure 2. Right knee-joint. Posterior view. (Gray 1918)

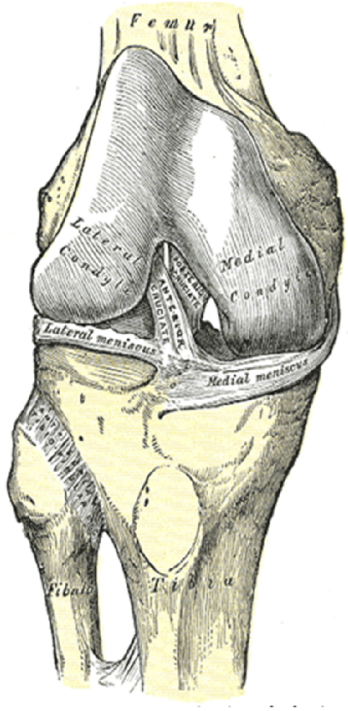

Figure 3. Right knee-joint, from the front, showing the Anterior Cruciate Ligament . (Gray 1918)

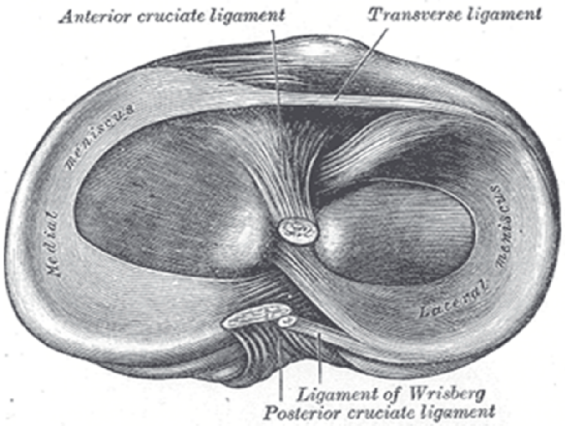

Figure 4. Head of right tibia seen from above, showing the Anterior Cruciate Ligament and the Posterior Cruciate Ligament . (Gray 1918)

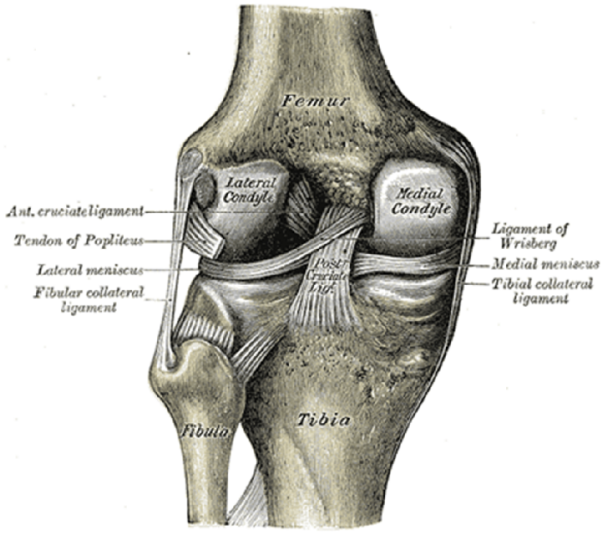

Figure 5. Left knee-joint from behind, showing the Posterior Cruciate Ligament, the Tibial Collateral Ligament and the Fibular Collateral Ligament . (Gray 1918)

Acute anterior cruciate ligament (ACL) ruptures are most often sustained by young, physically active individuals. It is estimated that there will be more than 100,000 ACL tears in the United States each year (Frank and Jackson 1997). ACL reconstruction surgery often results in reliable ligamentous stability permitting patients to recover to a normal level of joint function in the short term, up to 5 years (Otto 1998; Spindler, Warren et al. 2005), and little problem is reported in the intermediate term, ranging 5~9 years (Bach, Tradonsky et al. 1998). However, many cases of abnormal articular cartilage morphology have been observed over longer time frames, with 48% of cases exhibiting evidence of knee osteoarthritis (OA) within 5–20 years after the initial ACL injury (Lohmander, Englund et al. 2007; Louboutin, Debarge et al. 2009). Altered knee biomechanics in the post-operative knee can be expected to yield abnormal cartilage loading patterns across the knee joint with long-term changes in dynamic loading, which may contribute to the prevalence of early OA in this population (Lohmander, Englund et al. 2007).

From a clinical application perspective, there are presently no feasible methods for assessing how ACL reconstruction surgery will change *in vivo* biomechanics of the knee during the gait cycle, despite the significance to clinicians and patients. Since *in vivo* direct measurement of the human knee is not clinically feasible, gait simulation is considered a useful measuring tool to indirectly assess dynamic loads on the joint (Shakoor and Moisio 2004). Analyzing knee biomechanics during functional activity can offer fundamental understanding of daily repetitive loads applied to the knee joint and it can provide insight into the pathogenesis of knee OA.

There has been substantial speculation about the relationship between *in vivo* tissue mechanics, specific gait alterations after ACL construction surgery and the development of OA at the knee joint (Andriacchi, Briant et al. 2006). Computational models provide an appropriate framework for studying such links, by providing a cause-effect relationship between joint morphology, muscle loading and cartilage pressure. There are two major challenges to constructing subject-specific computational models that contain anatomical details necessary to simulate cartilage pressure. First, it is computationally expensive, as the model contains enormous amounts of information from the fine meshes of contact surfaces of the knee joint developed from the high resolution of MR images and variations of soft tissue conditions. One approach to this challenge is parallel computation, which is an emerging computational technique in which many calculations are launched concurrently, working on the principle that the computation of enormous amounts of data can often be distributed into multi-cores, which are then solved simultaneously (Almasi and Gottlieb 1989). Second, to build a more realistic computation model, we will construct the 3D model from subject specific three-dimensional cartilage

volumes created from MR images (Kaiser, Bradford et al. 2012). Generally, 3D geometry is manually segmented from MR images, which is time-consuming and may lead to inaccuracies from the manual work. To build an accurate and efficient computational model, a semi-automated segmentation algorithm has been developed. Using these computational frameworks, the investigation of the interrelationship of cartilage morphology and knee mechanics became feasible.

Chapter 2: Background

2-1. Knee Cartilage and Osteoarthritis

The specific causes of early OA in patients with ACL reconstruction remain unknown in spite of the great number of empirical investigations over the past several decades. The prevailing theory is that early OA may develop due to a change in cartilage loading resulting from abnormal kinematics after ACL reconstruction surgery. Generally, knee cartilage has been known to be mainly self-modified to the continual loading that occurs during the gait cycle. The region of cartilage subjected to high compressional stress is relatively thicker than normal cartilage tissue (Kiviranta, Jurvelin et al. 1987) and it demonstrates more random collagen fiber orientations (Figure 6) (Bullough, Yawitz et al. 1985; Clark 1991; Appleyard, Burkhardt et al. 2003; Chaudhari, Briant et al. 2008), while the region under tensional stress is thinner, with tangentially oriented collagen fibers at the surface (Figure 6) (Bullough, Yawitz et al. 1985; Eggli, Hunziker et al. 1988; Little and Ghosh 1997; Quinn, Hunziker et al. 2005; Chaudhari, Briant et al. 2008). These suggest that cartilage reacts and adapts to the loading environments.

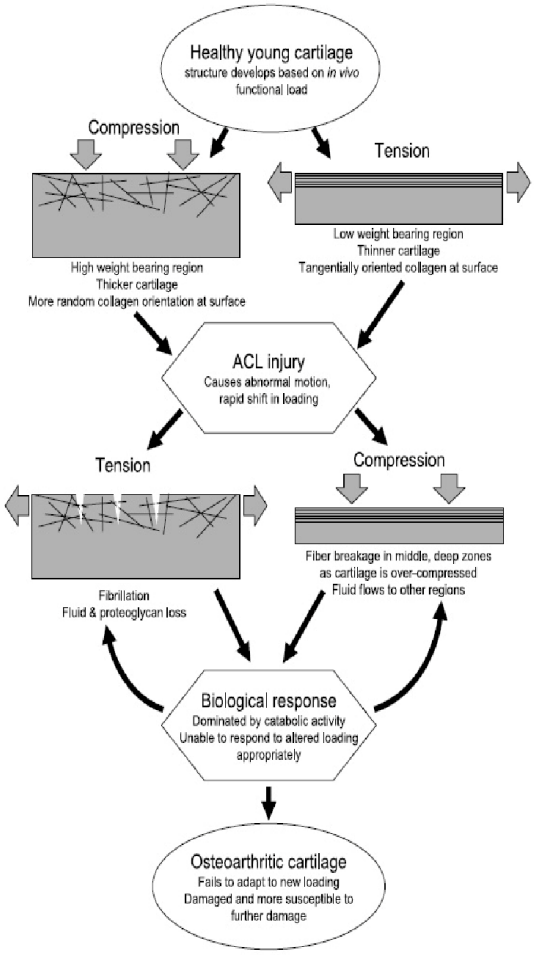

Figure 6. (Upper Left) Normal cartilage under high compressional stress, (Upper Right) Normal cartilage under low compressional stress or tensional stress, (Lower Left) Abnormal tensional stress on cartilage, (Lower Right) Abnormal compression stress on cartilage (Chaudhari, Briant et al. 2008)

There are important differences in the tibiofemoral kinematics of ACL damaged knees during the gait cycle compared to the uninjured healthy knees (Georgoulis, Papadonikolakis et al. 2003; Andriacchi and Dyrby 2005). Researchers have compared the contact points on the surfaces of the tibial plateau of ACL damaged knees to healthy

knees. The ACL reconstruction surgery may result in a shift in which areas of the cartilage are in contact (Figure 7) (Li, Moses et al. 2006).

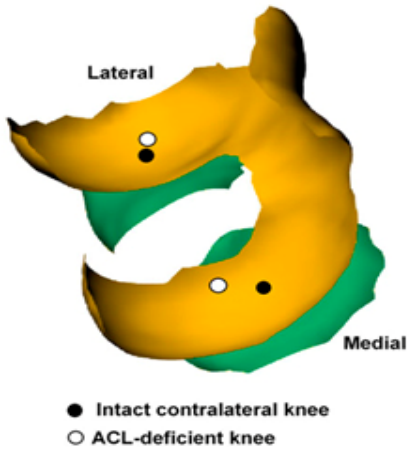

Figure 7. Difference in contact point between healthy knee and ACL-deficient knee (Li, Moses et al. 2006)

This shift likely causes increased compressional loading in areas not conditioned to frequent load bearing, as well as reduced loading in areas conditioned to frequent load bearing or regions that were previously subjected to compression become subjected to tension (Figure 6) (Chaudhari, Briant et al. 2008). Cartilage tissue may fail to adapt to the new loading pattern and this could lead to the initiation of OA.

Since the ACL provides the main anterior and rotational stability to the knee joint (Markolf, Graff-Radford et al. 1978; Shoemaker and Markolf 1982; Kanamori, Zeminski et al. 2002), there are ongoing studies about the contribution of ACL to knee kinematics in gait. The evidence of abnormal internal-external rotation of the tibia with respect to the

femur in ACL-deficient and reconstructed knees has been demonstrated in the literature. For example, ACL-deficient knees were more internally rotated (Georgoulis, Papadonikolakis et al. 2003) while reconstructed knees were more externally rotated (Tashman, Collon et al. 2004). ACL reconstruction has not been capable of correcting this abnormality in walking, which is more demanding during running (Stergiou, Ristanis et al. 2007). Also, an internal rotational offset of 5° in the ACL-deficient knee caused a higher rate of cartilage loss (44% increase in loss) than the normal knee with ACL and zero rotation in the loading on the knee. This shows the necessity of correcting for rotational motion during ACL reconstruction surgery (Andriacchi, Briant et al. 2006).

2-2. Recent trends in ACL reconstruction surgery

ACL reconstruction is surgery aimed at replacing the anterior cruciate ligament (ACL), which is located in the center of the knee joint, with a new graft. The ACL keeps the tibia in a fixed position and provides the main anterior and rotational stability of the knee joint (Markolf, Graff-Radford et al. 1978; Shoemaker and Markolf 1982; Kanamori, Zeminski et al. 2002). A rupture of this soft tissue can cause the limb to fail its function during ambulation. The tissue replacement is typically either an allograft from a donor or an autograft from the patient's own body. The two most common regions to harvest the soft tissue from are the patella tendon or the hamstring tendon. The surgical process is typically completed by knee arthroscopy. With arthroscopy, a small medical camera is inserted into the knee joint through a tiny surgical cut. Arthroscopy is a minimally invasive surgical procedure to check the ligaments and other tissues of the knee during surgery.

Then, the surgeon will make other small cuts around the knee joint and insert the other medical instruments. The surgeon will fix any other injury found, and then will restore the ACL by the following procedures:

- The torn soft tissue will be detached with a medical shaver or similar medical instruments (Fu, Bennett et al. 2000).
- If an autograft is chosen to build a new ligament, a larger cut needs to be made. Then, soft tissue from either the patella tendon or the hamstring tendon will be removed through the larger cut (Fu, Bennett et al. 2000).
- The surgeon will make tunnels in the femur and tibia to bring the graft through (Howell and Barad 1995; Fu, Bennett et al. 1999; Fu, Bennett et al. 2000) (Figure 8).

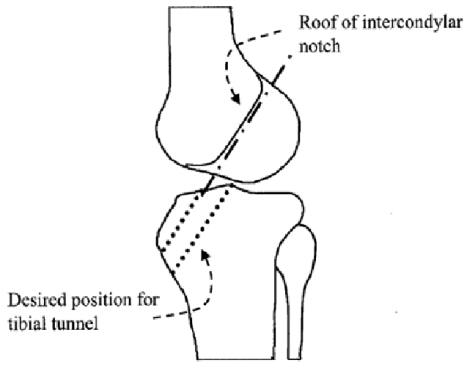

Figure 8. Tunnels in femur and tibia (Fu, Bennett et al. 1999)

This new ligament will be placed in the center of the old knee tissue. The location of the new graft is the most significant surgical factor during reconstruction since it has a direct

influence on the mechanics of the limb during the gait (Beynnon, Johnson et al. 2005). Specifically, the angle of the tunnel decides the position of the inserted graft. This tunnel is usually located using a clock-face reference of orientation (Loh, Fukuda et al. 2003) (Figure 9). The graft tunnel is normally drilled between the 10 and 11 o'clock direction in the right limb, from the tibia to the femur.

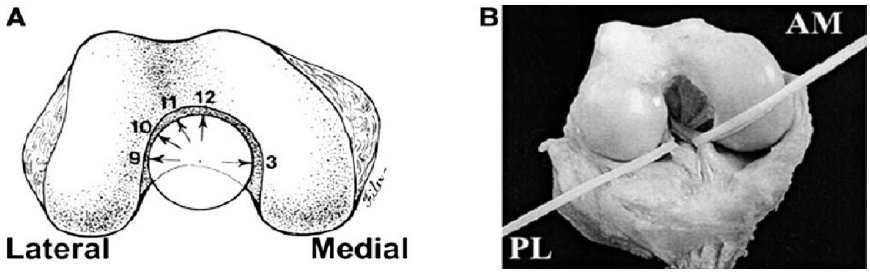

Figure 9. A.Clock-face reference of orientation of tunnel, B. Photograph of the separated ACL bundles, AM and PL (Loh, Fukuda et al. 2003)

- The surgeon will fasten the graft to the femur and tibia with titanium screws or other fixation device to hold it in a static location. As it recovers, the tunnel structures in the femur and tibia will fill in with osteons. Finally, the tunnel could secure the reconstructed ACL tissue (Fu, Bennett et al. 1999) (Figure 10).

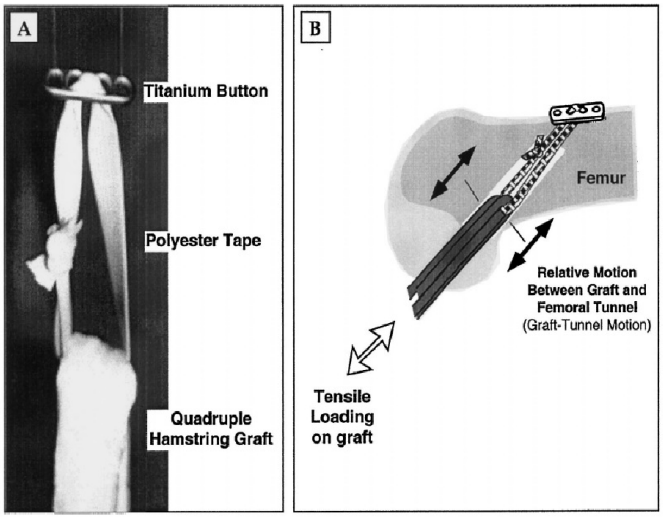

Figure 10. A. a titanium button-polyester tape construction for soft tissue fixation. B. a schematic diagram illustrating longitudinal graft tunnel motion, or the bungee effect (Fu, Bennett et al. 1999)

2-3. Generating dynamic gait simulations

Dynamic gait simulation using a musculoskeletal model is a useful methodology to investigate how muscles, bones and articular joints interact to produce functional movement. Especially, it is powerful when the investigator needs to isolate specific parameters such as the ACL tunnel angles or the ligament's stiffness and observe the consequences. It provides capabilities of investigation when experimental methods are limited (i.e. incapability of in vivo measurements) (Thelen, Anderson et al. 2003).

2-4. Outline of Dissertation

The following chapters contain studies that address some of the computational challenges in generating models of subject-specific cartilage morphology (Chapter 3),

computing articular contact pressure between articular surface models (Chapter 4) and simulating tibiofemoral contact loads within the context of gait (Chapter 5). Finally, we demonstrate the use of these computational tools to investigate the relationship between cartilage thickness and cartilage pressure patterns in human walking (Chapter 6).

Chapter 3: Semi-Automated Segmentation Algorithm for Reconstructing Articular Cartilage Morphology from MR Images

3-1. Introduction

Cartilage composition and morphology are important indicators of the development and progression of osteoarthritis (OA) (Andriacchi, Mundermann et al. 2004; Andriacchi, Briant et al. 2006; Tashman, Kopf et al. 2008; Lin, Walter et al. 2010). Currently, plane film radiographs are often used in the diagnosis of late stage knee osteoarthritis. However, standard x-ray technology can only identify cartilage thinning in the late stages of the disease. Magnetic resonance (MR) images provide a higher resolution alternative that is better able to assess early changes in the 3D geometry of knee cartilage(Eckstein, Cicuttini et al. 2006). In addition, newer quantitative MR sequences (T1-rho mapping, T2-mapping) can be used as biomarkers of cartilage composition. For example, abnormal values of T1-rho and T2 have been observed in patients who develop OA one year after knee ligament injury (Li, Kuo et al. 2011). These early signs of OA occur much earlier than changes in cartilage thickness, which generally are not observable until later stages of the disease.

In practice, it remains challenging to segment the 3D cartilage tissue regions in MR images. Segmentation is important for measuring cartilage thickness over the entire articulating surface. The segmented cartilage also serves as a mask for identifying cartilage regions where quantitative image metrics (T1-rho, T2) should be extracted. Traditionally, this is done by having end users scroll through stacks of images and

manually identify cartilage tissue. The problem is that manual cartilage segmentation is an extremely time-consuming process. Furthermore, the precision of the cartilage volume developed based on this method has been questioned because the efficiency and repeatability of the segmentation are based on the level of human expertise (Yushkevich, Piven et al. 2006). As a result, clinical use of MRI for diagnosing early stage OA is not seen in practice.

The objective of this study was to develop a novel semi-automated, repeatable and time-effective algorithm to construct 3D geometries from high resolution 3D MR images. The proposed approach consists of two major image processing techniques: boundary-based methods that rely on the analysis of the energies of image pixels to delineate an outline of the region of interest (ROI) from a possibly noisy 2D image, and region-based methods that rely on the analysis of the homogeneity of a spatially localized region to divide the image region into several classes or clusters. The novelty of the proposed algorithm comes from the integration of boundary-based methods with a region-based approach. The purpose of this study was to measure the accuracy of our cartilage segmentation algorithm by comparing the results to that obtained by laser scanning. Secondarily, we aimed to determine its repeatability by comparing the results from different MR sequences.

3.2. Methods

3.2.1 MR imaging

Three porcine knees were used to evaluate the accuracy of an algorithm used to segment cartilage geometry. All three porcine knees were scanned using a 3.0T MR scanner, (Discovery MR750, GE Healthcare, Waukesha, WI) using an 8-channel phased-array extremity coil (InVivo, Orlando, FL) and two separate imaging sequences. A three-dimensional FSE Cube sequence was acquired for whole knee cartilage segmentation with TR/TE=1600/28ms, 14cm field of view, 384 x 384 matrix, interpolated (zero filled) to 512 x 512 matrix, 80 slices with 1mm slice thickness. A three dimensional IDEAL-SPGR sequence was also applied with minimum possible TR of 8.6ms and three TEs of 4.2, 5.0 and 5.8ms, 14cm field of view, 384 x 384 matrix, interpolated (zero filled) to 512 x 512 matrix, 80 slices with 1mm slice thickness. After the second and third porcine knees were scanned for the first time, they were re-positioned and rescanned to allow for repeatability studies. By comparing the geometries obtained from the two scans, we can assess the repeatability of the segmentation algorithm. The repeatability of both the FSE Cube and the IDEAL SPGR were tested. Next, five healthy human subjects' knees were scanned and the resulting MR images were segmented using the same approach. This study was approved by the Wisconsin Health Sciences Institutional Review Board. Five healthy male subjects (average height: 175.7cm, weight: 72.56 kg, age: 32.6 years old) participated after providing informed consent. These were used to measure the time performance of semi-automated segmentation on human knee MRI scans. Each subject's knee was scanned using both FSE Cube and IDEAL SPGR sequences. By measuring the segmentation time per MR slice, we can assess the performance of this algorithm and its feasibility for clinical use.

3.2.2 Semi-automated segmentation algorithms

MR images were segmented using custom Matlab (The MathWorks, Natrick, Massachusetts, U.S.) code and the following the semi-automated segmentation method to construct 3D models.

Step 1. Segment out the bone tissue (pre-processing)

Discriminating cartilage from bone was an important first step. A geodesic active contours method was used to identify the bone area in each sagittal image stack. Geodesic active contour is a boundary-based image segmentation technique (Caselles, Kimmel et al. 1997). The user first draws an initial rough outline named “initial contour” and the algorithm determines whether the neighboring pixels should be added to the initial contour. If the pixel energies of the neighboring pixels are similar to the seed contour, the contour grows from the initial selection. The process is then iterated until it meets the boundary between bone and cartilage. By using this method, we can select and clear out the region of bone in an MR image so that detection of the cartilage boundary can be improved (Figure 11).

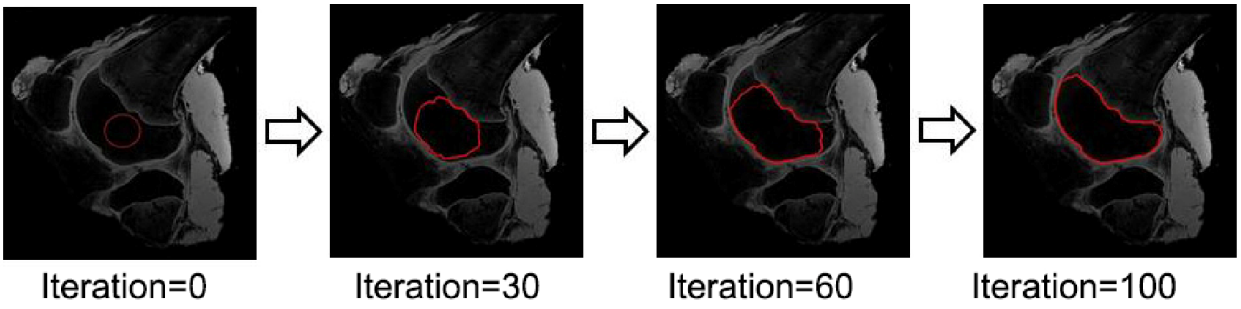

Figure 11. Geodesic Active Contours Method to identify the bone area in each sagittal image stack.

If any noise remains around the cartilage boundary, a fuzzy C-mean Method (FCM) (Ahmed, Yamany et al. 2002; Nock and Nielsen 2006) can be applied to remove it, and will effectively sharpen the boundary (Figure 12).

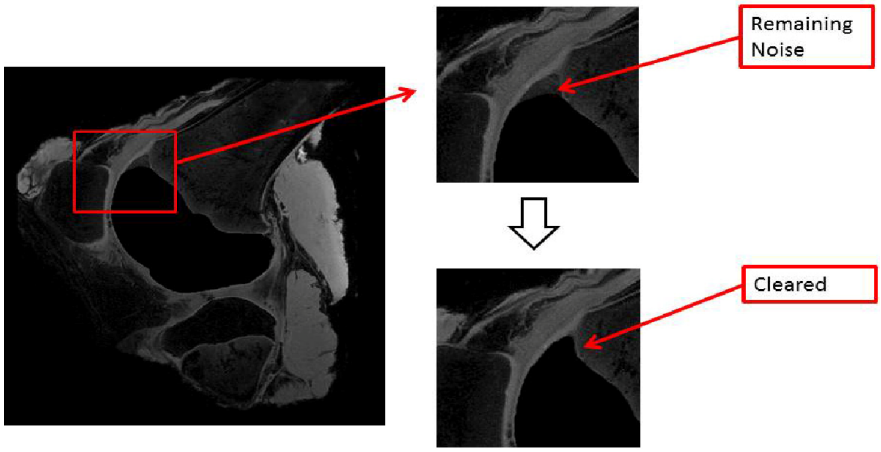

Figure 12. Fuzzy C-mean filter to remove the noise around cartilage boundary

FCM is one of the region-based image segmentation methods that relies on data clustering based on the analysis of the homogeneity of the image pixel values. Image data clustering is the process of dividing image pixels into several classes or clusters so that pixels in the same categorized class are as similar as possible, and pixels in different classes are as dissimilar as possible (Nock and Nielsen 2006). The FCM algorithm allows discriminating of the cartilage region and the remaining noise near the cartilage-bone interface, clearly.

The noise removal process was done semi-automatically throughout all slices in the MR images (Figure 13). The algorithm only requires user interaction three times. For

the example of femoral cartilage segmentation, the user needed to select one point at the center of the femoral bone region in the beginning of the 2D sagittal image slice where the femoral cartilage first appeared, another point in the mid-slice between the two femoral condyles, where the anterior cruciate ligament (ACL) was found, and then the other point in the end of the femoral cartilage slice where the last slice of the femoral cartilage was found (Figure 14).

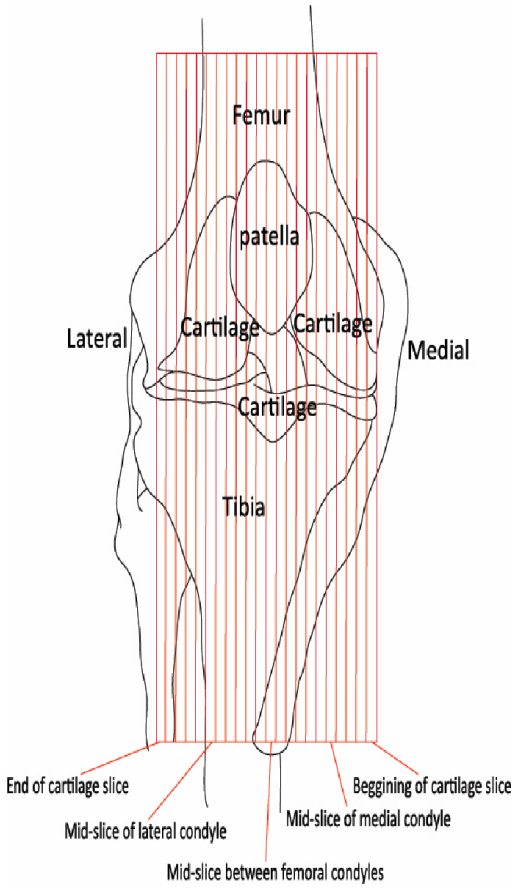

Figure 13. Sagittal image stack of knee MRI

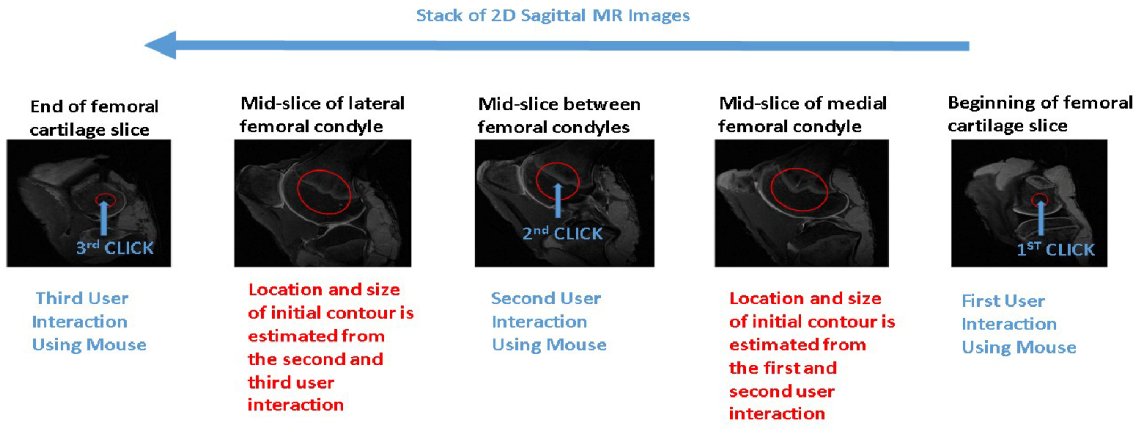

Figure 14. User interaction to set initial contours through sagittal image stack of right porcine knee MRI

Based on the first, second and third mouse click points at the centers of the bony regions in the femur, the algorithm set small initial contours, the sizes of which were slightly smaller than the bony regions in the 2D images. Then, the algorithm found the mid-slices of the medial and lateral condyle based on the slice index numbers of the beginning slice, the mid-slice between the two femoral condyles and the end slice. The center locations and the sizes of the initial contours in the mid-slices of the medial and lateral condyle were estimated from the center locations and the sizes of the contours from the aforementioned three slices (Figure 14). Finally, the center locations and the sizes of the initial contours in the slices between the beginning slice and the mid-slice of the medial condyle were linearly calculated based on the information of the two slices and the initial contours were placed in each slice between the two, respectively. In a similar fashion, the contours in the slices between the mid-slice of the medial condyle and the mid-slice of the two femoral condyles, between the mid-slice of the two femoral condyles and the mid-

slice of the lateral condyle and between the mid-slice of the lateral condyle and the end slice were calculated and placed, respectively.

Step 2. Edge detection

The Canny edge detection technique (Canny 1986) is a boundary-based image segmentation technique which aims at recognizing points, lines or regions in a digital image at which the pixel intensity changes suddenly, or more formally, has discontinuities. The regions at which image pixel intensity changes suddenly are usually organized into a set of curved line segments or edges. Edge detection is an essential algorithm in digital image processing, mostly in the area of feature recognition. We utilize this image processing method to detect cartilage regions from an MR image. This method can be used to capture changes in material properties because the region of collagen that constructs cartilage is brighter than any other tissue due to its higher proportion of water (Canny 1986; Lim 1990; Parker 1997) (Figure 15).

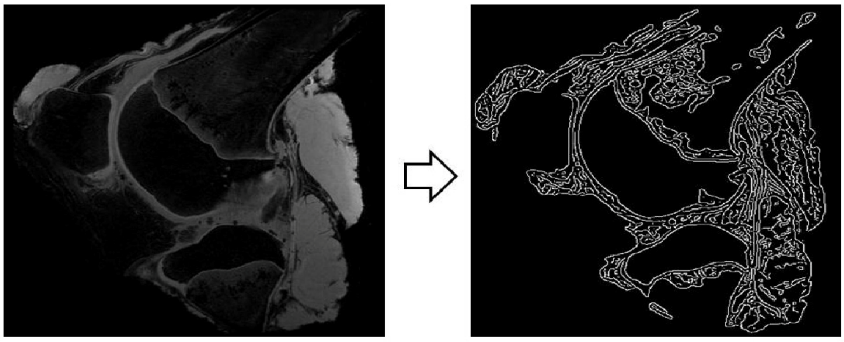

Figure 15. Edge detection

Step 3. Detection of cartilage boundary using radial line casting

The user is asked to select three points on each sagittal MR image of the knee (Figure 16): the start point of cartilage in the most anterior region (Figure 16, P1), the center point of bone (Figure 16, P2), and the end point of cartilage in the most posterior region (Figure 16, P3). Based on the three points, a large sector will be created. This large sector is equally divided into smaller parts with each division terminating in a new point (Figure 16, P4, P5 and P6). The number of divided sectors can be chosen by the user. Larger numbers of divisions will provide higher resolution but will slow down the detection process. We then track changes in pixel intensity along these lines and detect the non-zero pixel values. (The edge detector converts gray scale MR images to black and white images and the black pixel has 0 value while the white pixel has 1 value.) These will be selected as the locations of cartilage inner and outer boundaries (Figure 17). If detection is not well done, user can manually correct incorrect detection of boundaries.

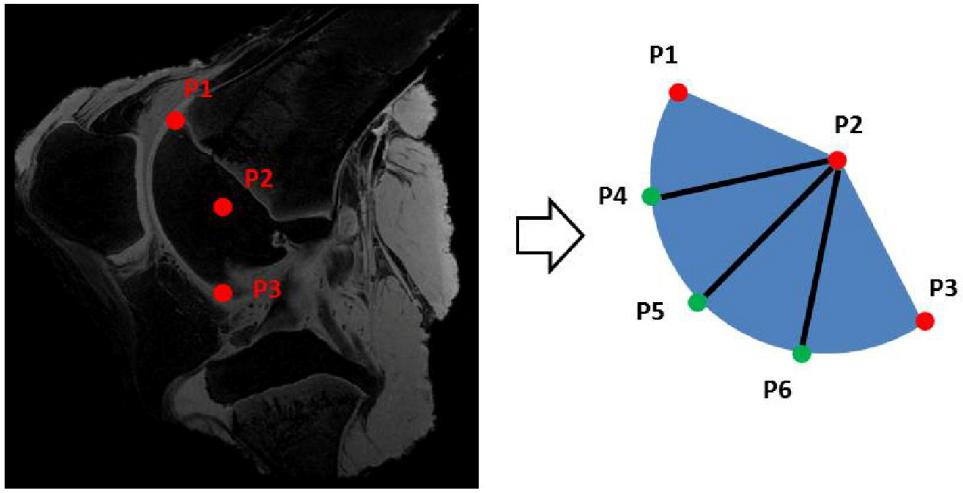

Figure 16. Selection of 3 points to choose the start point, pivot point and end point of image profiler

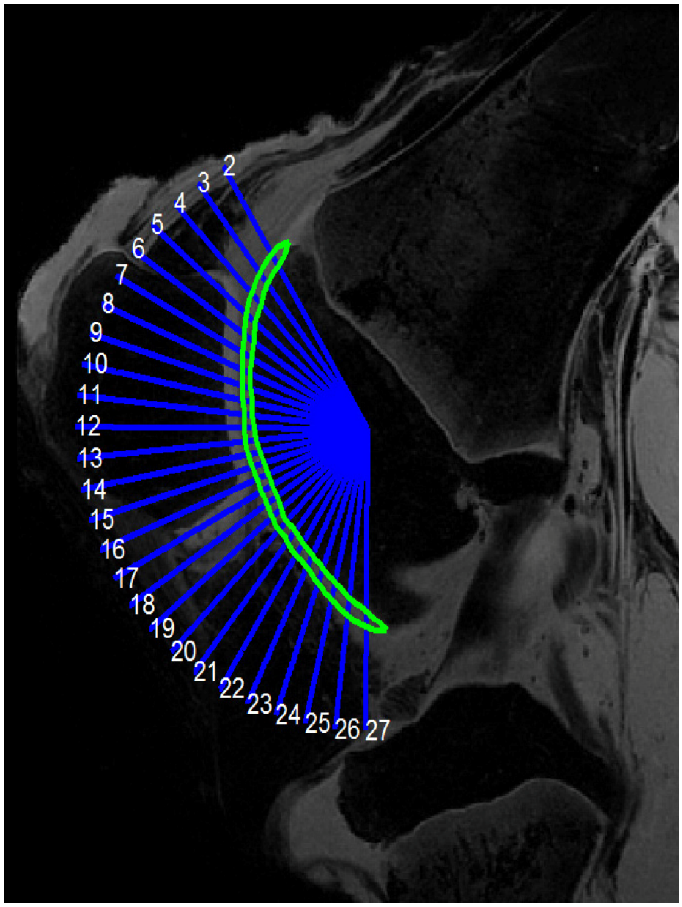

Figure 17. Cartilage Detection

Step 4. Reconstruct the cartilage volume

Finally, the algorithm draws a closed curve from the detected boundary points to make the outline of the cartilage (Figure 17). Detected cartilage boundaries on the stack of 2D images form a series of contours in 3D space and then the algorithm explores the pixel data in each 2D image to find pixels near a contour in each slice. Once these pixels are found, the x and y coordinates of points can be extracted based on the locations of these pixels in each 2D image and the z coordinates can be extracted based on the slice thickness and slice indices. After the coordinates of these 3D points are extracted, the 3D points are then connected into surfaces and called isosurfaces. The reconstructed isosurfaces can be patched into 3D triangular meshes, and then the meshes can be expressed as lists of triangular faces and sets of three vertices that form these triangles. The converted lists of triangular faces and sets of vertices can be saved to the standard STL format for further geometrical processing. STereoLithography (STL) is a data format native to stereolithography CAD (3D Systems, Valencia, California, U.S.). This file format is supported by many other 3D CAD software packages for visualization and geometrical processing as well. The resulting STL models were imported to Geomagic (Geomagic, Research Triangle Park, NC), smoothed and decimated to ~40,000 meshes per bone. We note that the general method presented in this work can be applied to femoral, tibial and patellar cartilage and is also applicable to other articular joint cartilage, as long as the cross section of the cartilage is arc-shaped.

3.2.3 Validation of segmentation method

Laser Scanning

After MR scanning, the porcine specimens were laser scanned. By comparing the geometry obtained from the MR images with the geometry obtained from the laser scans, we were able to measure the accuracy of the segmentation algorithm. The semi-automated MR segmentation method presented herein was validated by comparing segmented MR images of three porcine knees with post-dissection laser scans of cartilage regions (Koo, Giori et al. 2009). Articular cartilage surfaces of the femur, tibia, and patella were scanned using a portable 3D laser scanner (ShapeGrabber: Ottawa, Canada) (Figure 18). The axial resolution of the laser scanner was 0.1 mm. Since the laser scanner can only scan the surfaces that are exposed to the optical sensor, scans were repeated at different angles and registered using Geomagic (Research Triangle Park, NC). To scan the femur, the bone was first oriented such that the resulting scan was in the coronal plane. This position was marked as 0 degrees. Each subsequent scan was completed after the bone was rotated in an increment of 45 degrees, resulting in a total of eight scans. Patellar and tibial cartilages were scanned in four planes, including the posterior-superior, posterior-inferior, posterior-medial and posterior-lateral view. Three screws placed into the bone surface allowed for registration of these different scans. Cartilage tissues were exposed to room temperature air for less than 10 min during preparation and 12 min during laser scanning to prevent volume change due to dehydration (Koo, Giori et al. 2009). After the articular surfaces of the cartilage had been scanned, specimens were submerged in an 8.25% sodium hypochlorite solution for 18

hours to 24 hours to dissolve the cartilage (24 hours for femoral and tibial cartilage, 18 hours for patella cartilage) (Koo, Giori et al. 2009). Thick cartilage tissue will take longer to be completely dissolved. Following cartilage removal, only bone remains. Laser scans were repeated on this remaining tissue. The model created from the specimen with cartilage and the model created from the cartilage-free specimen were registered using the best fit alignment function in Geomagic. The three screws fixed on the bone surface were used as landmarks to register. By performing Boolean operations on these two scans using Geomagic, the cartilage geometries were acquired (Figure 18). Because laser scanning is known as a very accurate method of obtaining 3D geometries, the geometries acquired by the laser scanner were used as the “gold standard” to calculate the accuracy of the 3D models generated from the MR images (Koo, Giori et al. 2009).

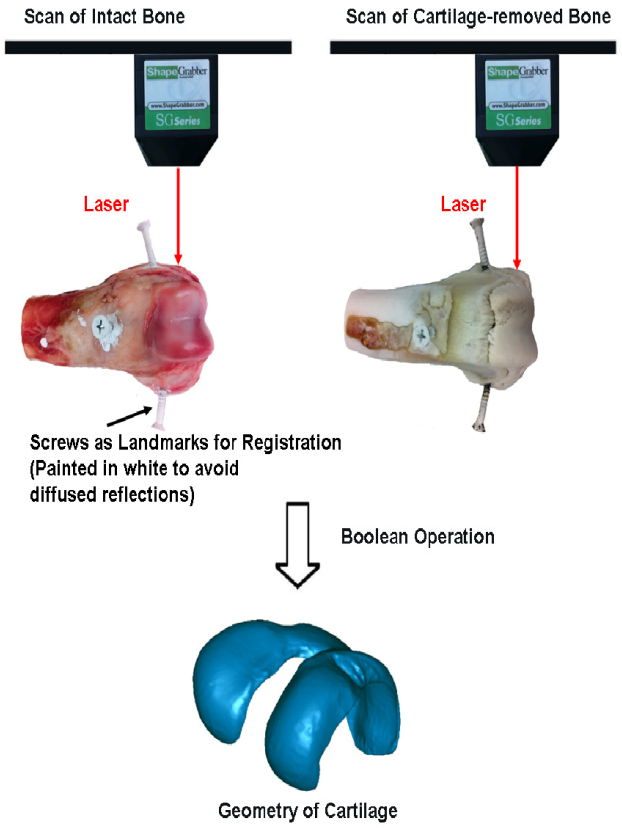

Figure 18. Applying Boolean operation between the geometry with and without cartilage which were scanned using laser scanner to create 3D cartilage model. Three screws were fixed on bone to register the location of two models.

Comparing geometries

3D geometries from the semi-automated MR image segmentation program and laser scanning device were registered to each other using the best fit alignment function in Geomagic (Chen and Medioni 1991). Differences in thickness between the two models were calculated as follows. First, thicknesses of each model were computed for all the points on the articular surface (outer surface) by searching the nearest 3D point on the

bone-cartilage interface surface (inner surface). The thickness data was saved on 3D thickness maps. Then, the thickness was compared on the nearest points of the two models (Koo, Giori et al. 2009).

3.3. Results

Thickness maps were able to elucidate variability in cartilage thickness (Figure 19).

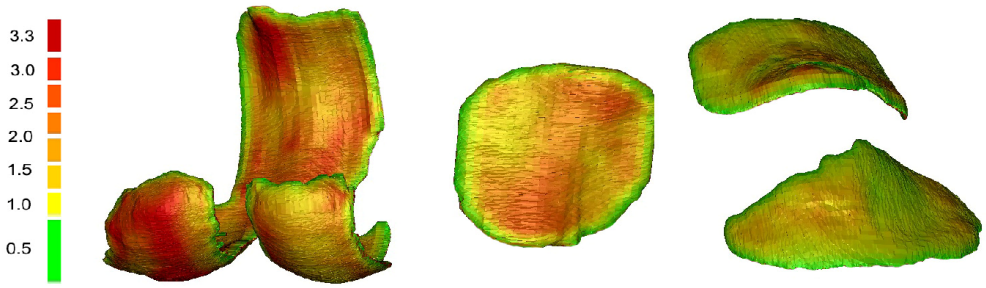

Figure 19. The 3D thickness maps of femoral, patella and tibial cartilage model segmented from FSE Cube MR images.

The accuracy vs. thickness of both the FSE Cube sequence and the IDEAL SPGR sequence are shown in (Figure 20). The cartilage thickness based on the 3D model acquired from MR images tends to be overestimated for thin regions and overestimated for thick regions. MRI tends to overestimate when the thickness of the region of interest is less than 2.3mm and underestimate when it is over 2.3mm. It is known that the thickness of thin regions is overestimated due to the partial volume effect and MR imaging voxel anisotropy. There was a significant linear relationship between the actual cartilage thickness and the accuracy, which was consistent with the literature (Koo, Giori et al.

2009). Overall, the mean accuracy of the FSE Cube was within +0.25mm and -0.10mm and that of the IDEAL SPGR was within +0.35mm and -0.40mm. This shows the model segmented from the FSE Cube has higher accuracy than the model from the IDEAL SPGR.

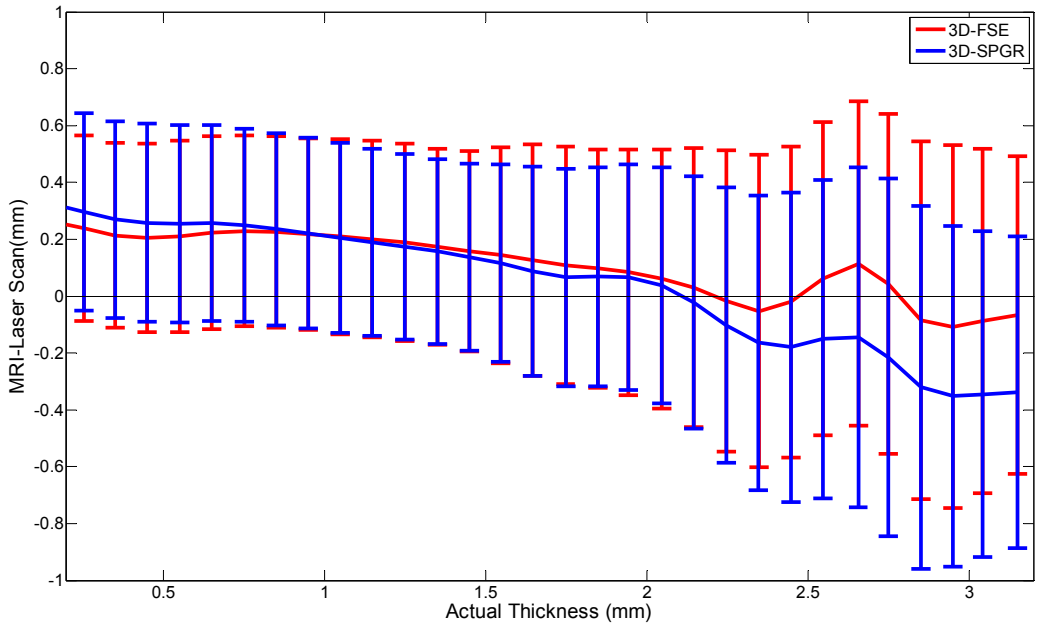

Figure 20. Differences in thickness measurement between MRI based 3D models and laser-scan based 3D models. The means of the differences were drawn as lines, and standard deviation for every 0.1mm range was drawn as error bars. Three porcine knees were used to evaluate the accuracy

The semi-automated segmentation technique was tested on human knee MR images to check the feasibility of use with images of human cartilage. Preprocessing times to remove noise in bony regions are not included. After approximately 30 minutes of noise removal pre-processing, the MR images were tested. First, the repeatability to construct the 3D model from the MR images was measured. Differences in 3D thickness between the two models constructed from the two repeated MR scans are shown in (Figure 21). Repeatability was within +0.2mm and -0.1mm for both3D-FSE and 3D-SPGR.

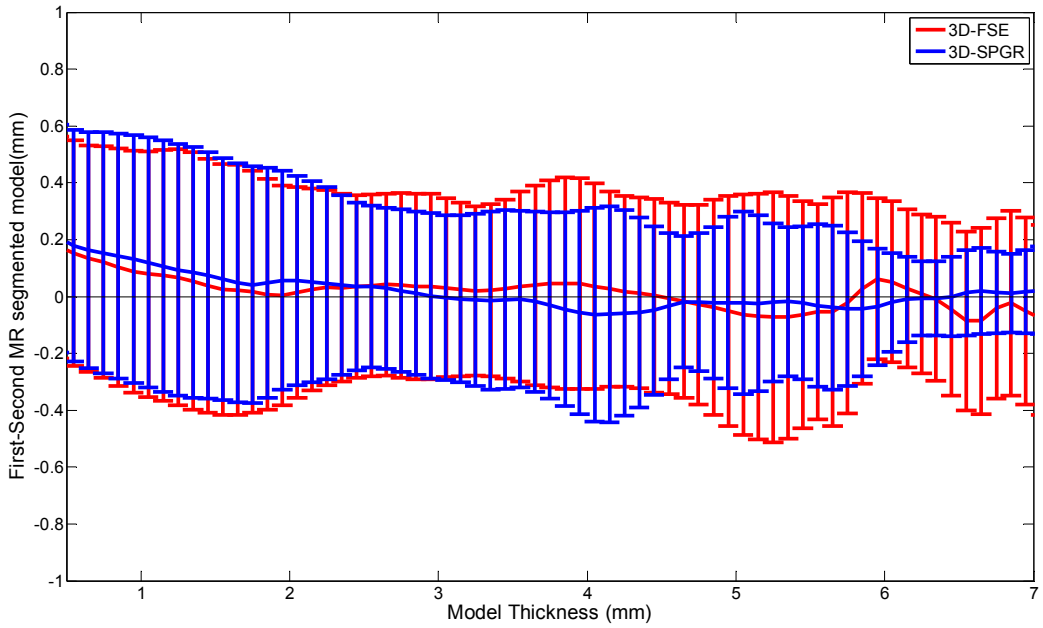

Figure 21. Differences in thickness measurement between 3D models from first scan and second scan of human knee MRI. The means of the differences were drawn as lines, and standard deviation for every 0.1mm range was drawn as error bars. MR images from five healthy male subjects were used to evaluate the repeatability

Table 1. Time performance of semi-automated segmentation method for human knee MRI. MR images from five healthy male subjects were used to evaluate the performance.

Sequence	Cartilage Region	Average Number of slices	Average Detection Time/slice(s)	Average Correction time/ slice(s)	Average Segmentation Time/slice(s)	Average Total Time (s)	Average Total Time(min)
FSE Cube	Femur	72.8	4.01	3.22	7.23	526.34	8.77
FSE Cube	Tibia	55.6	3.92	1.39	5.31	295.23	4.92
FSE Cube	Patella	44.0	3.78	6.39	10.17	447.48	7.46
	Total	172.4	11.71	11.00	22.71	1268.19	21.13
IDEAL SPGR	Femur	74.0	3.93	5.58	9.51	703.74	11.73
IDEAL SPGR	Tibia	65.4	4.07	1.75	5.82	380.63	6.34
IDEAL SPGR	Patella	44.2	3.68	7.80	11.48	507.42	8.46
	Total	183.6	11.68	15.13	26.81	1591.79	26.52

Second, the detection time for each MR slice was measured (Table 1). However, when there were errors in detection, these regions were manually corrected. The manual correction times were recorded. Processing time per image for segmentation including manual correction is shown in Table 1. The overall performance on human knee MR images was 22.71 s/slice for the FSE Cube sequence and 26.81 s/slice for the IDEAL SPGR sequence. The time performances for both MR sequences are fast enough to be practical for clinical use.

Additionally, cartilage free porcine patella bone was submerged into an 8.25% sodium hypochlorite solution for an additional 72 hours to ensure that the solution did not digest porcine bone tissue. The geometry of the cartilage free patella was laser-scanned before it was submerged. After the extra 72 hours, the geometry was rescanned. The two

geometries were registered to each other using a surface matching function in Geomagic, and the thicknesses were compared (Figure 22).

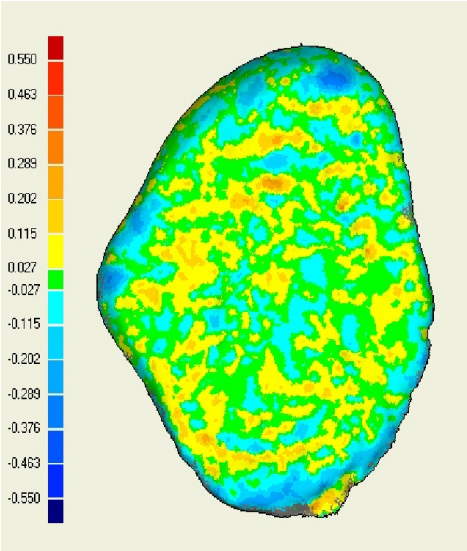

Figure 22. Comparison of porcine patella bone geometries after immersion in 8.25% sodium hypochlorite solution for 72 hours.

The average positive thickness difference between two surfaces was 0.053mm and the average negative error was -0.056mm. The positive and negative thickness differences came from the error during model registration. Overall, the average thickness difference including positive and negative was 0.0025mm and its standard deviation was 0.073mm. This shows the solution does not digest bone tissue.

3.4. Discussion

Computer assisted segmentation techniques could enhance the use of MRI for evaluating cartilage health, while reducing user time and providing repeatable quantitative

assessments. In recent years, there have been a series of advances in MRI segmentation for the quantitative assessment of cartilage volume in longitudinal clinical studies(Eckstein, Cicuttini et al. 2006). Recent MRI segmentation methods can be divided into two categories by the degree of human user interaction with the computer: fully automatic segmentation methods which do not require any user interaction, and semi-automated methods which require some degree of user interaction. Then each method can also be subdivided into two sub-categories: the boundary-based methods that rely on analysis of the energy level of the image pixels to delineate a region of interest's boundary, and region-based methods that rely on the analysis of the homogeneity of a spatially localized region to select the area of the region of interest.

Several fully automatic segmentation methods have been developed. Tamez-pena et al. (Tamez-Pena, Farber et al. 2012) proposed a region-based method to fully-automatically segment the knee cartilage using the Atlas database. The Atlas database is built from knee MR images of many healthy subjects, and segmentation is conducted based on comparison to the pre-accumulated database. Fripp et al. (Fripp, Crozier et al. 2010) also developed a fully-automatic boundary-based cartilage segmentation method using the active shape model (ASM). Active shape models (ASMs) are statistical models of the shape of objects which iteratively deform to fit within the boundary of cartilage. The initial rough shapes are built from a training set of triangulated surface representations of each of the bones in the knee. Both Atlas and ASM based methods are fully-automatic methods that rely on *a priori* knowledge of healthy knee shapes from many subjects (Cootes, Taylor et al. 1995; Tamez-Pena, Farber et al. 2012). It is pointed out by the authors that diseased knees would be more difficult to segment due to their odd shapes

(Fripp, Crozier et al. 2010), and would require higher computation cost since they access pre-stored databases of healthy knee shapes and continuously compare current detected cartilage volume to pre-stored volumes (Cabezas, Oliver et al. 2011).

Various semi-automated segmentation methods have been developed that require different degrees of user interaction. Stammberger et al. (Stammberger, Eckstein et al. 1999), Peterfy et al. (Peterfy, van Dijke et al. 1994), Piplani et al. (Piplani, Disler et al. 1996) and Eckstein et al. (Eckstein, Gavazzeni et al. 1996; Eckstein, Schnier et al. 1998) utilized semi-automatic region-based methods such as “region growing” to segment cartilage regions. Lynch et al. (Lynch, Zaim et al. 2000), Stammberger et al. (Stammberger, Eckstein et al. 1999) and Kauffmann et al. (Kauffmann, Gravel et al. 2003) utilized boundary-based methods such as “active contour (also known as snakes)”. Active contours are computer-generated curves that move within images to find target boundaries. Steines et al. (Steines and P. 2000), Gougoutas et al. (Gougoutas, Wheaton et al. 2004) and Bowers et al. (Bowers, Trinh et al. 2008) utilized boundary-based methods such as “live wire”. Live wire is a segmentation technique which allows a user to select regions of interest using simple mouse clicks. The user sets the starting point clicking on an MR image’s pixel. Then, as the user starts to move the mouse over other pixels, the smallest cost path is drawn from the starting point to the pixel the mouse is over, changing itself if the user moves the mouse. This method is widely used in the field of image segmentation because the user can check the boundary detection in real time while working, but it requires the most user interaction. Aforementioned methods let the initial user-defined contour grow to fit in the boundary of the cartilage without prior knowledge of knee shape. However, Solloway et al. (Solloway, Hutchinson et al. 1997)

utilized semi-automated boundary-based methods using the “active shape model (ASM)”. The active shape model is an advanced version of the active contour method. It is also known as “smart active contour or smart snakes”. It uses some degree of pre-accumulated database to increase the detection rate. Compared to the fully automated ASM method utilized by Fripp et al. (Fripp, Crozier et al. 2010), this method is a semi-automated application of ASM which still needs some degree of user interaction: The initial rough shapes are built by the user. Ghosh et al. (Ghosh 2000) utilized boundary-based methods such as “immersion based watershed”. The algorithms of their method can be simply described by figuring that holes are punctured in each local minimum of the topographic relief. Next, the surface is slowly immersed into ‘virtual water’, by that, filling all the water basins, starting from the basin that is associated to the global minimum. As soon as two water basins tend to merge, a dam is built. The procedure results in a partitioning of the image into many water basins, of which the borders define the watersheds. Kshisagar et al. (Kshirsagar, Watson et al. 1998) utilized a boundary-based method such as “edge detection” to segment the cartilage regions. Stehling et al. (Stehling, Baum et al. 2011) proposed a semi-automated boundary-based segmentation method that superimposes two different MR image sequences to detect cartilage boundaries. However, this method requires two different MR sequences of the same knee to segment the images, and thus would not be practical for clinical use.

Each existing segmentation method has pros and cons. The novelty of the algorithm we developed comes from the integration of boundary-based methods with a region-based approach. We took strengths of each approach and integrated them to increase the boundary detection. Generally, computer assisted full or semi-automated

algorithms should give similar or better accuracy and reproducibility than manual segmentation methods, but with faster time, less effort, and less need for an expert (Stammberger, Eckstein et al. 1999). However, in most of these computer assisted methods, it would be very difficult to detect the anterior beginning point and posterior ending point of the cartilage boundary in the sagittal MR images without enormous prior knowledge of knee shape. The semi-automated technique we have developed utilizes a combination of semi-automated methods, specifically to increase the detection rate of the anterior beginning point and posterior ending point of the cartilage boundary. To increase the bone-cartilage contrast, we first deleted the noise in the bony region, using the combination of “geodesic active contour” and the “fuzzy C means method”, then applied “edge detection” to clearly detect the boundary of the cartilage. Then we let the user click points to select the anterior beginning, the center of the bony region and the posterior ending points of the cartilage. These points are very hard to be identified by computer software, so that the human “eye” is the best solution to identify these points. The pre-processing of noise removal takes about 30 min to remove noise in the bony region in 80~90 slices of MR images and this is the part where most of time is spent. However, in the case of larger slice thicknesses, this time could be reduced. To expedite the pre-processing speed, every two (or more) slices could be averaged to reduce the number of slices.

Ideally, validation of the segmentation method should be not only on phantoms but on the actual biological tissue of interest (Eckstein, Cicuttini et al. 2006). The porcine knee was used to validate the accuracy and reproducibility and MR images from human subjects were used to test the processing time. The laser scanning method was used as

a “gold standard” to measure the accuracy in this study. It is known as a very accurate method of measurement and is relatively easy and convenient to use. Koo et al. (Koo, Giori et al. 2009) assessed the accuracy of *in vivo* cartilage thickness measurements from MR image-based 3D cartilage models using a laser scanning method and found that the thickness of cartilage in MRI were overestimated in thinner regions while the thick regions in the weight bearing area were underestimated. The accuracy of thickness in the MR segmented 3D cartilage models systematically varied according to actual cartilage thickness. The accuracy we measured using porcine knees also varied systematically and show consistency with Koo et al. (Koo, Giori et al. 2009). This variation in accuracy was derived from the nature of technical limitations in current MR imaging and soft tissue behavior. For MRI, reproducibility depends on the process of image acquisition, image analysis, and measurement method (Eckstein, Cicuttini et al. 2006). The processes of image acquisition and analysis were controlled for repetitive MR scans while there was some degree of manual correction by the user on a section-by-section verification. The difference in reproducibility was mainly derived from user correction during segmentation.

Chapter 4: Computationally Efficient Collision Detection Algorithm to enable the Calculation of Complex Cartilage Contact Pressure Patterns within Biomechanical Simulations of Movement

4-1. Introduction

The location and magnitude of knee joint articular contact are important factors that can affect the long-term health of cartilage tissue (Andriacchi and Dyrby 2005; Andriacchi, Briant et al. 2006; Chaudhari, Briant et al. 2008; Tashman, Kopf et al. 2008; Andriacchi 2009). However, joint contact modeling represents a computationally challenging problem due to the complexity of articular surface geometries, nonlinear tissue properties and the intermittent nature of loading during gait (Arnold, Ward et al. 2010; Dhaher, Kwon et al. 2010). These challenges tend to preclude the direct use of finite element analysis within a multi-joint dynamic simulation of movement. Discrete element analysis (DEA) represents a viable approach that computes contact pressure based on the degree of overlap between interacting cartilage surfaces. In a DEA approach, cartilage tissue is represented as an array of compressive springs overlying rigid body representations of the articulating bone surfaces (An, Himeno et al. 1990; Li 1994; Iwasaki, Genda et al. 1998; Genda, Iwasaki et al. 2001; Volokh, Chao et al. 2007). DEA approaches have been used to study contact mechanics in various diarthrodial joints, most recently progressing to fully 3D subject-specific geometry (Anderson, Iyer et al. 2010).

The most time-consuming step in DEA is the detection of overlap between high resolution articulating surface meshes. This task can be exceptionally burdensome within a dynamic simulation of movement, where collision detection and penetration depth calculations must be repeated at every integration time step in order to update contact pressure. A brute force approach to collision detection would evaluate penetration between every pair of faces of two surfaces, resulting in an order (N^2) computation time.

Various algorithms have been proposed to speed up the process of computing cartilage surface contact within dynamic simulations. Dhaher et al. described articular surfaces as the inner product of two basis functions, providing for continuous contact calculations(Dhaher, Delp et al. 2000). Bei and Fregly used polygon meshes, but restricted collision detection to neighbors of previous contact patches, thereby leveraging the fact that relatively small changes in pose occur between simulation time steps (Bei and Fregly 2004). Collision detection of polygon surfaces is a well-studied problem in the graphics community (Bergen 2004). One promising approach involves the use of bounding volume hierarchichal structures (BVH) and ray-casting to rapidly narrow down the regions of surface that may be overlapping(Gottschalk 1996; Schmidl 2004). Further computational gains can be achieved by porting this routine onto parallel cores of the Graphics Processing Unit (GPU)(Lauterbach 1981), allowing for collision detections to be performed on multiple mesh faces simultaneously.

The objective of this study was to assess the feasibility of using BVH/ray casting techniques to enable the simulation of cartilage pressure distributions within a multibody dynamic knee model. We first investigate the computational gains and convergence properties that are achievable when using a range of mesh densities to represent the cartilage surfaces. We then demonstrate the use of the DEA approach for simulating knee cartilage pressure within a whole body simulation of gait.

4.2. Methods

4.2.1. Cartilage Surface Geometries and Bounding Volumes

High-resolution magnetic resonance (MR) images of the right knees of a healthy young adult male (age= 22 yr, height= 177.80 cm, mass=79 kg) were acquired under a protocol approved by the Wisconsin Health Science Institutional Review Board. A VIPR ATR sequence(Al Saleh, Hernandez et al. 2013) was used to obtain isotropic volumetric

images with 0.3 mm cubic voxels. The images were manually segmented (MIMICS, Materialise Group, Leuven, Belgium) to obtain 3D geometries of the femoral cartilage, tibia plateau and patellar facet cartilage surfaces (Kaiser, Bradford et al. 2012) (Figure 23). These surfaces were smoothed in Geomagic (3D Systems, Morrisville, North Carolina) and decimated to obtain surface geometries of varying resolution, ranging from 260 (34.9 mm^2/element) to 1.3 million (0.007 mm^2/element) of total triangular elements on the tibial and femoral surfaces (Table 2).

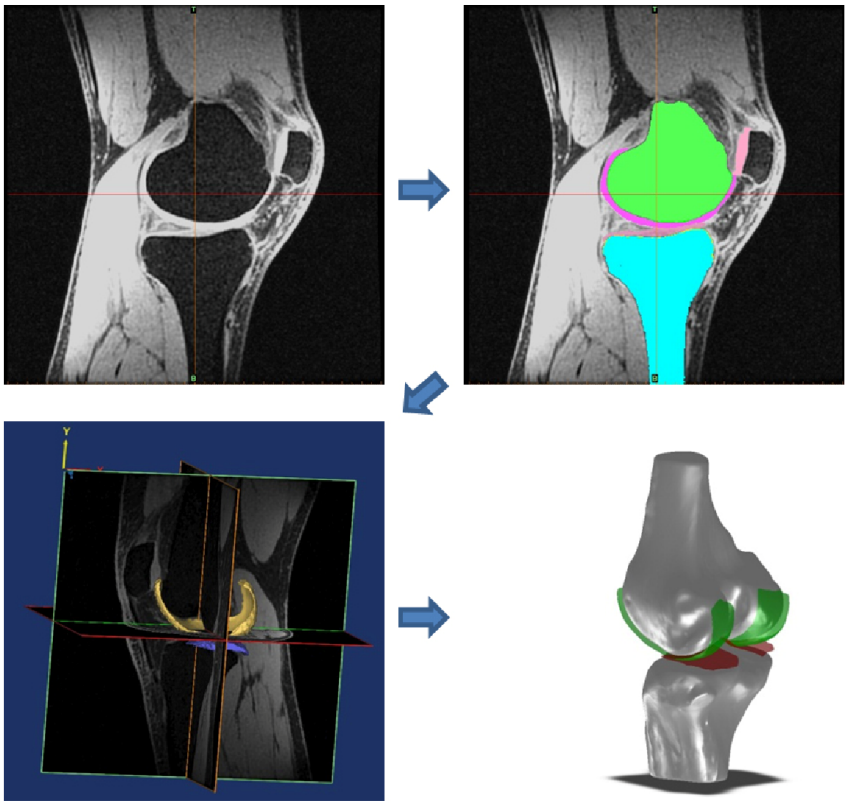

Figure 23. Segmentation of Knee Cartilage

Contact detection was facilitated by creating a BVH of the femoral cartilage geometry using tight-fitting, oriented bounding box trees (OBB Trees)(Gottschalk 1996;

Schmidl 2004). A bounding volume hierarchy (BVH) is a tree structure on a set of virtual bulks to wrap geometric objects and oriented bounding box is a type of virtual bulk used to wrap the geometric objects. The lowest level of the BVH tree structure consists of boxes, termed leaf nodes, that tightly fit over each element of the femoral cartilage surface. Leaf nodes are then recursively grouped as small sets and enclosed within larger OBBs until a single OBB tightly encapsulates the entire femoral cartilage geometry(Gottschalk 1996; Schmidl 2004).

4.2.2. Contact detection and calculation of penetration depth

Contact Detection: Contact detection is the process of detecting the degree of overlap, i.e. the depth of penetration, between two surface measures. One first sets the three-dimensional pose of the meshes based on the position and orientation of the bone segments to which they are attached. In our case, the femur and tibia segments were posed based on simulated gait pose. For each triangle of the tibia plateau, a series of ray-OBB intersection tests were then conducted. A ray is cast normal to the triangle and an intersection test is performed to see if the ray intersects the largest OBB of the target femoral geometry (Williams, Barrus et al. 2005) (Figure 24).

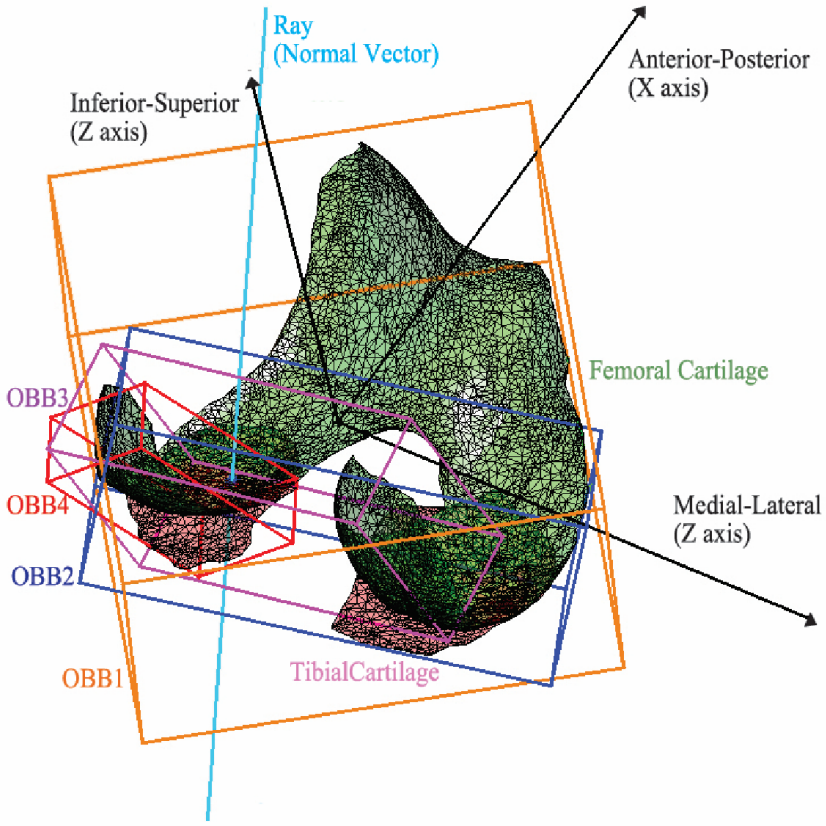

Figure 24. Ray-OBB intersect test between target and contact body

If there is no intersection, the test is terminated. If a ray intersects this hierarch OBB, then this ray will be tested with OBBs in the next sub-hierarchy. The ray-OBB test is repeated recursively until it finds the leaf node (Choi 2013). The result is a pair of triangles in the tibial (contact) and femoral (target) bodies. The depth of penetration, d, is then determined by computing the distance from the contact surface face centroid to the ray-intersection point on the corresponding leaf node triangle (Equation 1):

$$d = \frac{\left(\vec{C}_2 - \vec{C}_1\right) \cdot \hat{n}_2}{\hat{n}_1 \cdot \hat{n}_2} \quad \text{(Equation 1)}$$

A distance *d*>0 is indicative of penetration of the tibia triangle into the femoral surface. Assuming the cartilage tissue to be linearly elastic, contact pressure is then computed using an elastic foundation model that can accommodate the larger deformations that occur in natural knee cartilage (Equation 2).

$$p = -\frac{(1-\nu)E}{(1+\nu)(1-2\nu)} \ln\left[1 - \frac{d}{h}\right] \quad \text{(Equation 2)}$$

where γ is Poisson's ratio, E the elastic modulus of cartilage, and h is the combined thickness of femoral and tibial cartilage (An, Himeno et al. 1990; Blankevoort, Kuiper et al. 1991b; Bei 2004; Lin 2004).

4.2.3. GPU Implementation of Contact Detection Algorithm

The contact detection was implemented on the GPU using Compute Unified Device Architecture (CUDA) to gain additional speed. In contrast to a serial implementation on the Central Processing Unit (CPU), the GPU implementation can leverage a larger number of Arithmetic Logical Units (ALUs) which can perform ray-BVH intersection tests in parallel (Figure 25). Further, the multi-cores in GPU are used as high throughput, many-core processors (Lauterbach 1981) to construct a parallel OBB tree, test hierarchical intersections and query penetration.

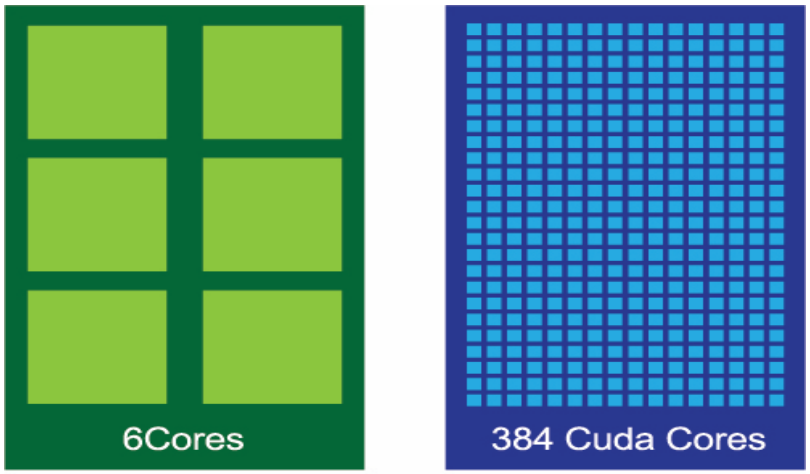

Figure 25. CPU computing architecture consists of a small number of fast processing cores (ALU). In contrast, The GPU has a larger number of cores that can perform a many operations in parallel.

4.2.4. Neuromusculoskeletal Model

To assess the performance of the tibiofemoral contact algorithm, we incorporated the contact surfaces into a previously developed 6 degree-of-freedom tibiofemoral joint model (Thelen, Choi et al. 2014). The knee model included nonlinear spring representations of 19 ligaments (Shelburne, Torry et al. 2006; Shin, Chaudhari et al. 2007), and a one degree-of-freedom patellofemoral joint that allowed the patella to translate in a constrained path relative to femur. The knee model was implemented into a multi-body musculoskeletal dynamics model (SIMM, MusculoGraphics, Inc., Santa Rosa, CA) that included 44 Hill-type musculotendons acting about the hip, knee and ankle(Arnold, Ward et al. 2010) (Figure 26). A computed muscle control algorithm was

used to compute muscle excitations needed to drive the musculoskeletal model to track kinematics measured during normal overground walking (1.25 m/s) (Thelen, Choi et al. 2014). At each time frame of the simulation, the current pose of the femur, tibia and patella were used to calculate the ligament forces and cartilage pressure of the knee model. These knee model outcomes were then applied within the dynamic simulation when computing body accelerations (Figure 26).

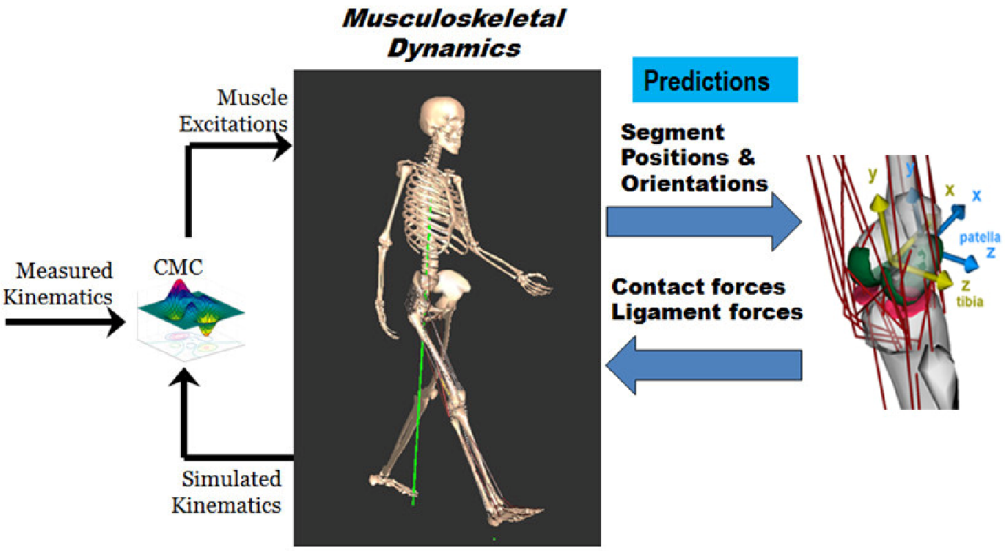

Figure 26. Co-simulation framework in which muscle excitations are varied such that a multi-body dynamics model tracks measured gait kinematics. A 6 degree of freedom tibiofemoral model with 19 ligaments and articular contact is solved for the ligament and contact forces at each time step of a dynamic simulation.

4.2.5. Performance Tests

We performed a series of tests to assess the influence of the mesh density and processor implementation (CPU: AMD Phenom II X6 1055 T Processor 2.8GHz with 8GB Main RAM, GPU: NVIDIA GeForce GTX 560Ti with 1GB Graphics RAM) on the contact computation time and contact pressure patterns. Computation times were evaluated at a single pose of the femoral and tibia corresponding to the second peak of the tibiofemoral force during stance. Reported GPU times include the transfer time between the main memory in the host and the global memory in the GPU. To test how the cartilage mesh density effects computation time and contact pressure calculations, we repeated the analyses for a range of mesh densities. For each mesh density, we computed the contact area, the center of contact pressure location, and average pressure at the second force peak of stance. The CPU-implementation was not tested due to time limitations.

Table 2. Numbers of triangles in 3D models used for the convergence test and their corresponding average triangle sizes

Femoral Cartilage		Tibial Cartilage		Total Knee Cartilage	
# of triangles	Average triangle area (mm^2)	# of triangles	Average triangle area (mm^2)	# of triangles	Average triangle area (mm^2)
130	51.929	130	17.793	260	34.927
260	26.139	260	8.889	520	17.514
650	10.338	650	3.556	1,300	6.947
6,500	1.029	6,500	0.354	13,000	0.691
26,000	0.257	26,000	0.089	52,000	0.173
65,000	0.103	65,000	0.035	130,000	0.069
104,000	0.064	104,000	0.022	208,000	0.043
416,000	0.016	416,000	0.005	832,000	0.011
650,000	0.010	650,000	0.004	1300,000	0.007

4.3. Results

A dynamic simulation of one gait cycle takes 120 minutes to run. Tibiofemoral contact force patterns over a gait cycle (Figure 27) exhibited the characteristic double-peak during stance, with greater net force borne on the medial tibia plateau than on the lateral tibia plateau. Predicted cartilage contact pressures exhibited greater magnitudes and excursion on the medial tibia plateau during gait cycle (Figure 28). Medial cartilage

contact pressure progressed anteriorly through much of stance, reaching a peak forward position prior to toe-off, which is consistent with empirically derived contact patterns (Liu, Kozanek et al. 2010).

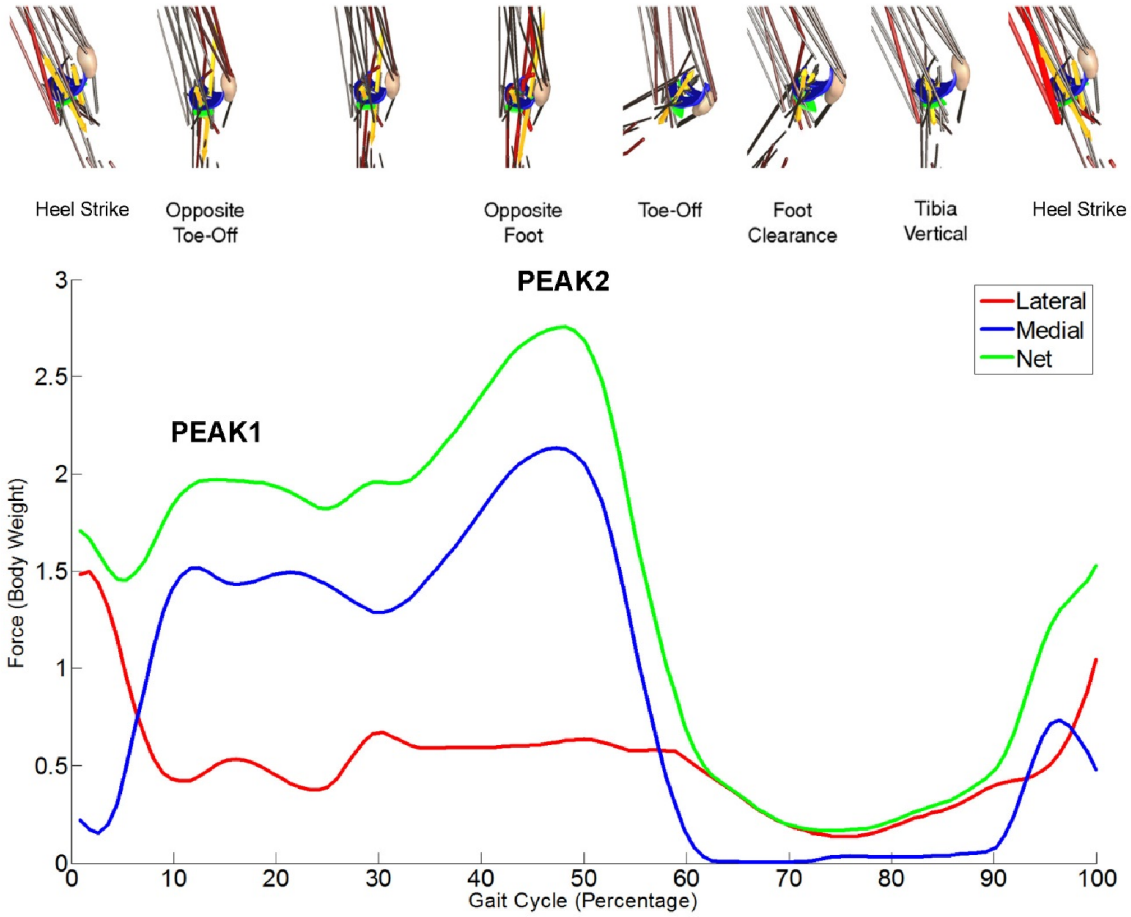

Figure 27. Simulated contact force on articular cartilage of the right tibia plateau cartilage over a gait cycle

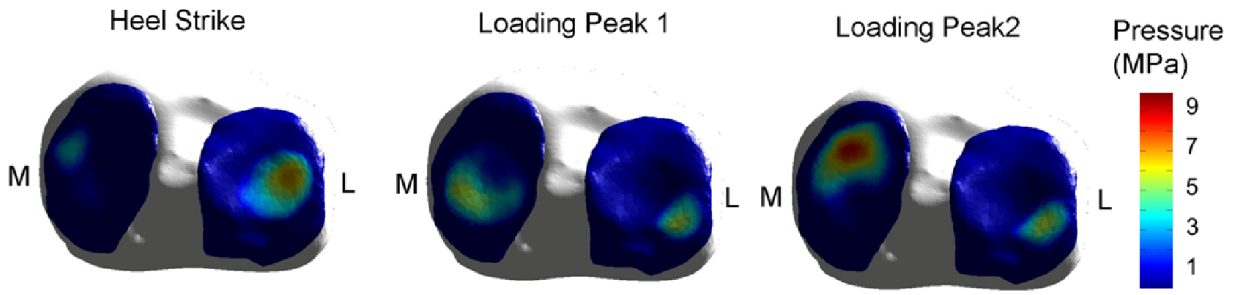

Figure 28. Simulated contact pressure on articular cartilage of the right tibia plateau cartilage at heel strike, peak load 1 and peak load 2

Solution time increased with increasing mesh density for both BVH implementations, though the rate of increase was greater for the CPU algorithm than the GPU (Figure 29). GPU implementation of BVH was 10x faster than the CPU implementation with 1,300,000 elements in the knee model. The BVH algorithm on the CPU provided a 10,900x increase in speed over the brute force CPU method. Contact parameters were dependent on mesh density but converged to within 2% of the limiting value at 52,000 elements (Figure 30) (Table 2).

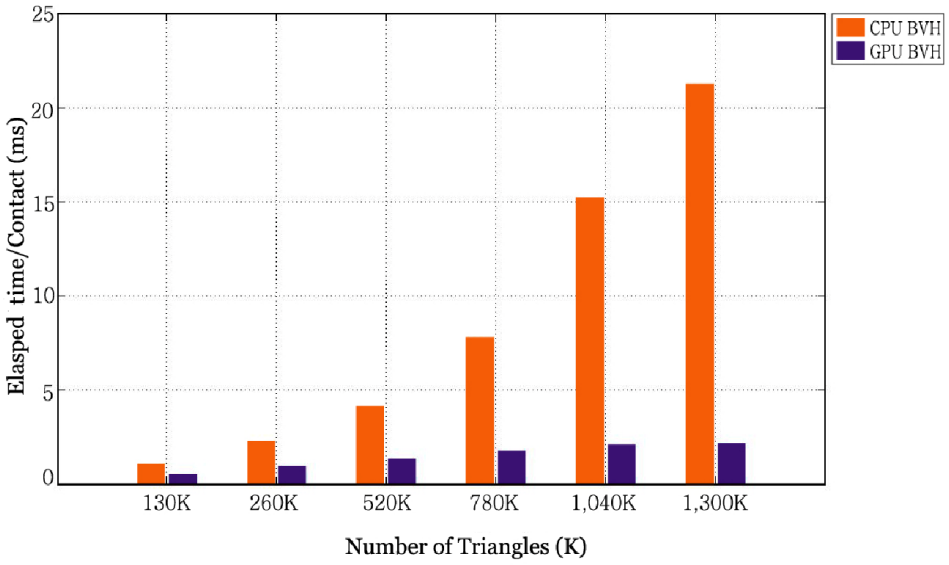

Figure 29. Speed test for the BVH algorithm implemented on the CPU and GPU

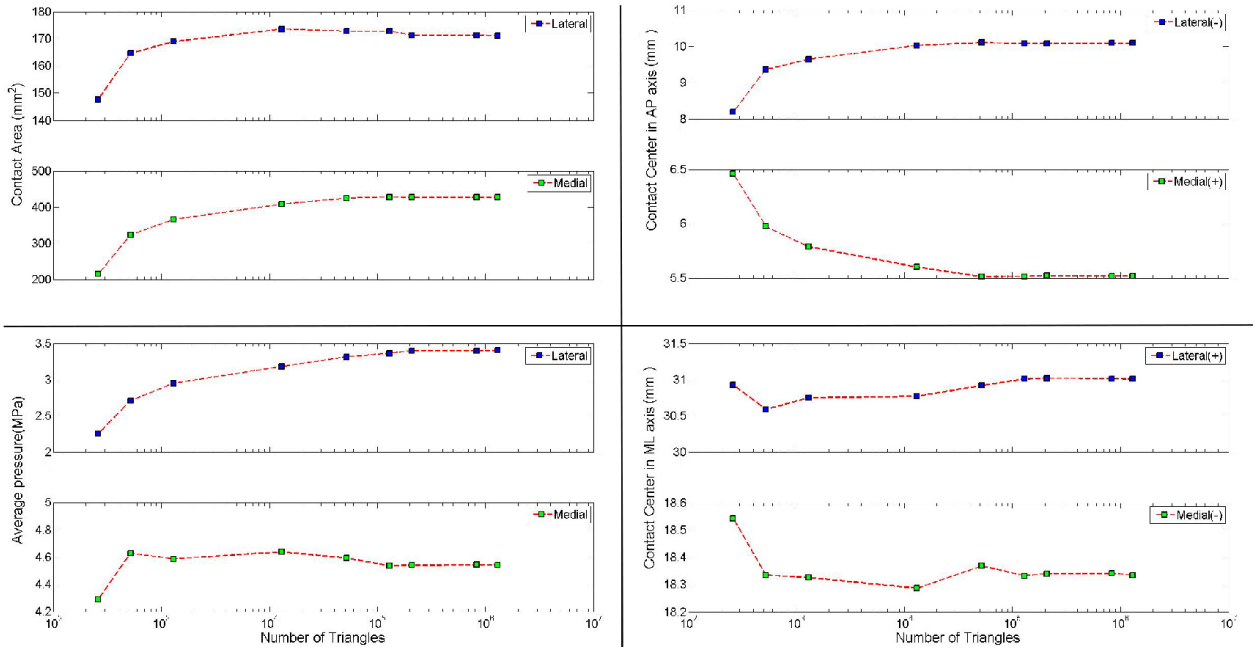

Figure 30. Mesh density influences the contact area, center of contact location and average contact pressure on articular cartilage of the tibia plateau at the second peak force of stance.

4-4. Discussion

The results of this study demonstrate the benefits of using bounding volume hierarchical (BVH) structures to compute the location of contact between articular surfaces. The contact detection algorithm treats each face of the contact body independently, which allows for easy parallel implementation on multiprocessors. This allowed us to implement the algorithm on a graphics processor unit (GPU), which was up to 10X faster than running the same algorithm on a CPU. The advantage of GPU-based calculation of contact detection increased substantially with mesh density, which reflects

some of the overhead costs associated with CPU-GPU data transfer that arises in GPU scientific computing.

Speed-up of contact detection is important given that contact pressure calculations have to be performed every time step in a dynamic simulation, which can thus represent the most time consuming task in simulating gait. We note that within a dynamic gait simulation, that the tibiofemoral pose does not change considerably between two successive integration time steps. Hence in practice, additional computational gain is achieved by simply checking if the paired triangles from a prior step still remain in contact. This test is achieved using a single ray-triangle intersection test(Moller 1997), which when positive circumvents the need to re-progress through the BVH.

Our gait simulation predicted the characteristic bimodal loading of the tibiofemoral joint during the stance phase of walking. The magnitudes of the net tibiofemoral joint contact forces (2 BW and 2.8 BW for the first and second peak) are consistent with predictions made by simpler knee models and *in vivo* measures obtained with instrumented implants (Fregly, Besier et al. 2012). The medial contact pressures were higher than on the lateral side, and the medial center of pressure progressed anteriorly over stance. In vivo tibiofemoral contact pressures during gait are not available, thus direct validation is not feasible. However, the simulated pressure patterns agree favorably with image-based measures of tibiofemoral contact patterns during normal gait. Liu et al. measured cartilage deformations of 7 to 23% during the stance phase of gait, with larger anteriorposterior excursions and contact areas on the medial tibia plateau than on the lateral plateau. Our gait simulations show similar trends, with the medial plateau center

of pressure progressing anteriorly 7.9 mm between the first and second peaks of stance (Figure 28). Medial cartilage contact area estimates are very similar to Liu et al.'s measurements, while our lateral contact area tends to be ~50% lower(Liu, Kozanek et al. 2010). Further study is needed to determine the underlying causes of such differences.

Our sensitivity analyses provide an objective basis for settling on the mesh densities needed to use DEA models to assess cartilage contact. We found mesh densities of >100,000 triangles for the two articulating surfaces (average triangle area <0.1 mm^2) produced consistent estimates of peak tibia plateau pressure, contact area and center of pressure that varied less than 0.15%.

There are limitations to consider in this work. First we did not include a meniscus in our knee model which is well recognized to distribute pressure in the tibiofemoral joint. Recent studies have introduced discretized meniscus models (Anderson, Iyer et al. 2010; Guess, Thiagarajan et al. 2010) that would be well suited to incorporate in future iterations of the multi-body knee models. Our pressure calculations assume linearly elastic cartilage tissue properties, which clearly ignores viscoelastic effects. Adding in viscoelasticity would increase complexity considerably by adding additional state variables to track, such that it may be preferable to use gait simulation outputs on a more conventional finite element model to consider more complex material properties.

We conclude that a BVH implementation on the GPU is a viable approach for simulating articular contact in gait, can produce pressure estimates consistent with empirical observations. The computational speed achieved allows for simulations to be performed more readily, permitting the use of probabalistic approaches to look at how

injury and intervention-induced changes in knee structure may affect in vivo knee mechanics and function.

Chapter 5: The Accuracy of Simulated Tibiofemoral Contact Loads Obtained via the Co-Simulation of Neuromuscular Dynamics and Knee Mechanics

(Thelen, Choi et al. 2014)

5-1. Introduction

The magnitude and location of joint contact forces are important to consider when assessing the causes and treatment of knee pathologies (Andriacchi, Mundermann et al. 2004). Since internal loads cannot normally be measured *in vivo*, computational models are needed to estimate the joint contact forces that can arise during functional tasks such as walking. The traditional modeling approach involves two steps. A multi-body neuromuscular dynamics model is used in the first step to estimate muscle and net joint forces associated with a task performance (Anderson and Pandy 2001; Taylor, Heller et al. 2004). These forces are subsequently applied as boundary conditions to a knee mechanics model to estimate ligament forces and the distribution of joint contact loads (Shelburne, Torry et al. 2005; Shelburne, Torry et al. 2006; Kim, Fernandez et al. 2009). However, this serial simulation approach may not capture two-way interactions that can exist between musculoskeletal dynamics and internal joint mechanics. In particular, musculoskeletal models used to simulate movement typically use a simplified knee model with pre-assumed constraints on secondary knee motions (Delp, Loan et al. 1990; Wilson, Feikes et al. 1998; Arnold, Ward et al. 2010). This approach assumes that contact forces do not induce moments about the primary joint axis, and that muscle forces are not important contributors to secondary motion constraints (Lin, Walter et al. 2010). However, the validity of such assumptions was questioned in a recent study that showed that

muscle force estimates are sensitive to the constraints included in the knee model (Lin, Walter et al. 2010). Hence, it would seem preferable to co-simulate neuromuscular dynamics and knee joint mechanics, such that muscle, contact and ligament loads are considered within the context of whole body movement dynamics.

The co-simulation of movement and localized tissue mechanics represents a computationally demanding problem that has only recently been explored in the biomechanics literature (Halloran, Erdemir et al. 2009; Halloran, Ackermann et al. 2010). A major challenge involves the computation of appropriate muscle controls that drive a model to emulate coordinated movement. Prior studies have pre-assumed the muscle excitation patterns (Piazza and Delp 2001) or used dynamic optimization to compute muscle excitations that achieve a desired performance criterion (Halloran, Ackermann et al. 2010). While dynamic optimization is an attractive approach, obtaining a global optimum can be very challenging and require many iterations to converge (Neptune 1999).

We previously introduced a computed muscle control (CMC) algorithm which uses feedforward and feedback control to modulate muscle excitations to track measured joint angle trajectories (Thelen, Anderson et al. 2003; Thelen and Anderson 2006). CMC was originally formulated to work on models in which all joints have constrained translational degrees of freedom (e.g. a gimbal joint). Translational constraints allow for instantaneous force transmission across the joint, and hence a quantitative assessment of a muscle's capacity to induce movement throughout the body. However in a dynamic multi-body model with 6 degree-of-freedom (d.o.f.) joints, time is required to deform the soft tissues and thereby transmit forces across a joint. Hence, the first objective of this study was to

extend the CMC algorithm to co-simulate musculoskeletal dynamics and joint mechanics when using models that include 6 d.o.f. joints spanned by soft tissues. Second, we sought to assess the veracity of the co-simulation framework by comparing model predictions of knee contact forces to *in vivo* measures obtained with an instrumented total knee joint replacement during walking (Fregly, Besier et al. 2012). Finally, we demonstrate the capacity of the framework to assess the sensitivity of contact loading patterns to variations in frontal plane knee alignment, which is an important consideration in joint replacement procedures.

5-2. Methods

5-2-1. Experimental Data

The experimental data used in this study were collected as part of the 4th grand challenge competition for predicting in vivo knee loads (Fregly, Besier et al. 2012). We simulated the gait of a male subject (age 88 yrs, mass = 68 kg, height = 1.66 m) who received an instrumented total knee replacement on the right side for primary osteoarthritis. The data downloaded from the competition website (https://simtk.org/home/kneeloads) included the knee replacement geometry, post-operative CT scans, electromyographic data, whole body kinematics, ground reactions and tibiofemoral contact forces during overgound walking. Medial and lateral tibiofemoral contact forces were delineated using four uniaxial force transducers embedded in the tibial tray (D'Lima, Townsend et al. 2005).

5-2-2. Knee Mechanics Model

We created a 3 body model of knee mechanics that included a one d.o.f. patellofemoral joint and a six d.o.f. tibiofemoral joint (Shelburne, Torry et al. 2006; Shin, Chaudhari et al. 2007). Superior patella translation was the independent degree of freedom for the patellofemoral joint. The patellofemoral angles and anterior and lateral patella translation were defined as constrained functions of superior translation, such that the patella could translate and rotate within a constrained path relative to the femur(Delp 1990). Seventeen knee ligament bundles were included in the model (Figure 31): the patellar ligament (medial, mid and lateral bundles), the medial collateral ligament (MCL, 5 bundles), lateral collateral ligament (LCL), popliteofibular ligament (PFL), posterior cruciate ligament (anterior and posterior bundles), posterior capsule (4 bundles) and the illiotibial band (ITB). The anterior cruciate ligament (ACL) was not included since it was resected in the subject whose gait was simulated (Fregly, Besier et al. 2012). Ligament geometry data was not available for the test subject, so ligament origins and insertions were based on nominal descriptions in the literature (Sugita and Amis 2001; LaPrade, Ly et al. 2003; Davies, Unwin et al. 2004; Edwards, Bull et al. 2007; Petersen and Zantop 2007; Liu, Yue et al. 2010). Wrapping objects were affixed to the femur to represent the collateral ligaments wrapping about the condyles. The nonlinear relationship between ligament force, F_ℓ, and strain, ε_ℓ, was represented by:

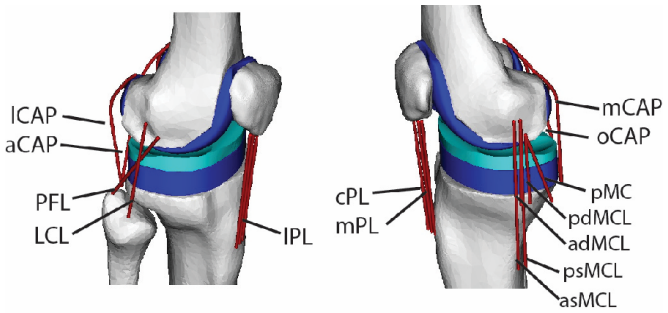

Figure 31. The three body knee mechanics model included 17 ligament bundles acting about the tibiofemoral and patellofemoral joints. Contact pressure between the femoral component and tibial insert was computed via an elastic foundation model. Ligament abbreviations are given in Table 3.

$$F_\ell = \begin{cases} 0 & \varepsilon < 0 \\ \dfrac{k\varepsilon^2}{4\varepsilon_\ell} & 0 < \varepsilon < 2\varepsilon_\ell \\ k\left(\varepsilon - \varepsilon_\ell\right) & \varepsilon > 2\varepsilon_\ell \end{cases} \quad \text{(Equation 3)}$$

where ε_ℓ (=0.03) is the transition strain and *k* is the ligament stiffness expressed in units of force per unit strain. At any time point, the ligament bundle strain, $\varepsilon = \left(L - L_0\right)/L_0$, was computed from the current length (L) and slack length (L_0) of the ligament. The slack length of each bundle was computed by scaling the ligament length in a reference configuration with its assumed reference strain ε_{ref} :

$$L_0 = L_{ref}/(1+\varepsilon_{ref}) \quad \text{(Equation 4)}$$

Ligament stiffness and reference strains were adapted from representative values used in comparable knee models in the literature (Shelburne, Torry et al. 2006; Shin, Chaudhari et al. 2007) (Table 3).

Table 3: Ligament stiffness and reference strains used in the knee mechanics model. A negative reference strain assumes that the ligament is slack in the reference posture.

Ligament	Stiffness (N)	Reference Strain
aPCL	3000	-0.10
pPCL	1500	-0.05
asMCL	1500	0.02
psMCL	1500	0.02
adMCL	1000	0.02
pdMCL	1000	0.02
pMC	2000	0.02
LCL	4000	0.02
PFL	2000	-0.05
aCAP	1500	0.02
lCAP	2000	0.02
oCAP	1500	0.02
mCAP	2000	0.02
mPL	4000	0.00
cPL	4000	0.00
lPL	4000	0.00
ITB	5000	0.00

Stiffness is expressed in units of force per unit strain. Reference strains are used to compute the ligament lengths in the upright reference configuration. Notation: aPCL, pPCL – anterior and posterior cruciate ligament; asMCL, psMCL – anterior and posterior superior medial collateral ligament; adMCL, pdMCL – anterior and posterior deep medial collateral ligament; pMC – posteromedial capsule; LCL – lateral collateral ligament; PFL – popliteofibular ligament; aCAP, lCAP, oCAP, mCAP – arcuate, lateral, medial and oblique posterior capsules; mPL, cPL, lPL – medial, central and lateral patellar ligament; ITB – ilitotibial band

The geometry of the implanted femoral component and tibial insert were represented by triangulated polygon meshes of the subject's joint replacement. Tibiofemoral contact loads were computed using an elastic foundation model in which pressure was assumed to be a function of the depth of penetration of intersecting bodies (Bei and Fregly 2004). Intersecting regions between the femoral and tibia surface geometry were detected using ray casting in conjunction with hierarchical bounding volumes (BV). To do this, the femoral surface was first subdivided into a tree of geometrically coherent subsections, and tight-fitting oriented bounding boxes (OBB) were fit over each subdivision (Bergen 2004). A normal ray was then cast for each triangle of the tibia and a ray-OBB intersection test was performed with the largest OBB. If intersected, ray-OBB tests continued to sub-hierarchical levels, ultimately identifying the leaf node (single triangle) of the femoral surface intersected by the ray (Gottschalk 1996; S. Gottschalk 1996; Bergen 2004; Schmidl 2004). The penetration depth, *d*, was defined as the distance from the center of a tibia triangle to the point at which a normal ray intersected the corresponding femoral leaf node. The contact pressure *p* on the tibia surface triangle was then calculated using a linearized version of an elastic foundation model (Bei and Fregly 2004):

$$p = -\frac{(1-\nu)E}{(1+\nu)(1-2\nu)}\frac{d}{h} \quad \text{(Equation 5)}$$

were h is the insert thickness, ν is Poisson's ratio (=0.46) and E is Young's modulus (=463 MPa) for a ultra-high molecular weight polyethylene tibial insert (Kurt, Jewett et al. 2002). The force acting on the tibia surface triangle was obtained by multiplying the pressure by

the triangle cross-sectional area and applying the force normal to the triangle. Equal and opposite forces were applied at the same point in the femoral surface.

5-2-3. Lower Extremity Musculoskeletal Model

We started with a generic lower extremity musculoskeletal model (Arnold, Ward et al. 2010) that included the pelvis, right femur, tibia, patella and foot segments. The hip was represented by a 3 d.o.f. ball-and-socket joint, and the ankle as a 1 d.o.f. joint that allowed for dorsi- and plantarflexion. We replaced the 1 d.o.f. knee in the generic model with the 3-body knee model described earlier. The femoral component surface geometry was positioned such that it closely aligned with the condyles of the generic model's femur. The tibia insert surface geometry was then positioned in the tibia reference frame so that it closely aligned with the femoral component when the model was in an upright standing posture. The lower extremity model was scaled to represent the subject. Each body segment was scaled such that anatomical landmarks were optimally aligned with anatomical marker positions recorded with the subject standing upright. During scaling, the frontal plane knee angle was fixed at 4 deg valgus, as was measured from the post-operative CT scans of the subject.

The model included 44 Hill-type musculotendon units acting across the hip, knee and ankle joints (Arnold, Ward et al. 2010). The input to each muscle was an excitation that could vary between 0 and 1. Excitation-to-activation dynamics were represented by a bi-linear differential equation with activation and deactivation time constants of 15 and 40 ms, respectively. Contraction dynamics was represented by a nonlinear differential

equation describing the interaction of tendon compliance and the force-length-velocity properties of muscle (Thelen 2003). The lower extremity model was implemented in SIMM (Delp and Loan 1995), with the Dynamics Pipeline (Musculographics Inc., Santa Rosa, CA) and SD/Fast (Parametric Technology Corp., Needham, MA) used to generate code describing the multibody equations of motion.

5-2-4. Computed Muscle Control Algorithm

With the muscles and knee model included, the multi-body dynamic equations of motion are of the form:

$$\mathbf{M}\ddot{\mathbf{q}} = \mathbf{R}^m\mathbf{F}^m + \mathbf{R}^\ell\mathbf{F}^\ell + \mathbf{R}^c\mathbf{F}^c + \mathbf{F}^e + \mathbf{G}(\mathbf{q}) + \mathbf{C}(\mathbf{q},\dot{\mathbf{q}}) \quad \text{(Equation 6)}$$

where $\mathbf{M}$ is the mass matrix, $\mathbf{G}(\mathbf{q})$ is a vector of forces arising from gravity, $\mathbf{C}(\mathbf{q},\dot{\mathbf{q}})$ are forces arising from coriolis and centripetal accelerations, and $\mathbf{F}^e$ represents generalized forces arising from external loads or prescribed accelerations. The force vectors arising from muscle ($\mathbf{F}^m$), ligament ($\mathbf{F}^\ell$) and articular contact ($\mathbf{F}^c$) are scaled by moment arm matrices $\mathbf{R}^m$, $\mathbf{R}^\ell$ and $\mathbf{R}^c$, respectively. The generalized coordinates, $\mathbf{q}$, include the six d.o.f. pelvis motion (translation and orientation) relative to ground, three hip rotation angles, three tibiofemoral angles, three tibifemoral translations, superior patella translation and ankle dorsiflexion. Pelvis, hip and tibiofemoral angles are expressed as a Cardan rotation sequence consisting of flexion, adduction and then rotation about the long axis of the distal segment (Grood and Suntay 1983).

A computed muscle control (CMC) algorithm was used to determine the muscle excitations needed to drive the model to closely track measured hip flexion, hip adduction, knee flexion and ankle dorsiflexion trajectories (Figure 32). CMC is a feedforward-feedback controller that uses the experimentally measured accelerations ($\ddot{\mathbf{q}}^{exp}$) together with current errors in generalized speeds ($\dot{\mathbf{q}}^{exp} - \dot{\mathbf{q}}$) and coordinates ($\mathbf{q}^{exp} - \mathbf{q}$) to compute a set of desired generalized accelerations in the degrees of freedom being tracked:

$$\ddot{\mathbf{q}}^{des} = \ddot{\mathbf{q}}^{exp} + k_v\left(\dot{\mathbf{q}}^{exp} - \dot{\mathbf{q}}\right) + k_p\left(\mathbf{q}^{exp} - \mathbf{q}\right) \qquad \text{(Equation 7)}$$

where k_v and k_p are velocity and position feedback gains, respectively.

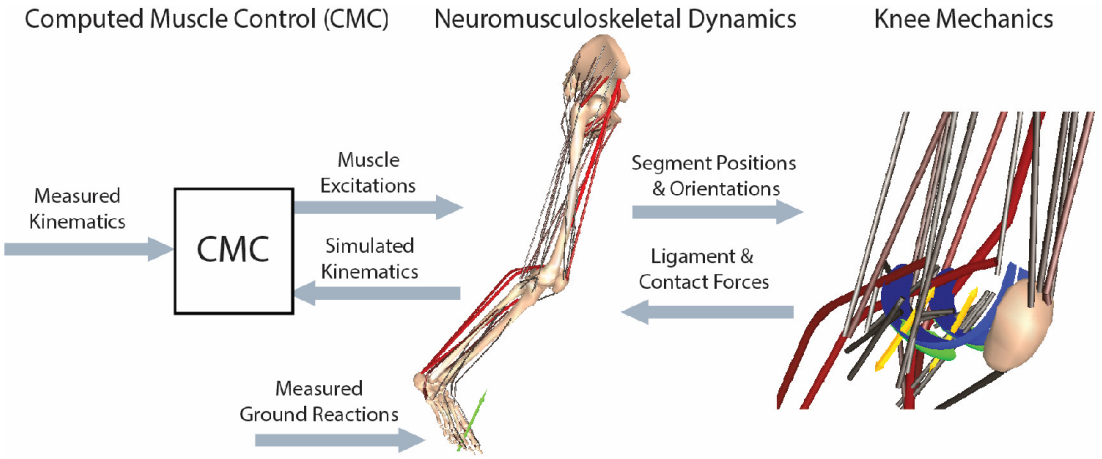

Figure 32. A computed muscle control (CMC) algorithm was used to modulate the lower limb muscle excitations such that the simulation closely tracked the measured hip, knee and ankle angles. At every time step, the tibia, patella and femur positions were used to ascertain the tibiofemoral contact and ligament forces. These forces were then applied within the forward dynamic simulation of the neuromusculoskeletal model.

The original formulation of CMC was implemented for multi-body models in which all joints had constrained translational d.o.f., allowing for instantaneous load transfer across the joint to occur. Such a formulation allows for a muscle's potential to induce motion, defined as the generalized accelerations generated per unit muscle force (Arnold, Anderson et al. 2005), to be directly computed from the whole body equations of motion. Computationally, muscle potential is determined by applying a unit muscle force, $\hat{F}_i = 1$, and then solving the equations of motion (equation 6) for the resulting accelerations ($\ddot{\mathbf{q}}_i = \mathbf{M}^{-1}\mathbf{R}_i^m$). However in the case of a 6 d.o.f. tibiofemoral joint, it is not feasible for a muscle proximal to the knee to instantaneously generate segment accelerations distal to the

knee. Time is needed for ligament and contact surface deformations to occur, such that force is transmitted across the joint. To handle this challenge, we adapted CMC to compute a muscle's potential to induce joint accelerations assuming the knee translational accelerations are instantaneously zero. This assumption was used since contact and ligament forces restrict the knee translations to relatively small magnitudes. A zero translational acceleration constraint therefore allowed for instantaneous force transmission across the knee, and thus provided an estimate of the effect of ligament and contact forces on joint rotational accelerations. To implement the constraint, we first defined a vector, $\mathbf{q}_x$, as the subset of generalized coordinates associated with the tibiofemoral (q_{tx}, q_{ty}, q_{tz}) and patellofemoral (q_{py}) translational degrees of freedom.

$$\mathbf{q}_x = \begin{bmatrix} q_{tx} & q_{ty} & q_{tz} & q_{py} \end{bmatrix}^T \qquad \text{(Equation 8)}$$

We used a finite difference technique to estimate a sensitivity matrix, $\mathbf{S}_x$, describing the dependency of generalized accelerations to variations in the knee translational degrees of freedom.

$$\mathbf{S}_x = \left[\frac{\partial \ddot{\mathbf{q}}}{\partial q_{tx}} \frac{\partial \ddot{\mathbf{q}}}{\partial q_{ty}} \frac{\partial \ddot{\mathbf{q}}}{\partial q_{tz}} \frac{\partial \ddot{\mathbf{q}}}{\partial q_{py}} \right] \qquad \text{(Equation 9)}$$

These sensitivities were then used to determine virtual perturbations, $\delta\mathbf{q}_x$, to the translation knee coordinates that, in conjunction with a unit muscle force, would negate translational knee accelerations. This assumption was applied for each muscle *i* by solving the following linear equations:

$$\hat{\ddot{\mathbf{q}}}_i = \mathbf{M}^{-1}\mathbf{R}_i^m + \mathbf{S}_x \delta\mathbf{q}_{x,i} \qquad \text{(Equation 10)}$$

$$\hat{\ddot{\mathbf{q}}}_x = \mathbf{0} \qquad \text{(Equation 11)}$$

for $\delta\mathbf{q}_{x,i}$ and $\hat{\ddot{\mathbf{q}}}_i$. The vector $\hat{\ddot{\mathbf{q}}}_i$ is an estimate of the potential of muscle *i* to induce accelerations throughout the limb per unit muscle force.

The muscle potential acceleration information was used to update muscle controls every T=0.01 seconds within a simulation. When updating controls, we first determined muscle force increments, $\delta\mathbf{F}^m$, that when added to the current muscle forces would induce desired accelerations in the tracked degrees of freedom:

$$\ddot{\mathbf{q}}^{des} = \sum_{i=1}^{m} \delta F_i^m \hat{\ddot{\mathbf{q}}}_i + \ddot{\mathbf{q}}^{cur} \qquad \text{(Equation 12)}$$

In eq. (10), $\ddot{\mathbf{q}}^{cur}$ represent the generalized accelerations resulting from current muscle forces, ligament forces, contact forces, external force and gravity acting on the system. Muscle redundancy was resolved by simultaneously minimizing a cost function J which, in this study, was taken as the sum of muscle-volume (V) weighted squared activations (a) (Happee 1994):

$$J = \sum_{i=1}^{m} V_i a_i^2 \qquad \text{(Equation 13)}$$

where muscle activations are determined based on the force-length-activation properties of muscle (Thelen and Anderson 2006). Excitations were then determined from activations by inverting activation dynamics. After computing the controls, the skeletal equations of motion, muscle activation dynamics and contraction dynamics were integrated forward using a forward-backwards implicit numerical integration routine

(Hindmarsh, Brown et al. 2005). The control process was then repeated every T=0.01 sec throughout a gait simulation.

5-2-5. Simulations of Knee Mechanics during Gait

We generated simulations of five overground walking trials with an average gait speed of 1.25 (±0.02) m/s. For each gait trial, a global optimization inverse kinematics routine was first used to determine the pelvis translations, pelvis rotation, hip angles, knee flexion and ankle dorsiflexion that best agreed with the measured pelvis and lower extremity marker trajectories. At this stage, the knee abduction angle was maintained at 4 deg while the tibiofemoral internal rotation and translations were assumed to be constrained functions of knee flexion as defined in the generic lower extremity model of Arnold et al. (Arnold, Ward et al. 2010).

We then used the CMC algorithm to compute muscle excitations that drove the dynamic multi-body model to track measured hip flexion, hip adduction, knee flexion and ankle dorsiflexion trajectories over a gait cycle. Measured ground reactions were applied directly on the feet (Thelen and Anderson 2006), while pelvis generalized coordinates were prescribed to track measured values. The tibiofemoral translations, patellofemoral translation, tibiofemoral internal rotation and tibiofemoral adduction were unconstrained in the dynamic simulations, and thus evolved naturally as a function of the external and internal loads acting on the system. We compared the timing of muscle excitations to temporal patterns of electromyographic data that were recorded from the subject during the walking trials simulated. Model predictions of tibiofemoral contact forces acting in the medial and lateral compartments were quantitatively compared to *in vivo* measures using

Pearson's correlation, the coefficient of determination, the average difference in the force predictions (bias), the standard deviation of the force prediction errors (precision) and the root-mean-squared (r.m.s.) error. We also evaluated the agreement between the medial, lateral and total contact forces at the time of the two peak contact forces that arise in the stance phase of normal gait.

5-2-6. Sensitivity of Model Predictions to Frontal Plane Alignment

We performed a sensitivity study analyzing the dependence of tibiofemoral loading patterns to variations in frontal plane alignment between the femoral component and tibia insert. To do this, we first re-ran the inverse kinematics routine with fixed knee valgus angles 2 deg greater and less than that measured (4 deg valgus) on the CT scans. For each case, we re-oriented the femoral component and tibia insert by counter-rotating each surface by 1 deg in the coronal plane, such that they were aligned and just contacting with the model in the upright standing configuration. We then used CMC to re-generate dynamic simulations using the re-aligned models to track the gait kinematics. Note that tibiofemoral adduction and rotation were not fixed in these forward dynamic simulations, but evolved as a result of tibiofemoral contact and internal soft tissue loadings. The effect of alignment on loading was quantitatively evaluated by comparing the tibiofemoral contact force and pressure patterns at heel strike, and the time of the first and second peak of the tibiofemoral contact force.

5-3. Results

The modified CMC algorithm modulated muscle excitation patterns to successfully track measured hip flexion, hip adduction, knee flexion and ankle angle trajectories with average root-mean-square errors of 0.4, 0.3, 0.9 and 1.0 deg, respectively. Simulated posterior cruciate and collateral ligament forces were relatively small (generally <100 N), with peak magnitudes arising during swing phase (Figure 33).

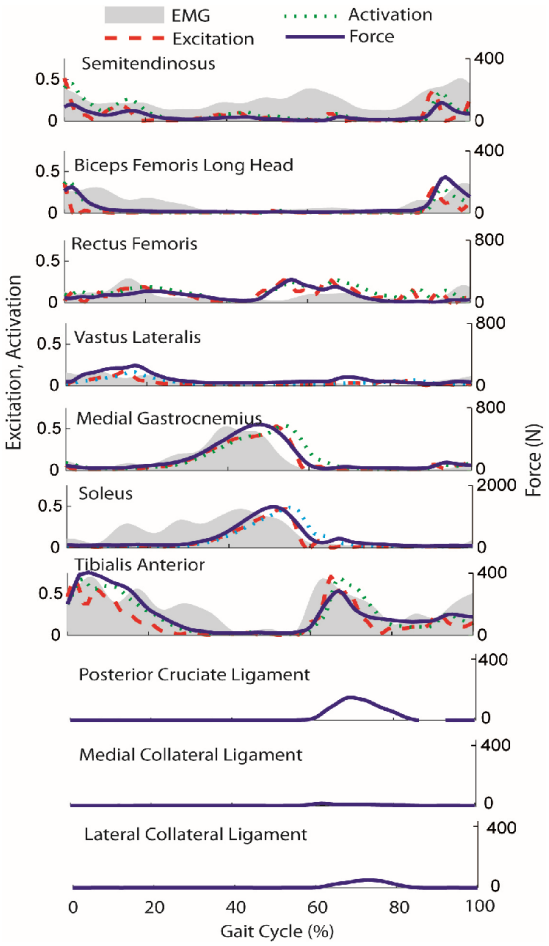

Figure 33. Comparison of average electromyographic (EMG) data with simulated muscle excitations, activations and forces over a gait cycle. Reasonably good temporal agreement is seen for the vastus lateralis, medial gastrocnemius, soleus and tibialis anterior. Normal bursts of hamstring activity (semitendinosus, biceps femoris long) in late swing and early stance are also predicted, though the subject exhibited greater medial hamstring EMG activity throughout the gait cycle. Rectus femoris EMG activity near toe-off is slightly lower than that used in the model to initiate swing limb motion between 50 and 60% of the gait cycle. Simulated posterior cruciate and collateral ligament forces were greatest in mid-swing.

Model predictions of tibiofemoral contact forces exhibited the characteristic double peak in stance, with greater load borne on the medial side (Figure 33). The temporal patterns of medial and total tibiofemroal contact forces agreed well with measurements, with average Pearson R^2 of 0.87 and 068, respectively. Temporal patterns of lateral forces were not as well predicted (R^2=0.07), with the model over-estimating lateral contact forces in early stance and mid-swing. The magnitude of medial contact forces estimates agreed well with measurements, with an average root-mean-squared (RMS) error of 0.26 body weight (BW), and a slight bias (+0.09 BW) to over-predicting the loads (Table 4). Errors in lateral force estimates were slightly larger, with average RMS errors of 0.42 BW (Figure 34). The first peak in the estimated medial load averaged 1.95 BW, which was 13% greater than experimental measures. The second medial peak estimate was 1.6 BW which was 4% above average measurements. The first and second total peak forces of 2.76 and 2.71 BW were 17% and 5% greater than the corresponding peak force measurements.

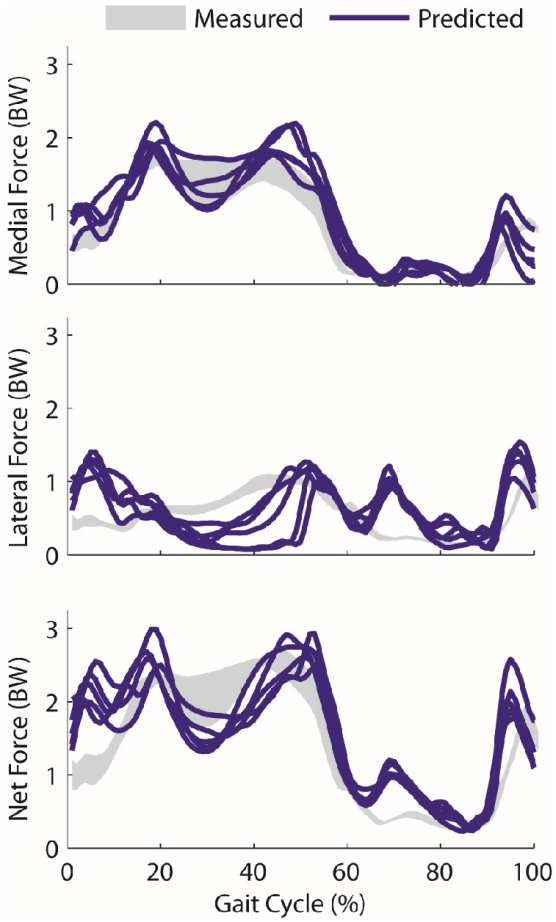

Figure 34. Model-predicted medial, lateral and total tibofemoral contact forces (expressed in units of body weight, BW) over 5 experimental walking cycles. Experimentally measured contact forces represent the mean (±1 s.d.) over the same 5 repeat walking cycles. Peak lateral contact forces are of comparable magnitude to experimental forces in late stance, but the model predicts greater lateral contact forces in early stance (0-10%) and first half of swing (60-80%) than was measured.

Table 4: Agreement (mean ±1 s.d.) between measured and model-predicted tibiofemoral joint contact forces over 5 trials of normal walk.

		Medial		Lateral		Total	
R^2, Pearson's		0.87	(0.03)	0.07	(0.08)	0.68	(0.08)
R^2, Coef of Determ		0.81	(0.05)	-1.29	(0.92)	0.60	(0.09)
Bias (BW)		0.09	(0.02)	0.06	(0.08)	0.15	(0.09)
Precision (BW)		0.24	(0.03)	0.42	(0.08)	0.48	(0.08)
RMS Error (BW)		0.26	(0.03)	0.42	(0.08)	0.51	(0.07)
Peak 1 (BW)	Predicted	1.95	(0.08)	0.81	(0.31)	2.76	(0.32)
	Measured	1.73	(0.09)	0.65	(0.06)	2.37	(0.12)
	Error	0.22	(0.10)	0.17	(0.34)	0.39	(0.34)
Peak 2 (BW)	Predicted	1.60	(0.17)	1.11	(0.13)	2.71	(0.17)
	Measured	1.56	(0.14)	1.05	(0.06)	2.60	(0.10
	Error	0.04	(0.23)	0.06	(0.14)	0.11	(0.20)

R^2 was calculated using Pearson's correlation coefficient and the Coefficient of Determination

The frontal plane alignment of the joint replacement had a substantial influence on the secondary tibiofemoral kinematics and joint loading patterns. A two deg shift toward greater valgus alignment increased external rotation in swing and internal rotation in early stance (Figure 35). A more varus alignment had the opposite effect on tibia rotation. The change in frontal plane knee alignment affected the predicted load distribution across the medial and lateral compartments. At the time of the first peak in tibiofemoral loading, the percentage of load borne on the medial component was 87%, 78% and 66% of the total load for 2, 4 and 6 deg valgus alignments. More equal distribution of load was observed at time of second peak with 66%, 59% and 52% of the total load on the medial aspect of the tibial insert. These effects carried over to the contact pressure estimates, with lower peak pressures on the medial side and greater peak pressures on the lateral side with more valgus alignment (Figure 36). Coronal alignment affected the location of pressure at heel strike, but did not substantially alter the location of peak pressure regions when the limb was loaded in mid-stance.

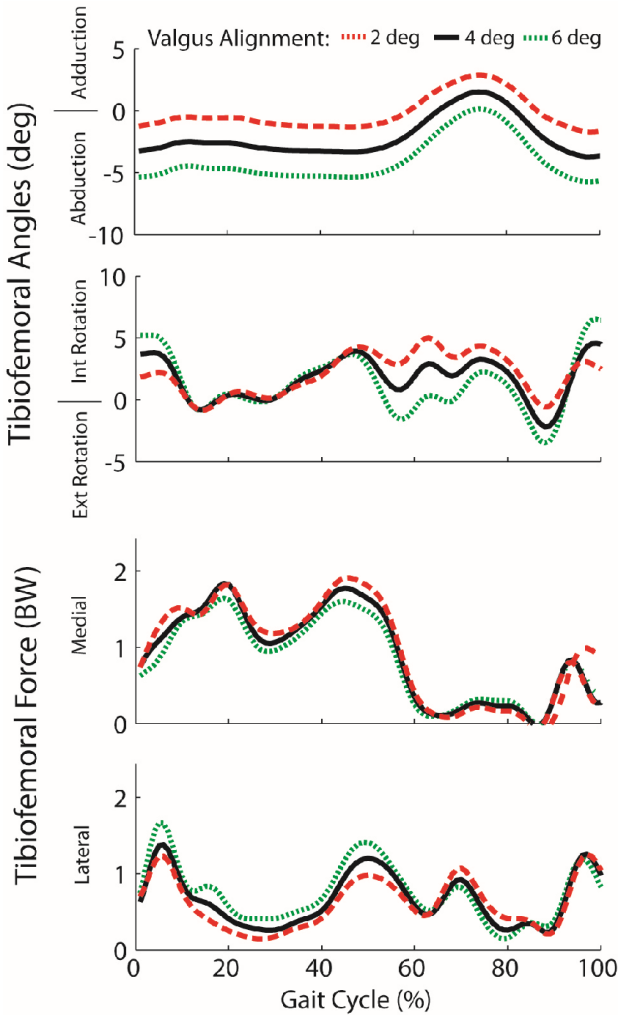

Figure 35. Frontal plane alignment of the joint replacement substantially altered tibia rotation in swing and early stance, but had little effect on rotation when the limb was loaded in mid- and terminal stance. A more valgus joint replacement alignment induced greater knee abduction, lower medial contact forces and higher lateral contact forces throughout stance.

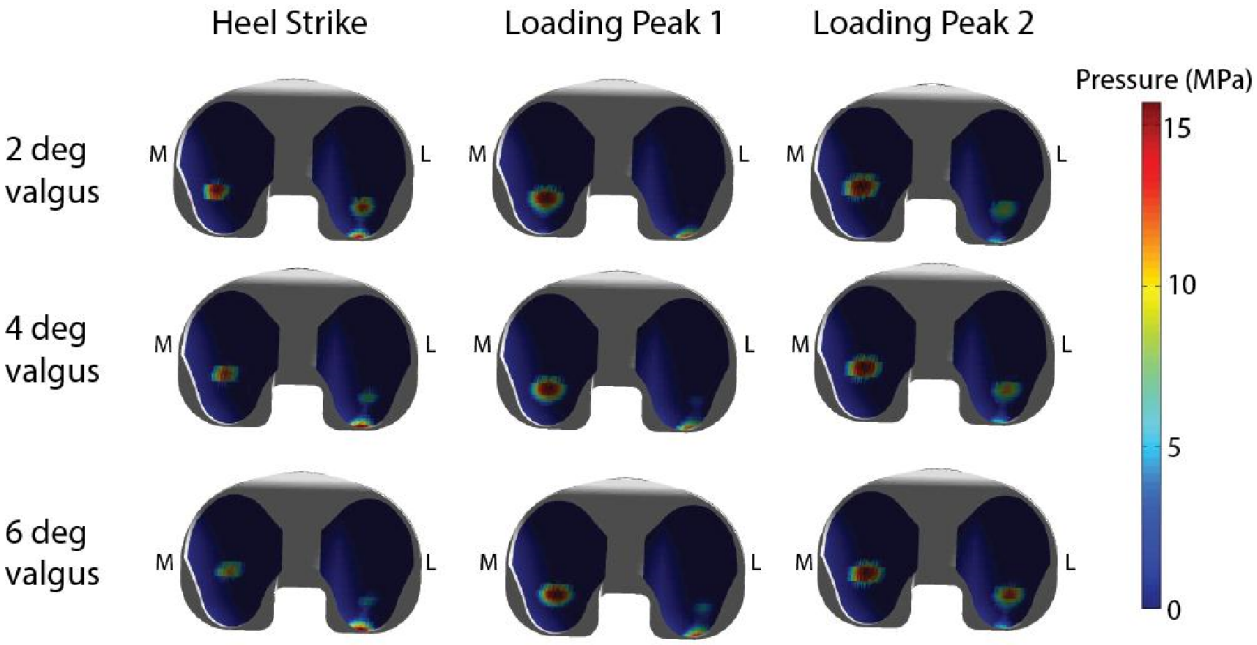

Figure 36. Predicted contact pressures on the tibial insert at the time of heel strike and the first and second peaks of the tibiofemoral contact loading. Greater valgus alignment of the joint replacement resulted in a more posteriorly loaded lateral compartment at heel strike. During stance, the location of peak pressures did not vary with alignment, but more even pressure distribution across the medial and lateral compartments is predicted in the valgus alignment.

5-4. Discussion

We have introduced a framework for simulating the interaction of muscle, ligament and joint contact forces within the context of dynamic multi-joint movement. We first showed that the framework can be used to predict knee contact force patterns that compare well with those measured directly using an instrumented knee implant (D'Lima, Townsend et al. 2005). We then demonstrated that the co-simulation framework can be used to predict the sensitivity of knee contact loading patterns to variations in implant

alignment. Such an approach allows one to virtually assess the coupled influence of physiological, surgical and design factors on *in vivo* musculoskeletal loads.

Biomechanical models have long been used to estimate the tibiofemoral loading patterns during gait. Early inverse modeling approaches tended to over-predict the tibiofemoral joint reaction forces, with estimates nearly 7 times body weight (Seireg and Arvikar 1975). More recent studies using dynamic gait analysis and knee mechanics models have produced substantially lower knee contact force estimates (2-3 times body weight) that are closer to experimentally measured values (as reviewed in (Fregly, Besier et al. 2012)). However, a primary limitation of prior studies is that a simplified knee model is often used when estimating muscle forces that arise in gait (Kim, Fernandez et al. 2009). A common approach uses a constrained 1 d.o.f. knee joint in which muscles only actuate flexion-extension. It has recently been shown that releasing these constraints can alter both muscle and joint contact force estimates (Lin, Walter et al. 2010). However, this prior study only considered knee mechanics in isolation, which does not account for the action of multi-joint muscles.

This study represents the first attempt to use the computed muscle control algorithm (Thelen and Anderson 2006) on a model with six d.o.f. joints. Most musculoskeletal models utilize joints in which inter-segmental translations are fixed or are constrained functions of joint angles (Yamaguchi and Zajac 1989; Wilson and O'Connor 1997; Arnold, Ward et al. 2010). Such joints allow for instantaneous transfer of forces, which means one can use multibody equations of motion to assess directly the potential of a muscle to generate whole body accelerations (Arnold, Anderson et al. 2005). Such is not the case in a 6 d.o.f. joint restrained by soft tissues and articular contact, in which

time is required to deform elastic tissues and transmit forces. In this study, we numerically assessed the translational stiffness arising from ligament stretch and cartilage elasticity at a point in time (equation 3-4). Using this information, we were able to approximate the translational d.o.f.'s as fixed when estimating the capacity of a muscle to induce whole body accelerations. This information could then be used within the controller to track joint angular motions about primary degrees of freedom, as originally formulated in the CMC algorithm (Thelen, Anderson et al. 2003; Thelen and Anderson 2006). A major advantage of using 6 d.o.f. joints is that secondary kinematics (e.g. tibiofemoral translations and non-sagittal rotations) evolve naturally from the muscle, ligament, contact and external forces acting on the system, and thus are fully consistent with whole body dynamics. Such a framework would be well suited to investigate how muscles can be used to stabilize joints that may be compromised by injury-induced changes in ligamentous properties (Shelburne, Torry et al. 2005; Shao, MacLeod et al. 2011).

The co-simulation framework was solvable in reasonable time periods, with approximately 100 minutes of computation time on a desktop computer needed to generate a single cycle of gait. The greatest computational burden was in detecting contact between the femoral component and tibial insert surface geometries. We were able to accelerate contact detection by using hierarchical oriented bounding boxes to quickly identify closest triangles of adjacent polygonal surfaces (Gottschalk 1996; Kurt, Jewett et al. 2002; Schmidl 2004; Hindmarsh, Brown et al. 2005). It is possible that further computational gains are achievable by using surrogate modeling approaches to infer contact pressures directly from tibiofemoral orientation and positions (Lin, Farr et al. 2006; Halloran, Ackermann et al. 2010). Contact pressures were computed using an elastic

foundation model in which it was assumed that pressure is a simple function of the depth of penetration. The ability of the elastic foundation model to ascertain contact stress patterns in joint replacements has previously been demonstrated (Halloran, Easley et al. 2005).

We demonstrated the predictive capacity of the computational framework by varying the alignment of the knee joint replacement, and assessing how secondary motions and contact change in response. The importance of frontal alignment on the performance of knee joint replacements is well recognized (Jeffery, Morris et al. 1991). For example, a recent large scale study showed that excessive valgus and varus alignments are associated with substantially higher rates of failure (Fang, Ritter et al. 2009). Our sensitivity analysis suggests that internal tibia rotation is highly dependent on joint alignment when the limb is unloaded in swing and early stance. However, internal tibia rotation was relatively independent of loading during stance, with the greatest effect of alignment being on the mediolateral distribution of load across the tibiofemoral joint. A more equal distribution and lower pressure on the medial insert in the knee occurred with greater valgus alignment (Figure 36). These results are similar to experimental observations made when simulating gait on cadaveric specimens with varus and valgus alignments of the tibial insert (Werner, Ayers et al. 2005). We did predict a peak contact pressure on the posterior edge of the lateral insert at heel strike (Figure 36), though this effect may have arisen in part from the over-predict of lateral compartment loading in early stance (Figure 34).

There are a number of limitations to consider in our knee model. We represented the ligaments as spring elements, rather than deformable 3D representations that account

for spatial variations in strain. A one d.o.f. patellofemoral joint allowed for patella glide to occur as a result of patellar tendon stretch, but did not allow for medio-lateral translation and tilt. These choices were made for computational reasons since the simplified ligament and patellofemoral model could be more efficiently solved within the context of whole body movement. Increased knee model complexity can be easily incorporated into the framework, and is certainly warranted as improvements are made in the computational speed at which more complex soft tissue and contact models can be solved. We directly applied measured ground reaction forces within the gait simulation. Future studies will investigate the potential to use the elastic foundation framework to simulate foot-floor interactions within the context of whole body gait simulations. Finally, our framework relies on a static objective function to resolve muscle redundancy at every time step within the gait simulation. We used a popular objective function (sum of squared activations) that has been shown to reasonably predict muscle coordination in normal gait (Crowninshield and Brand 1981; Anderson and Pandy 2001). Our formulation over-predicted lateral compartment loading in early stance, which in part results from excess hamstring activity being recruited upon heel strike (Figure 33). Future studies may be able to better replicate experimental muscle recruitment patterns by incorporating objective functions that maximize agreement with EMG activities.

It is worth noting that generic musculoskeletal and ligament geometry were scaled to the subject and then used to simulate subject-specific gait dynamics. This scaling approach is often used in biomechanical simulation software (Delp, Anderson et al. 2007) and avoids the time consuming task of creating subject-specific musculoskeletal models from medical images. It is reassuring that this approach generated plausible estimates of

tibiofemoral contact forces, supporting the use of model scaling until more efficient approaches emerge for creating truly subject-specific musculoskeletal models. Posterior cruciate and collateral ligament forces were relatively low throughout the gait cycle, though stretch of these structures during swing did contribute to the over-prediction of the lateral and total tibiofemoral forces (Figure 36). Ligament stretch with knee flexion is highly dependent on the assumed ligament geometry, such that further work is needed to accurately characterize ligament origins, insertions, and wrapping about anatomical structures.

This study demonstrates the potential for co-simulating ligament, muscle and joint contact mechanics within the context of coordinated multi-joint movement. When applied to gait, model predictions of medial and total knee contact forces closely emulated experimental measures and exhibited a dependency on tibiofemoral alignment. We conclude that the new framework provides a powerful approach for virtually investigating how coupled physiological, surgical and design factors could affect joint mechanics and performance during functional tasks.

Chapter 6: The Influence of Cartilage Thickness on Simulated Tibiofemoral Contact Pressure Patterns during Normal Human Walking

6-1. Introduction

Recent studies have shown that a high knee adduction moment during gait was frequently observed among patients who have osteoarthritis in medial compartments(Hurwitz, Ryals et al. 2002). Further, medical image studies on healthy subjects showed that cartilage thickness increases with high knee loads (Andriacchi and Mundermann 2006). Seedhom et al. suggested that cartilage has homeostasis and this makes articular cartilage conditioned when high stresses or repetitive fatigue loads are applied (Seedhom 2006). In the literature, the possibility is reported that early cartilage thinning in anterior cruciate ligament (ACL)-deficient subjects can alter knee kinematics after ACL injury (Koo 2007). An investigation using three-dimensional knee cartilage models segmented from magnetic resonance images (MRI) of healthy subjects was performed and the result showed that the thickest cartilage region in the model was matched to the region of the load bearing areas between the femoral condyles and the tibia plateau, where they are in contact during the stance phase of the gait cycle near full extension (Andriacchi 2009).

Thus, the cartilage morphology, especially the cartilage thickness in the articular region, should be an essential concern in the study of the maintenance of healthy cartilage in the knee. This study has the goal of using a compuational model to begin to investigate

the relationship between cartilage thickness in the knee and tibiofemoral loading patterns during a walking gait cycle.

6-2. Methods

Modeling Framework

We used the knee model and co-simulation framework described in Chapter 5. However to simulate natural knee mechanics, we incoporated tibiofemoral cartilage surfaces segmented from a healthy adult female. High-resolution magnetic resonance (MR) images of the right knees of a healthy young adult male (age= 22 yr, height= 177.8 cm, mass=79 kg) were acquired under a protocol approved by the Wisconsin Health Science Institutional Review Board. A VIPR ATR sequence(Al Saleh, Hernandez et al. 2013) was used to obtain isotropic volumetric images with 0.3 mm cubic voxels. The images were manually segmented (MIMICS, Materialise Group, Leuven, Belgium) to obtain 3D geometries of the femoral cartilage, tibia plateau and patellar facet cartilage surfaces(Kaiser, Bradford et al. 2012)

Sensitivity of Model Predictions to Different Articular Cartilage Thicknesses

We repeated simulations of overground walking trials with an average gait speed of 1.25 m/s. We performed a sensitivity study analyzing the dependence of tibiofemoral loading patterns to variations in articular cartilage thickness between the femoral condyle and tibia plateau. Cartilage tissue was modeled as a linearly elastic isotropic material with an elastic modulus of 5 MPa, Poisson's ratio of 0.45, no damping, and a uniform thickness of 3 mm for each cartilage surface (Total thickness h is sum of tibia and femoral cartilage

thicknesses, assumed 6 mm in nominal case) (Blankevoort and Huiskes 1991a; Blankevoort, Kuiper et al. 1991b; Kim 1996; Pandy, Sasaki et al. 1997; Caruntu and Hefzy 2004; Shelburne, Pandy et al. 2004; Li, Park et al. 2005). The pressures were computed using nonlinear Kalker contact function (Equation 2) (An, Himeno et al. 1990; Blankevoort, Kuiper et al. 1991b) to find the contact pressures between the articulating cartilage.

$$p = \frac{-(1-\nu)E}{(1+\nu)(1-2\nu)} \ln\left[1-\frac{d}{h}\right] \quad \text{(Equation 2)}$$

Then, we made four more cartilage models to represent very thin, thin, thick and very thick cartilage models. In total, 2mm (very thin cartilage), 4mm (thin cartilage), 6mm (normal), 8mm (thick) and 10mm (very thick) cartilage models were built. The cartilage surface was the same in each case. We re-generated the dynamic gait simulations five times with five different cartilage models. The effect of cartilage thickness on loading was quantitatively evaluated by comparing the tibiofemoral contact force, pressure patterns and contact area at heel strike, and the time of the first and second peak of the tibiofemoral contact force. The top 5% peak pressure values were used to show the relationship between peak pressure in the simulation and thickness in the model instead of a peak pressure in the meshes. This is necessary to avoid error values from broken meshes during surface reconstruction. To calculate the top 5% peak pressures, the pressure values in the meshes in the contact area were collected first, and then the pressure values were sorted by the magnitudes of the pressures in the meshes. The meshes that contained the top 5% of high pressure were separated and averaged to calculate the top 5% peak pressures.

6-3. Results

Five dynamic simulations of one gait cycle took 600 minutes (120 minutes / simulation) to run. Five cases of contact forces including medial (Figure 37), lateral (Figure 38) and net (Figure 39) tibiofemoral forces during gait cycles were plotted.

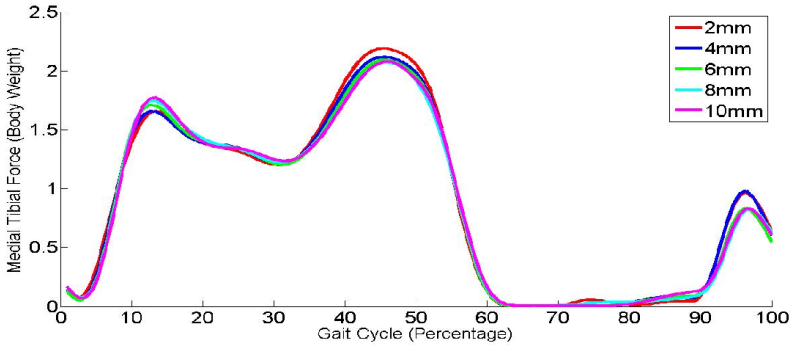

Figure 37. Simulated medial contact forces on articular cartilage of the right tibia plateau cartilage over five gait cycles. 2mm, 4mm, 6mm, 8mm and 10mm of total thickness (h) of cartilage models were simulated.

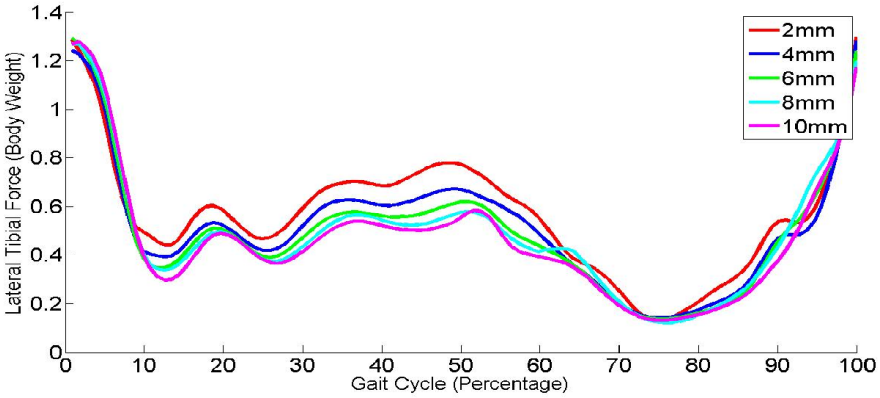

Figure 38. Simulated lateral contact forces on articular cartilage of the right tibia plateau cartilage over five gait cycles. 2mm, 4mm, 6mm, 8mm and 10mm of total thickness (h) of cartilage models were simulated.

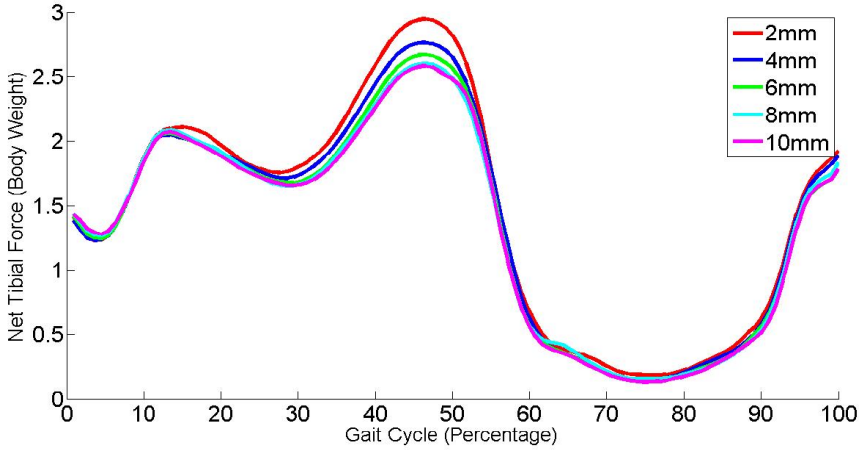

Figure 39. Simulated net contact forces on articular cartilage of the right tibia plateau cartilage over five gait cycles. 2mm, 4mm, 6mm, 8mm and 10mm of total thickness (h) of cartilage models were simulated.

The peak net tibiofemoral forces from the five gait simulations were plotted over total thicknesses (2mm, 4mm, 6mm, 8mm and 10mm) (Figure 40). (Figure 37), (Figure 38), (Figure 39) and (Figure 40) show that the tibiofemoral forces tend to increase as the cartilage gets thinner.

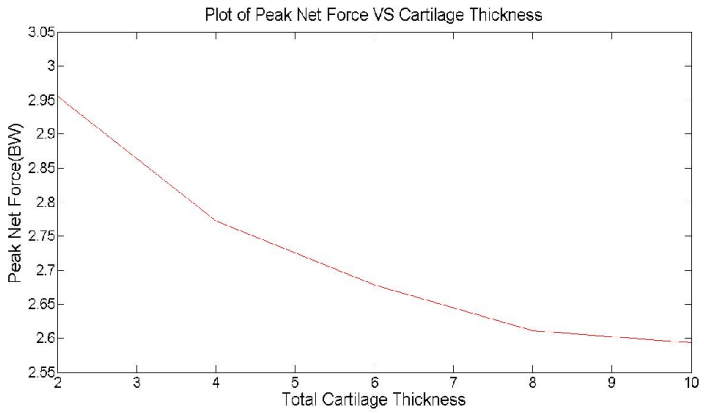

Figure 40. Plot of the peak net tibiofemoral forces from five gait simulations. 2mm, 4mm, 6mm, 8mm and 10mm of total thickness (h) of cartilage models were simulated.

Then pressure patterns at heel strikes, and the time of the first and second peaks of the tibiofemoral contact force using the five models were plotted (Figure 41). This shows that the tibiofemoral stress tends to increase and the contact area tends to decrease as the cartilage gets thinner.

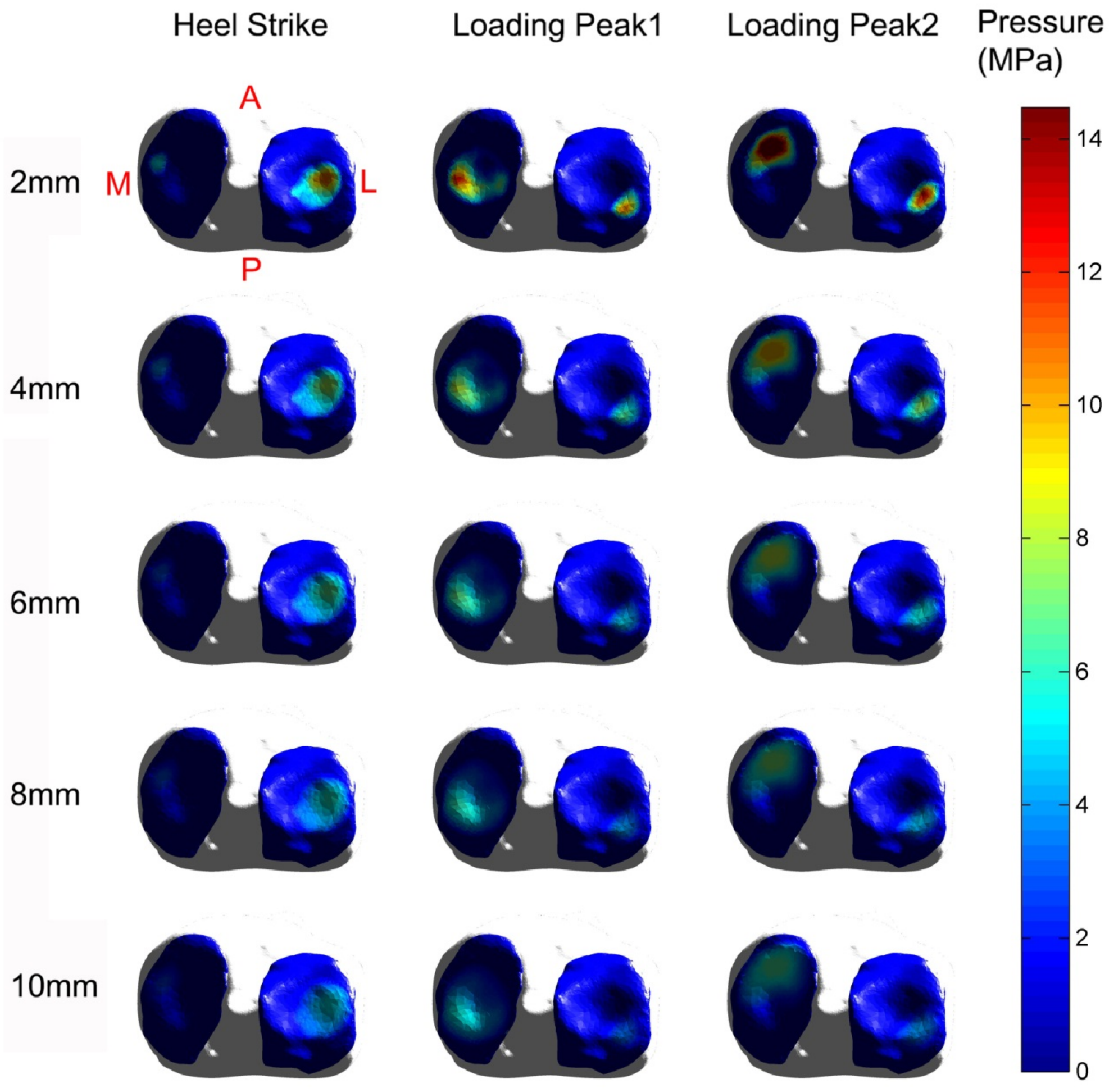

Figure 41. Simulated pressure on articular cartilage of the right tibia plateau cartilage over five gait cycles. 2mm, 4mm, 6mm, 8mm and 10mm of total thickness (h) of cartilage models were simulated.

The total tibiofemoral contact areas (Figure 42) and top 5% peak pressures (Figure 43) in the contact area at the moment of the peak net tibiofemoral forces from the five gait simulations were plotted over total thicknesses. (Figure 42) and (Figure 43) clearly showed the nonlinear relationship between the cartilage thickness and contact and the inverse nonlinear relationship between the thickness and pressure.

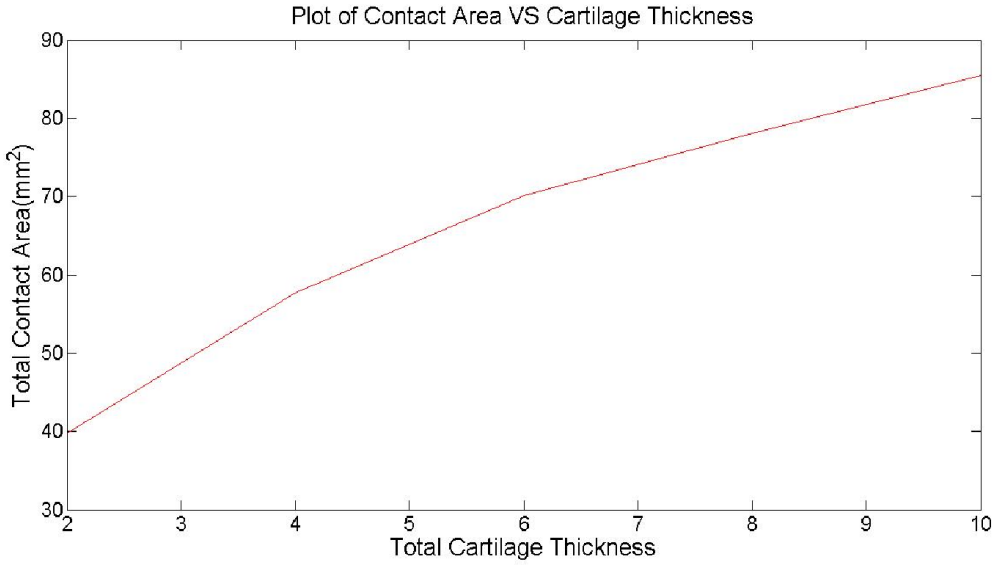

Figure 42. Plot of the total tibiofemoral contact areas at the peak loads from five gait simulations. 2mm, 4mm, 6mm, 8mm and 10mm of total thickness (h) of cartilage models were simulated.

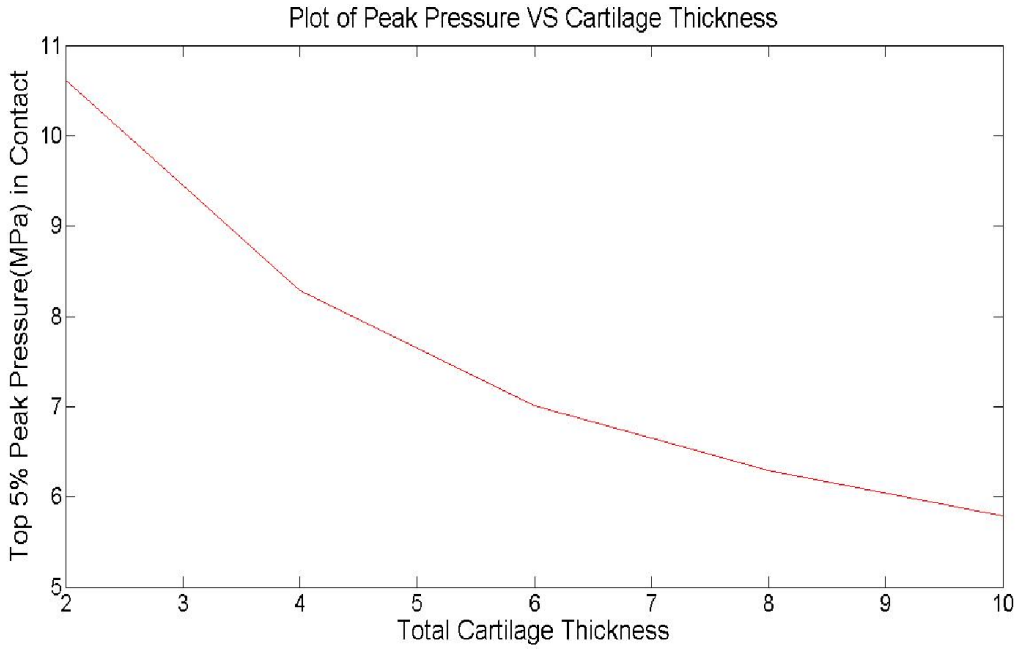

Figure 43. Plot of the peak pressures at the peak loads from five gait simulations. 2mm, 4mm, 6mm, 8mm and 10mm of total thickness (h) of cartilage models were simulated.

The lengths of aACL (Figure 44), asMCL (Figure 45) and LCL (Figure 46) in right knee during five cases of gait cycles were plotted to track the changes in the ligament lengths.

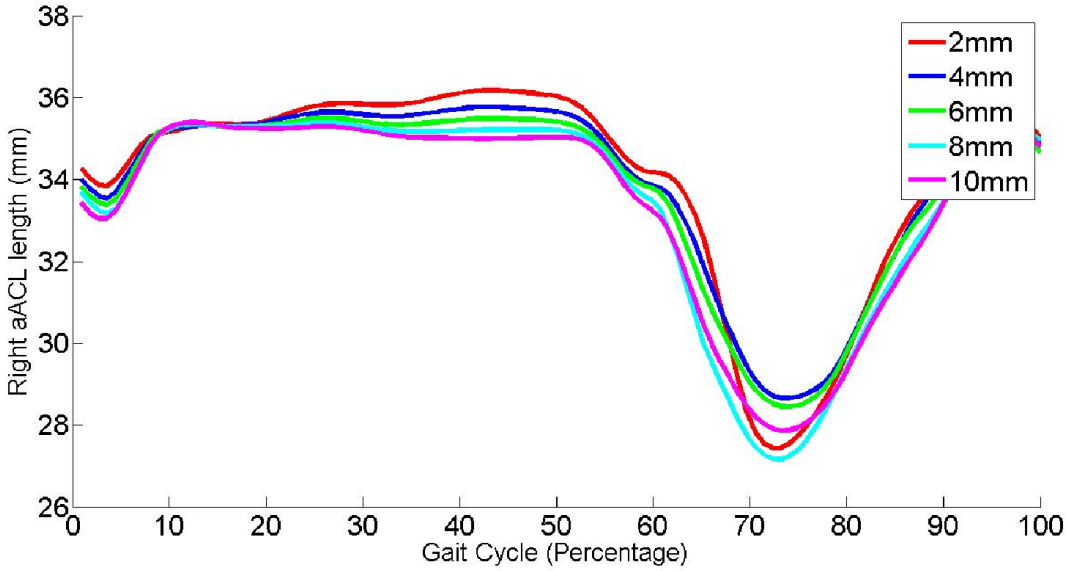

Figure 44. Simulated aACL lengths in the right knee over five gait cycles. 2mm, 4mm, 6mm, 8mm and 10mm of total thickness (h) of cartilage models were simulated.

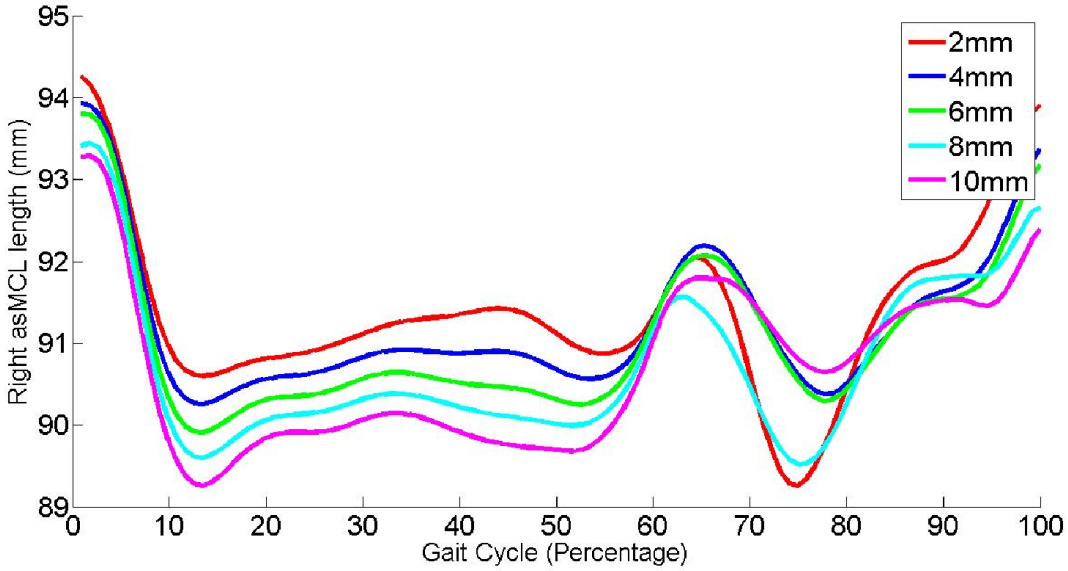

Figure 45. Simulated asMCL lengths in the right knee over five gait cycles. 2mm, 4mm, 6mm, 8mm and 10mm of total thickness (h) of cartilage models were simulated.

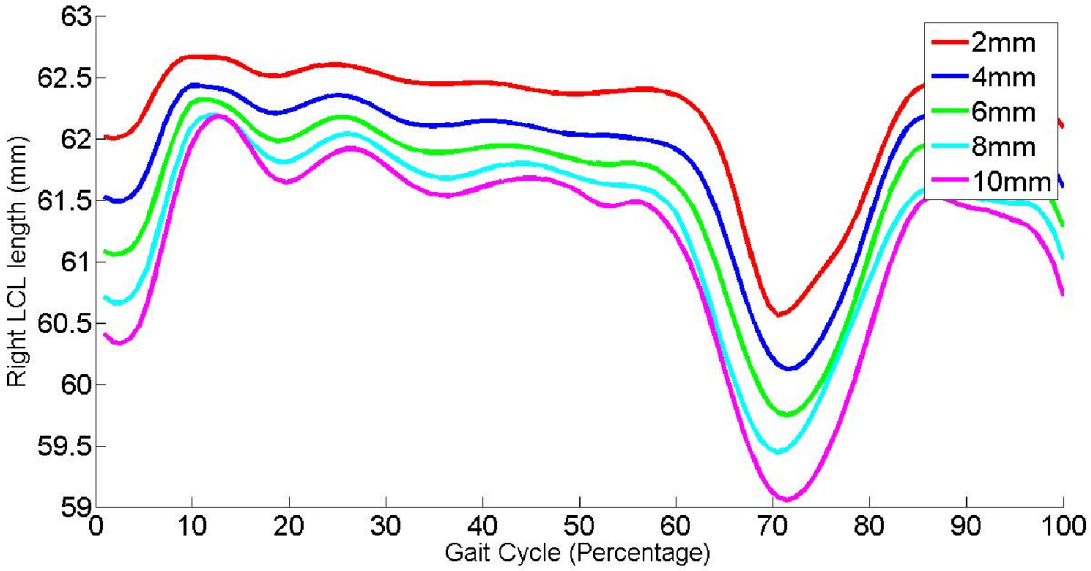

Figure 46. Simulated LCL lengths in the right knee over five gait cycles. 2mm, 4mm, 6mm, 8mm and 10mm of total thickness (h) of cartilage models were simulated.

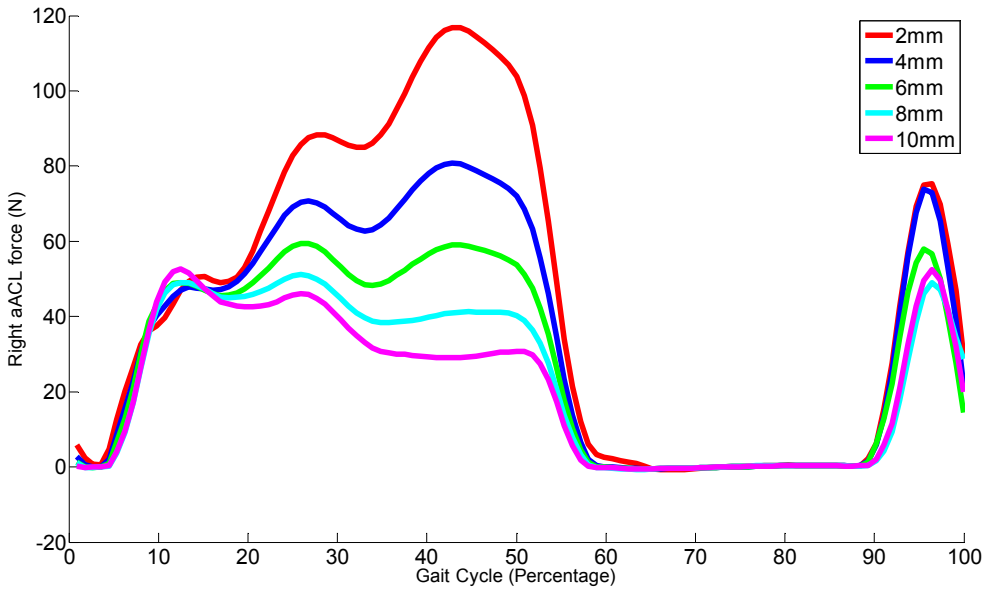

Figure 47. Simulated aACL forces in the right knee over five gait cycles. 2mm, 4mm, 6mm, 8mm and 10mm of total thickness (h) of cartilage models were simulated.

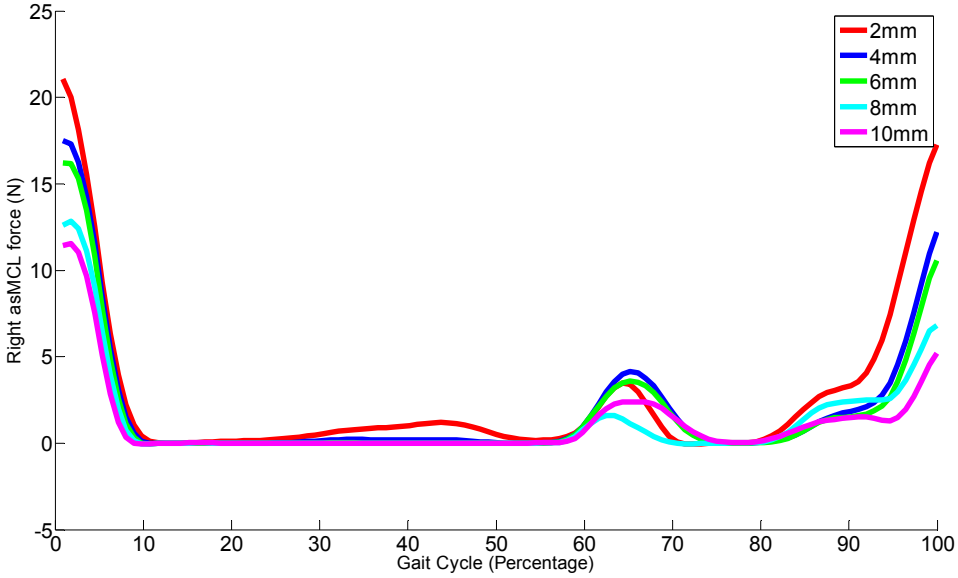

Figure 48. Simulated asMCL forces in the right knee over five gait cycles. 2mm, 4mm, 6mm, 8mm and 10mm of total thickness (h) of cartilage models were simulated.

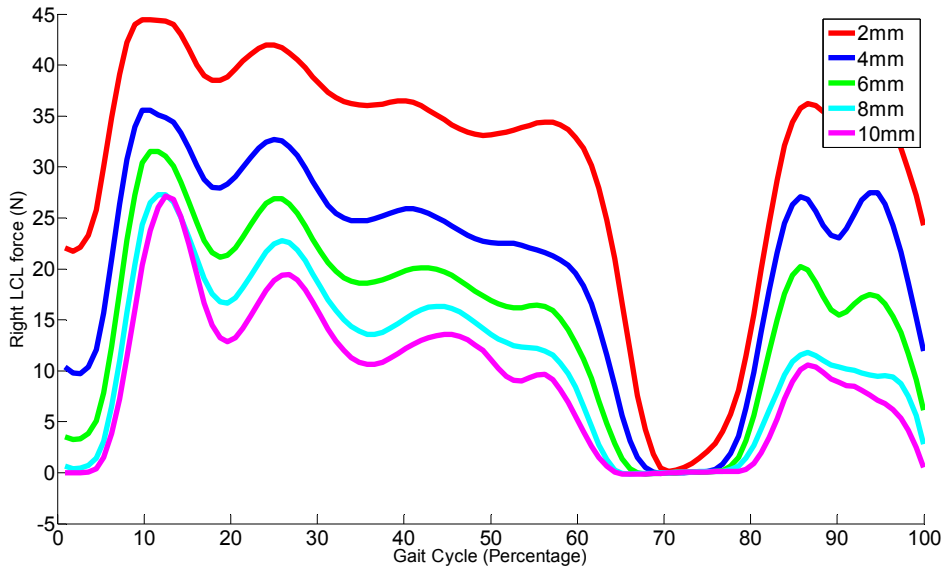

Figure 49. Simulated LCL forces in the right knee over five gait cycles. 2mm, 4mm, 6mm, 8mm and 10mm of total thickness (h) of cartilage models were simulated.

(Figure 47), (Figure 48)and (Figure 49) show that the ligament forces tend to increase due to the increasing of ligament lengths (Figure 44) (Figure 45) (Figure 46) as the cartilage gets thinner.

6-4. Discussion

The ratio between penetration depth d and total thickness h contributes to the pressure variation as a critical factor (Figure 50).

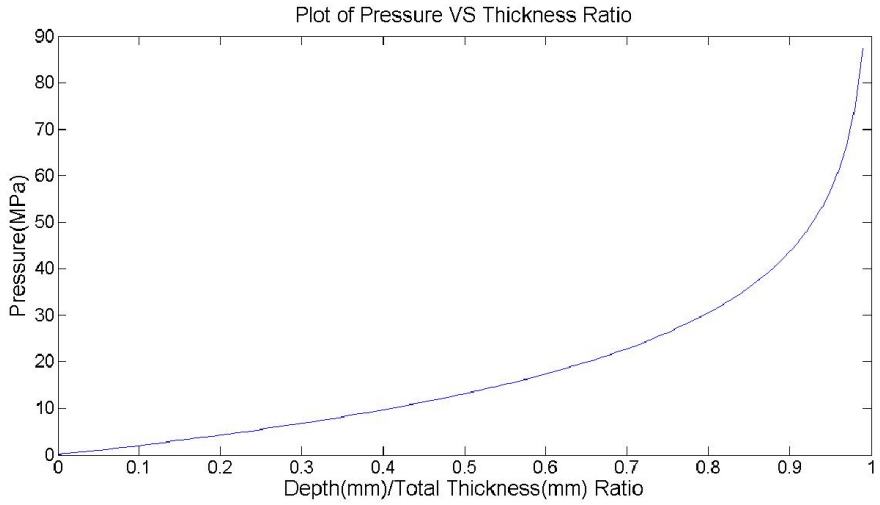

Figure 50. Plot of the pressure and the ratio between penetration depth and total thickness

Theoretically, when the total cartilage thickness gets thicker, the ratio relative to depth gets lower, while the ratio has a high value in thin cartilage (Figure 50)(Figure 51). This pattern was observed from the thickness sensitivity analysis models. (Figure 43) clearly showed the inverse nonlinear relationship between the cartilage thickness and pressure. The top 5% peak pressure at the max net load was increased as the cartilage got thinner. As a result, the contact area decreased and the ligament length increased due to this higher stress as the thickness got thinner (Figure 42). As a result, (Figure 37), (Figure 38) and (Figure 39) show that the tibiofemoral forces tend to increase due to the increasing of ligament forces (Figure 47), (Figure 48) and (Figure 49) as the cartilage gets thinner.

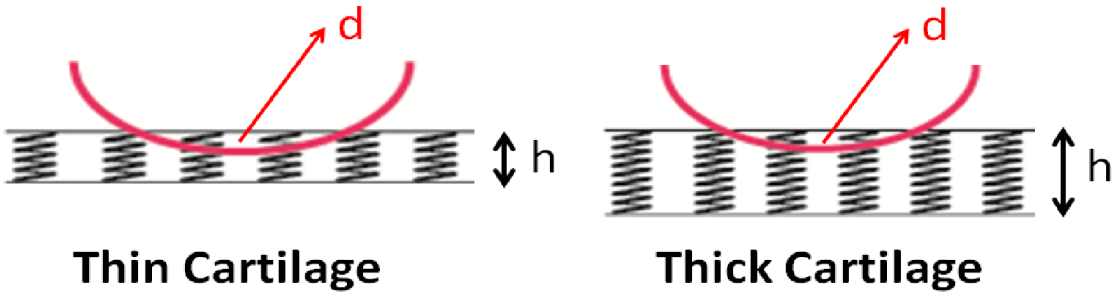

Figure 51. Schematic figure of thin and thick cartilage model

Chapter 7: Conclusions and Future Directions

7-1. Contributions of this research

7-1-1. Semi-automated segmentation of cartilage morphology from subject-specific MR images

Anatomically accurate cartilage modes are needed to characterize changes in morphology and to estimate the joint contact pressure distributions that can arise during functional tasks such as walking. We introduced a novel semi-automated segmentation approach to rapidly create cartilage thickness maps from MR images. The approach was shown capable of measuring thickness to within 0.4 mm, with accuracy improving for thicker cartilage. Before the development of this tool, manual segmentation had been used to construct 3D knee models from MR images. It had been taking a long time (more than 6 hours per model) to build a model from the MR images and the accuracy and repeatability had been questioned. The semi-automated process that we have developed will significantly decrease segmentation time while retaining precision and it is feasible to use for human knee cartilage segmentation. The overall time to make a 3D knee model from human knee MR images is less than an hour including pre-processing. This improved time performance is fast enough to be practical for clinical use.

7-1-2. Fast gait simulation using BVH and GPGPU

Simulation using anatomically detailed models can be resource-intensive with high-resolution cartilage meshes, due to the need to compute overlap of articulating

cartilage surfaces at every time step within a dynamic simulation. Using BVH and GPU, I showed the simulation time needed for collision detection can be expedited up to 10 times. This speedup further enables the viable simulation of cartilage contact loads within the context of musculoskeletal simulations of movement.

7-1-3. Thickness sensitivity analysis

The cartilage morphology, especially the cartilage thickness in the articular region, has been an essential concern in the study of the maintenance of healthy cartilage in the knee. This modeling study has provided insights into the relationship between the cartilage thickness in the knee and knee loading patterns during the gait cycle. Our results show that cartilage thinning may lead to higher force and pressure in articular knee surfaces and affect cartilage health.

7-2. Clinical Implications

7-2-1. MR image segmentation

The semi-automated segmentation method is applicable for morphological assessment of articular knee cartilage with quantitative MRI (qMRI). By constructing three-dimensional thickness models of cartilage, we can analyze cartilage health, and monitor progression and treatment response in knee osteoarthritis (OA), all with reasonable processing time, accuracy, and reproducibility. Thus, it has tremendous potential for large scale epidemiological studies of knee OA.

7-2-2. Gait simulation using high resolution cartilage geometries

Gait simulation can be used in the virtual design of joint replacements, and for investigating hypothesized relationships between soft tissue injury, cartilage loading patterns and osteoarthritis (Tashman, Collon et al. 2004). Also, this tool can be used as a pre-operative surgery simulator.

7-3. Future Work

7-3-1. Variable thickness knee cartilage model

In our gait simulations, we assumed that the cartilage thickness is uniform over the surface. But, quantitative MR study showed that the regions with cartilage-to-cartilage contact were significantly thicker than the regions without cartilage-to-cartilage contact (Andriacchi 2009). To have realistic outcomes, the gait simulation model should be advanced to contain regional variations in cartilage thickness.

7-3-2. Meniscus model

The meniscus was omitted in the knee model used in this study. The reason for this is that the meniscus is a highly flexible body, such that a straight forward discrete element analysis used for tibiofemoral cartilage is not appropriate. Future studies should consider the use of discretized multi-body models of the meniscus (Anderson 2009; Anderson, Iyer et al. 2010). Alternatively, one could use a finite element method (FEM) to represent meniscus deformation(Guess, Thiagarajan et al. 2010), though this would then involve

the ‘Combined Finite-Discrete Element Method’(Munjiza 2004) which would be even more resource intensive.

7-3-2. Monte Carlo simulation using cluster computing

Knee surgery such as ACL reconstruction may alter soft tissue material properties or structure, which may influence the cartilage loading patterns in the knee joint. To understand the major factors contributing to knee OA, simulations with various conditions of knee kinematics and variations in the soft tissue properties or structure (Ateshian, Soslowsky et al. 1991; Cohen, McCarthy et al. 1999; Cicuttini, Wluka et al. 2002) of the joint are necessary. Executing many Monte-Carlo gait simulations(Dubi 1999; Laz and Browne 2010) using various conditions of knee kinematics and variations in the soft tissue properties or structure over a multi-core CPU&GPU computer cluster system using parallel processing methods will have tremendous ability to analysis the interrelationship between surgical factors and clinical outcomes.

7-3-2. MR segmentation

1. Speed up the noise removal process

Speeding up the bone segmentation process would be very useful. At this time, the bone segmentation does not require much manual labor, but the processing time takes about 30 min.

2. Development of a tool for longitudinal studies

Implementation of an image registration tool could be considered. We will need to register images at two different time points assuming there is no shape change in bone

shape for now and generate pixel by pixel difference maps of cartilage thickness. However, this will be complex since bone shape changes rapidly as well following ACL reconstruction and with OA.

3. Develop a tool for measuring changes in bone marrow edema volume and meniscus shape and area.

These are very important factors following ACL reconstruction and in the progression of OA.

7-4. Conclusions

Impairment of the lower extremities can lead to substantial limitations for humans. Musculoskeletal knee models that anatomically-accurately represent the knee joint systems of individual patients could be used as a convenient investigation tool to simulate diverse treatment options and related clinical outcomes. However, the most difficult technical limitation to utilizing this kind of simulation is validation of the simulation result (Fregly, Besier et al. 2012), because *in vivo* contact and muscle forces are very hard to measure.

The emergence of the instrumented knee implant became an unparalleled method to measure *in vivo* contact forces. Instrumented knee implants with telemetric data transmission made the measurement of the tibiofemoral contact forces and moments from live human subjects viable. By comparing the result from the gait simulation of the knee replaced subject with the *in vivo* measured values from the Grand Challenge Competition (Fregly, Besier et al. 2012), which is open to the public, we could partially validate the system we developed. After comparing the result from simulated knee

replacement and *in vivo* measurements from the instrumented knee implant, the knee model was replaced with a natural knee. A 3D model segmented from high resolution MR images was used to construct the anatomically detailed knee geometry. However, the computation using high-resolution cartilage meshes of femoral cartilage and tibia plateau cartilage from the MR images were resource-intensive and hard to solve within a reasonable time.

Using a computation strategy such as bounding volume hierarchy (BVH) and general purpose graphic processing unit (GPGPU) parallel computing made the computation of the contact detection during the gait cycle 10 times faster. This speedup may make it viable to solve for cartilage contact loads within the context of musculoskeletal simulations of movement. Such an advance could be used in the virtual design of joint replacements, and for investigating hypothesized relationships between soft tissue injury, cartilage loading patterns and osteoarthritis (Tashman, Collon et al. 2004).

We used this tool for sensitivity analysis of the implant angle for knee replacement patients and also did sensitivity analysis for knees with various cartilage thicknesses. These virtual experimental studies have provided insights into the relationship between the configuration in the knee and knee loading patterns during the gait cycle and the maintenance of a healthy knee joint.

However, building a subject-specific knee model remains a challenging problem. Especially, the simulation designer spent too much time constructing the subject-specific knee models from the MR images due to the manual MR image segmentation process. After we developed the semi-automated knee cartilage segmentation method, the

modeling speed got dramatically faster. The repeatability of the segmentation algorithms on the same MR images was stable and the time performance on the human knee MR images was reasonably fast. Thus, it will be a practical solution for clinical use. The semi-automated segmentation method is applicable for morphological assessment of articular knee cartilage with quantitative MRI (qMRI). By constructing three-dimensional thickness models of cartilage, we can analyze cartilage health, and monitor progression and treatment response in knee osteoarthritis (OA), all with reasonable processing time, accuracy, and reproducibility. Thus, it has tremendous potential for large scale epidemiological studies of knee OA.

With all the computational frameworks that have been developed for this study, it is viable to investigate the interrelationship between knee cartilage morphology and knee kinematics. The technology developed here to explore the nature of human knee perfectly is still limited. But, these tools can provide a useful and convenient method for those who investigate diverse treatment options for knee problems and related clinical outcomes.

Chapter 8: References

Ahmed, M. N., S. M. Yamany, et al. (2002). "A modified fuzzy c-means algorithm for bias field estimation and segmentation of MRI data." Medical Imaging, IEEE Transactions on 21(3): 193-199.

Al Saleh, H., L. Hernandez, et al. (2013). "Rapid isotropic resolution cartilage assessment using radial alternating repetition time balanced steady-state free-precession imaging." J Magn Reson Imaging 22(10): 24425.

Almasi, G. S. and A. Gottlieb (1989). Highly parallel computing, Benjamin-Cummings Publishing Co., Inc.

An, K. N., S. Himeno, et al. (1990). "Pressure distribution on articular surfaces: application to joint stability evaluation." J Biomech 23(10): 1013-20.

Anderson, D. D., K. S. Iyer, et al. (2010). "Implementation of discrete element analysis for subject-specific, population-wide investigations of habitual contact stress exposure." J Appl Biomech 26(2): 215-23.

Anderson, D. D., K. S. Iyer, et al. (2010). "Implementation of discrete element analysis for subject-specific, population-wide investigations of habitual contact stress exposure." Journal of applied biomechanics 26(2): 215-23.

Anderson, D. D., Iyer, Krishna S. , Segal, Neil A. , Brown, Thomas D. (2009). Meniscal Modeling in a Discrete Element Analysis of the Knee. The 2009 Meeting of the American Society of Biomechanics. August 26-29, State College, PA.

Anderson, F. C. and M. G. Pandy (2001). "Dynamic optimization of human walking." J Biomech Eng 123(5): 381-90.

Anderson, F. C. and M. G. Pandy (2001). "Static and dynamic optimization solutions for gait are practically equivalent." J Biomech 34(2): 153-61.

Andriacchi, T. P. (2009). "Gait Mechanics Influence Healthy Cartilage Morphology and Osteoarthritis of the Knee." J Bone Joint Surg Am 91: 95-101.

Andriacchi, T. P., P. L. Briant, et al. (2006). "Rotational Changes at the Knee after ACL Injury Cause Cartilage Thinning." Clinical Orthopaedics and Related Research 442: 39-44 10.1097/01.blo.0000197079.26600.09.

Andriacchi, T. P. and C. O. Dyrby (2005). "Interactions between kinematics and loading during walking for the normal and ACL deficient knee." Journal of Biomechanics 38(2): 293-298.

Andriacchi, T. P. and A. Mundermann (2006). "The role of ambulatory mechanics in the initiation and progression of knee osteoarthritis." Curr Opin Rheumatol 18(5): 514-8.

Andriacchi, T. P., A. Mundermann, et al. (2004). "A framework for the in vivo pathomechanics of osteoarthritis at the knee." Ann Biomed Eng 32(3): 447-57.

Andriacchi, T. P., A. Mundermann, et al. (2004). "A framework for the in vivo pathomechanics of osteoarthritis at the knee." Annals of biomedical engineering 32(3): 447-57.

Appleyard, R. C., D. Burkhardt, et al. (2003). "Topographical analysis of the structural, biochemical and dynamic biomechanical properties of cartilage in an ovine model of osteoarthritis." Osteoarthritis Cartilage 11(1): 65-77.

Arnold, A. S., F. C. Anderson, et al. (2005). "Muscular contributions to hip and knee extension during the single limb stance phase of normal gait: a framework for investigating the causes of crouch gait." Journal of biomechanics 38(11): 2181-9.

Arnold, E. M., S. R. Ward, et al. (2010). "A model of the lower limb for analysis of human movement." Annals of biomedical engineering 38(2): 269-79.

Arnold, E. M., S. R. Ward, et al. (2010). "A model of the lower limb for analysis of human movement." Ann Biomed Eng 38(2): 269-79.

Ateshian, G. A., L. J. Soslowsky, et al. (1991). "Quantitation of articular surface topography and cartilage thickness in knee joints using stereophotogrammetry." J Biomech 24(8): 761-76.

Bach, B. R., Jr., S. Tradonsky, et al. (1998). "Arthroscopically assisted anterior cruciate ligament reconstruction using patellar tendon autograft. Five- to nine-year follow-up evaluation." Am J Sports Med 26(1): 20-9.

Bei, Y. (2004). "Multibody dynamic simulation of knee contact mechanics." Medical Engineering & Physics 26: 777–789.

Bei, Y. and B. J. Fregly (2004). "Multibody dynamic simulation of knee contact mechanics." Med Eng Phys 26(9): 777-89.

Bergen, G. v. d. (2004). Collision Detection in Interactive 3D Environments. San Francisco, Morgan Kaumann Publishers, An Imprint of Elsevier.

Beynnon, B. D., R. J. Johnson, et al. (2005). "Treatment of anterior cruciate ligament injuries, part 2." Am J Sports Med 33(11): 1751-67.

Blankevoort, L. and R. Huiskes (1991a). "Ligament-bone interaction in a three-dimensional model of the knee." J Biomech Eng 113(3): 263-9.

Blankevoort, L., J. H. Kuiper, et al. (1991b). "Articular contact in a three-dimensional model of the knee." J Biomech 24(11): 1019-31.

Bowers, M. E., N. Trinh, et al. (2008). "Quantitative MR imaging using "LiveWire" to measure tibiofemoral articular cartilage thickness." Osteoarthritis and Cartilage 16(10): 1167-1173.

Bullough, P. G., P. S. Yawitz, et al. (1985). "Topographical variations in the morphology and biochemistry of adult canine tibial plateau articular cartilage." J Orthop Res 3(1): 1-16.

Cabezas, M., A. Oliver, et al. (2011). "A review of atlas-based segmentation for magnetic resonance brain images." Comput Methods Programs Biomed 104(3): 25.

Canny, J. (1986). "A Computational Approach to Edge Detection." Pattern Analysis and Machine Intelligence, IEEE Transactions on PAMI-8(6): 679-698.

Caruntu, D. I. and M. S. Hefzy (2004). "3-D anatomically based dynamic modeling of the human knee to include tibio-femoral and patello-femoral joints." J Biomech Eng 126(1): 44-53.

Caselles, V., R. Kimmel, et al. (1997). "Geodesic Active Contours." International Journal of Computer Vision 22(1): 61-79.

Chaudhari, A. M., P. L. Briant, et al. (2008). "Knee Kinematics, Cartilage Morphology, and Osteoarthritis after ACL Injury." Med Sci Sports Exerc 40(2): 215-22.

Chen, Y. and G. Medioni (1991). Object modeling by registration of multiple range images. Robotics and Automation, 1991. Proceedings., 1991 IEEE International Conference on.

Choi, K. W., Negrut, D. , Thelen, D. G. (2013). "GPU-based algorithm for fast computation of cartilage contact patterns during simulations of movement." The ASME 2013 Summer Bioengineering Conference.

Cicuttini, F. M., A. E. Wluka, et al. (2002). "Compartment differences in knee cartilage volume in healthy adults." J Rheumatol 29(3): 554-6.

Clark, J. M. (1991). "Variation of collagen fiber alignment in a joint surface: a scanning electron microscope study of the tibial plateau in dog, rabbit, and man." J Orthop Res 9(2): 246-57.

Cohen, Z. A., D. M. McCarthy, et al. (1999). "Knee cartilage topography, thickness, and contact areas from MRI: in-vitro calibration and in-vivo measurements." Osteoarthritis Cartilage 7(1): 95-109.

Cootes, T. F., C. J. Taylor, et al. (1995). "Active shape models-their training and application." Comput. Vis. Image Underst. 61(1): 38-59.

Crowninshield, R. D. and R. A. Brand (1981). "A physiologically based criterion of muscle force prediction in locomotion." Journal of Biomechanics 14(11): 793-801.

D'Lima, D. D., C. P. Townsend, et al. (2005). "An implantable telemetry device to measure intra-articular tibial forces." Journal of biomechanics 38(2): 299-304.

Davies, H., A. Unwin, et al. (2004). "The posterolateral corner of the knee: Anatomy, biomechanics and management of injuries." Injury 35(1): 68-75.

Delp, S. L. (1990). Surgery simulation: a computer graphics system to analyze and design musculoskeletal reconstructions of the lower limb., PhD Dissertation, Stanford University.

Delp, S. L., F. C. Anderson, et al. (2007). "OpenSim: open-source software to create and analyze dynamic simulations of movement." IEEE Trans Biomed Eng 54(11): 1940-50.

Delp, S. L. and J. P. Loan (1995). "A graphics-based software system to develop and analyze models of musculoskeletal structures." Comput Biol Med 25(1): 21-34.

Delp, S. L., J. P. Loan, et al. (1990). "An interactive graphics-based model of the lower extremity to study orthopaedic surgical procedures." IEEE Transactions on Biomedical-Engineering 37(8): 757-67.

Dhaher, Y. Y., S. L. Delp, et al. (2000). "The use of basis functions in modelling joint articular surfaces: application to the knee joint." Journal of Biomechanics 33(7): 901-907.

Dhaher, Y. Y., T. H. Kwon, et al. (2010). "The effect of connective tissue material uncertainties on knee joint mechanics under isolated loading conditions." J Biomech 43(16): 3118-25.

Dubi, A. (1999). "Monte Carlo Applications in Systems Engineering." Wiley: p. 71-92.

Eckstein, F., F. Cicuttini, et al. (2006). "Magnetic resonance imaging (MRI) of articular cartilage in knee osteoarthritis (OA): morphological assessment." Osteoarthritis Cartilage 14(75): 19.

Eckstein, F., A. Gavazzeni, et al. (1996). "Determination of knee joint cartilage thickness using three-dimensional magnetic resonance chondro-crassometry (3D MR-CCM)." Magn Reson Med 36(2): 256-65.

Eckstein, F., M. Schnier, et al. (1998). "Accuracy of cartilage volume and thickness measurements with magnetic resonance imaging." Clin Orthop Relat Res 352: 137-48.

Edwards, A., A. M. Bull, et al. (2007). "The Attachments of the Fiber Bundles of the Posterior Cruciate Ligament: An Anatomic Study." Arthro: J Arthro and Rel Surg 23(3): 284-290.

Eggli, P. S., E. B. Hunziker, et al. (1988). "Quantitation of structural features characterizing weight- and less-weight-bearing regions in articular cartilage: a stereological analysis of medial femoral condyles in young adult rabbits." Anat Rec 222(3): 217-27.

Elaine N. Marieb, J. M., Patricia Brady Wilhelm (2008). Human Anatomy, Pearson Benjamin Cummings.

Fang, D. M., M. A. Ritter, et al. (2009). "Coronal alignment in total knee arthroplasty: just how important is it?" The Journal of arthroplasty 24(6 Suppl): 39-43.

Frank, C. B. and D. W. Jackson (1997). "The science of reconstruction of the anterior cruciate ligament." J Bone Joint Surg Am 79(10): 1556-76.

Fregly, B. J., T. F. Besier, et al. (2012). "Grand challenge competition to predict in vivo knee loads." J Orthop Res 30(4): 503-13.

Fregly, B. J., T. F. Besier, et al. (2012). "Grand challenge competition to predict in vivo knee loads." Journal of orthopaedic research : official publication of the Orthopaedic Research Society 30(4): 503-13.

Fripp, J., S. Crozier, et al. (2010). "Automatic segmentation and quantitative analysis of the articular cartilages from magnetic resonance images of the knee." IEEE Trans Med Imaging 29(1): 55-64.

Fu, F. H., C. H. Bennett, et al. (1999). "Current trends in anterior cruciate ligament reconstruction. Part 1: Biology and biomechanics of reconstruction." Am J Sports Med 27(6): 821-30.

Fu, F. H., C. H. Bennett, et al. (2000). "Current trends in anterior cruciate ligament reconstruction. Part II. Operative procedures and clinical correlations." Am J Sports Med 28(1): 124-30.

Gardiner, J. C., J. A. Weiss, et al. (2001). "Strain in the human medial collateral ligament during valgus loading of the knee." Clin Orthop Relat Res 391: 266-74.

Genda, E., N. Iwasaki, et al. (2001). "Normal hip joint contact pressure distribution in single-leg standing--effect of gender and anatomic parameters." J Biomech 34(7): 895-905.

Georgoulis, A. D., A. Papadonikolakis, et al. (2003). "Three-Dimensional Tibiofemoral Kinematics of the Anterior Cruciate Ligament-Deficient and Reconstructed Knee during Walking." The American Journal of Sports Medicine 31(1): 75-79.

Ghosh, S., Ries, M, Lane, N, Ghajar, C, Majumdar, S (2000). "Segmentation of high resolution articular cartilage MR images (Abstract)." Trans OrthopResSoc(ORS): 246.

Gottschalk, S. (1996). "OBBTree: A Hierarchical Structure for Rapid Interference Detection." Computer Graphics: 171-180.

Gougoutas, A. J., A. J. Wheaton, et al. (2004). "Cartilage volume quantification via Live Wire segmentation." Acad Radiol 11(12): 1389-95.

Grood, E. S. and W. J. Suntay (1983). "A joint coordinate system for the clinical description of three-dimensional motions: application to the knee." Journal of biomechanical engineering 105(2): 136-44.

Guess, T. M., G. Thiagarajan, et al. (2010). "A subject specific multibody model of the knee with menisci." Medical engineering & physics 32(5): 505-15.

Guess, T. M., G. Thiagarajan, et al. (2010). "A subject specific multibody model of the knee with menisci." Medical Engineering & Physics 32(5): 505-515.

Halloran, J. P., M. Ackermann, et al. (2010). "Concurrent musculoskeletal dynamics and finite element analysis predicts altered gait patterns to reduce foot tissue loading." Journal of biomechanics 43(14): 2810-5.

Halloran, J. P., S. K. Easley, et al. (2005). "Comparison of deformable and elastic foundation finite element simulations for predicting knee replacement mechanics." Journal of biomechanical engineering 127(5): 813-8.

Halloran, J. P., A. Erdemir, et al. (2009). "Adaptive surrogate modeling for efficient coupling of musculoskeletal control and tissue deformation models." Journal of biomechanical engineering 131(1): 011014.

Happee, R. (1994). "Inverse dynamic optimization including muscular dynamics, a new simulation method applied to goal directed movements." J Biomech 27(7): 953-60.

Hindmarsh, A. C., P. N. Brown, et al. (2005). "SUNDIALS: Suite of nonlinear and differential/algebraic equation solvers." ACM Trans. Math. Softw. 31(3): 363-396.

Hindmarsh, A. C., P. N. Brown, et al. (2005). "SUNDIALS: Suite of nonlinear and differential/algebraic equation solvers." Acm Transactions on Mathematical Software 31(3): 363-396.

Howell, S. M. and S. J. Barad (1995). "Knee extension and its relationship to the slope of the intercondylar roof. Implications for positioning the tibial tunnel in anterior cruciate ligament reconstructions." Am J Sports Med 23(3): 288-94.

Hurwitz, D. E., A. B. Ryals, et al. (2002). "The knee adduction moment during gait in subjects with knee osteoarthritis is more closely correlated with static alignment than radiographic disease severity, toe out angle and pain." J Orthop Res 20(1): 101-7.

Iwasaki, N., E. Genda, et al. (1998). "Biomechanical analysis of limited intercarpal fusion for the treatment of Kienbock's disease: a three-dimensional theoretical study." J Orthop Res 16(2): 256-63.

Jeffery, R. S., R. W. Morris, et al. (1991). "Coronal alignment after total knee replacement." The Journal of bone and joint surgery. British volume 73(5): 709-14.

Kaiser, J., R. Bradford, et al. (2012). "Measurement of tibiofemoral kinematics using highly accelerated 3D radial sampling." Magnetic Resonance in Medicine: n/a-n/a.

Kanamori, A., J. Zeminski, et al. (2002). "The effect of axial tibial torque on the function of the anterior cruciate ligament: a biomechanical study of a simulated pivot shift test." Arthroscopy 18(4): 394-8.

Kannus, P., J. Bergfeld, et al. (1991). "Injuries to the posterior cruciate ligament of the knee." Sports Med 12(2): 110-31.

Kauffmann, C., P. Gravel, et al. (2003). "Computer-aided method for quantification of cartilage thickness and volume changes using MRI: validation study using a synthetic model." IEEE Trans Biomed Eng 50(8): 978-88.

Kim, H. J., J. W. Fernandez, et al. (2009). "Evaluation of predicted knee-joint muscle forces during gait using an instrumented knee implant." J Orthop Res 27(10): 1326-31.

Kim, S. (1996). A three-dimensional dynamic musculoskeletal model of the human knee joint, University of Texas at Austin.

Kiviranta, I., J. Jurvelin, et al. (1987). "Weight bearing controls glycosaminoglycan concentration and articular cartilage thickness in the knee joints of young beagle dogs." Arthritis Rheum 30(7): 801-9.

Koo, S., Dyrby, CO, Andriacchi, TP (2007). Abnormal ambulation after ACL rupture affects knee articular cartilage spatial thinning pattern. Presented at the Annual Meeting of the Orthopaedic Research Society. San Diego, CA.

Koo, S., N. J. Giori, et al. (2009). "Accuracy of 3D cartilage models generated from MR images is dependent on cartilage thickness: laser scanner based validation of in vivo cartilage." Journal of biomechanical engineering 131(12): 121004.

Kshirsagar, A. A., P. J. Watson, et al. (1998). "Measurement of localized cartilage volume and thickness of human knee joints by computer analysis of three-dimensional magnetic resonance images." Invest Radiol 33(5): 289-99.

Kulowski, J. (1932). "FLEXION CONTRACTURE OF THE KNEE The Mechanics of the Muscular Contracture and the Turnbuckle Cast Method of Treatment; with a Review of Fifty-Five Cases." The Journal of Bone & Joint Surgery 14(3): 618-630.

Kurt, S. M., C. W. Jewett, et al. (2002). "Miniature specimen shear punch test for UHMWPE used in total joint replacements." Biomaterials 23(9): 1907-19.

LaPrade, R. F., T. V. Ly, et al. (2003). "The posterolateral attachments of the knee: a qualitative and quantitative morphologic analysis of the fibular collateral ligament, popliteus tendon, popliteofibular ligament, and lateral gastrocnemius tendon." The American journal of sports medicine 31(6): 854-60.

Lauterbach, C. (1981). "gProximity: Hierarchical GPU-based Operations for Collision and Distance Queries." EUROGRAPHICS.

Laz, P. J. and M. Browne (2010). "A review of probabilistic analysis in orthopaedic biomechanics." Proc Inst Mech Eng H 224(8): 927-43.

Li, G., J. M. Moses, et al. (2006). "Anterior cruciate ligament deficiency alters the in vivo motion of the tibiofemoral cartilage contact points in both the anteroposterior and mediolateral directions." J Bone Joint Surg Am 88(8): 1826-34.

Li, G., S. E. Park, et al. (2005). "The cartilage thickness distribution in the tibiofemoral joint and its correlation with cartilage-to-cartilage contact." Clin Biomech 20(7): 736-44.

Li, G. G., E.; Sakamoto, M.; Chao, EYS. (1994). "Surface Pressure distribution in Articular Joint under Static Load." Advances in Bioengineering, ASME. BED-Vol. 28: p. 139-140.

Li, X., D. Kuo, et al. (2011). "Cartilage in anterior cruciate ligament-reconstructed knees: MR imaging T1{rho} and T2--initial experience with 1-year follow-up." Radiology 258(2): 505-14.

Lim, J. S. (1990). Two-Dimensional Signal and Image Processing. Englewood Cliffs, NJ, Prentice Hall.

Lin, Y.-C. (2004). Experimental Evaluation of a Natrual Knee Contact Model Using Response Surface Optimization, Master Thesis, University of Florida.

Lin, Y.-C., J. P. Walter, et al. (2010). "Simultaneous prediction of muscle and contact forces in the knee during gait." Journal of Biomechanics 43(5): 945-952.

Lin, Y. C., J. Farr, et al. (2006). "Response surface optimization for joint contact model evaluation." J Appl Biomech 22(2): 120-30.

Little, C. B. and P. Ghosh (1997). "Variation in proteoglycan metabolism by articular chondrocytes in different joint regions is determined by post-natal mechanical loading." Osteoarthritis Cartilage 5(1): 49-62.

Liu-Ambrose, T. (2003). "The anterior cruciate ligament and functional stability of the knee joint." British Columbia Medical Journal 45(BCMJ No. 10): 495-499.

Liu, F., M. Kozanek, et al. (2010). "In vivo tibiofemoral cartilage deformation during the stance phase of gait." Journal of Biomechanics 43(4): 658-665.

Liu, F., B. Yue, et al. (2010). "Morphology of the medial collateral ligament of the knee." Journal of orthopaedic surgery and research 5: 69.

Loh, J. C., Y. Fukuda, et al. (2003). "Knee stability and graft function following anterior cruciate ligament reconstruction: Comparison between 11 o'clock and 10 o'clock femoral tunnel placement." Arthroscopy: The Journal of Arthroscopic & Related Surgery 19(3): 297-304.

Lohmander, L. S., P. M. Englund, et al. (2007). "The long-term consequence of anterior cruciate ligament and meniscus injuries: osteoarthritis." Am J Sports Med 35(10): 1756-69.

Louboutin, H., R. Debarge, et al. (2009). "Osteoarthritis in patients with anterior cruciate ligament rupture: a review of risk factors." Knee 16(4): 239-44.

Lynch, J. A., S. Zaim, et al. (2000). Cartilage segmentation of 3D MRI scans of the osteoarthritic knee combining user knowledge and active contours.

Markolf, K. L., A. Graff-Radford, et al. (1978). "In vivo knee stability. A quantitative assessment using an instrumented clinical testing apparatus." J Bone Joint Surg Am 60(5): 664-74.

Moller, T. (1997). "Fast, minimum storage ray-triangle intersection." J. Graph. Tools 2(1): 21-28.

Munjiza, A. A. (2004). The Combined Finite-Discrete Element Method. Hoboken, NJ, Wiley.

Neptune, R. (1999). "Optimization algorithm performance in determining optimal controls in human movement analyses." Journal of Biomechanical Engineering 121: 249-252.

Nock, R. and F. Nielsen (2006). "On weighting clustering." Pattern Analysis and Machine Intelligence, IEEE Transactions on 28(8): 1223-1235.

Otto, D. (1998). "Five-Year Results of Single-Incision Arthroscopic Anterior Cruciate Ligament Reconstruction with Patellar Tendon Autograft." American Journal of Sports Medicine 26(2).

Pandy, M. G., K. Sasaki, et al. (1997). "A Three-Dimensional Musculoskeletal Model of the Human Knee Joint. Part 1: Theoretical Construction." Computer Methods in Biomechanics and Biomedical Engineering 1(2): 87-108.

Parker, J. R. (1997). Algorithms for Image Processing and Computer Vision. New York, NY, John Wiley & Sons, Inc.

Peterfy, C. G., C. F. van Dijke, et al. (1994). "Quantification of articular cartilage in the knee with pulsed saturation transfer subtraction and fat-suppressed MR imaging: optimization and validation." Radiology 192(2): 485-91.

Petersen, W. M. D. and T. M. D. Zantop (2007). "Anatomy of the Anterior Cruciate Ligament with Regard to Its Two Bundles." Clin Orthop Relat Res.

Piazza, S. J. and S. L. Delp (2001). "Three-Dimensional Dynamic Simulation of Total Knee Replacement Motion During a Step-Up Task." Journal of Biomechanical Engineering 123: 599-606.

Piplani, M. A., D. G. Disler, et al. (1996). "Articular cartilage volume in the knee: semiautomated determination from three-dimensional reformations of MR images." Radiology 198(3): 855-9.

Quinn, T. M., E. B. Hunziker, et al. (2005). "Variation of cell and matrix morphologies in articular cartilage among locations in the adult human knee." Osteoarthritis Cartilage 13(8): 672-8.

S. Gottschalk, M. C. L., D. Manocha (1996). "OBBTree: A Hierarchical Structure for Rapid Interference Detection." Computer Graphics, Vol. 30, No. Annual Conference Series. (1996), pp. 171-180 Key: citeulike:567553.

Schmidl, H. (2004). "CAB: Fast Update of OBB Trees for Collision Detection between Articulated Bodies." Graphics Tools 9, 2 (2004), 1–9. .

Seedhom, B. B. (2006). "Conditioning of cartilage during normal activities is an important factor in the development of osteoarthritis." Rheumatology 45(2): 146-9.

Seireg, A. and Arvikar (1975). "The prediction of muscular lad sharing and joint forces in the lower extremities during walking." Journal of biomechanics 8(2): 89-102.

Shakoor, N. and K. Moisio (2004). "A biomechanical approach to musculoskeletal disease." Best Pract Res Clin Rheumatol 18(2): 173-86.

Shao, Q., T. D. MacLeod, et al. (2011). "Estimation of ligament loading and anterior tibial translation in healthy and ACL-deficient knees during gait and the influence of increasing tibial slope using EMG-driven approach." Annals of biomedical engineering 39(1): 110-21.

Shelburne, K. B., M. G. Pandy, et al. (2004). "Pattern of anterior cruciate ligament force in normal walking." J Biomech 37(6): 797-805.

Shelburne, K. B., M. R. Torry, et al. (2005). "Effect of muscle compensation on knee instability during ACL-deficient gait." Medicine and science in sports and exercise 37(4): 642-8.

Shelburne, K. B., M. R. Torry, et al. (2005). "Muscle, ligament, and joint-contact forces at the knee during walking." Medicine and science in sports and exercise 37(11): 1948-56.

Shelburne, K. B., M. R. Torry, et al. (2006). "Contributions of muscles, ligaments, and the ground-reaction force to tibiofemoral joint loading during normal gait." J Orthop Res 24(10): 1983-90.

Shelburne, K. B., M. R. Torry, et al. (2006). "Contributions of muscles, ligaments, and the ground reaction force to tibiofemoral joint loading during normal gait." J Orthop Research 24(10): 1983-1990.

Shin, C. S., A. M. Chaudhari, et al. (2007). "The influence of deceleration forces on ACL strain during single-leg landing: a simulation study." J Biomech 40(5): 1145-52.

Shoemaker, S. C. and K. L. Markolf (1982). "In vivo rotatory knee stability. Ligamentous and muscular contributions." J Bone Joint Surg Am 64(2): 208-16.

Solloway, S., C. E. Hutchinson, et al. (1997). "The use of active shape models for making thickness measurements of articular cartilage from MR images." Magn Reson Med 37(6): 943-52.

Spindler, K. P., T. A. Warren, et al. (2005). "Clinical outcome at a minimum of five years after reconstruction of the anterior cruciate ligament." J Bone Joint Surg Am 87(8): 1673-9.

Stammberger, T., F. Eckstein, et al. (1999). "Determination of 3D cartilage thickness data from MR imaging: computational method and reproducibility in the living." Magn Reson Med 41(3): 529-36.

Stammberger, T., F. Eckstein, et al. (1999). "Interobserver reproducibility of quantitative cartilage measurements: comparison of B-spline snakes and manual segmentation." Magn Reson Imaging 17(7): 1033-42.

Stehling, C., T. Baum, et al. (2011). "A novel fast knee cartilage segmentation technique for T2 measurements at MR imaging – data from the Osteoarthritis Initiative." Osteoarthritis and Cartilage 19(8): 984-989.

Steines, D., Cheng, C, Wong, A, Berger, F, Napel, S, and L. P. (2000). Segmentation of osteoarthritic femoral cartilage from MR images. Proceedings of Computer Assisted Radiology and Surgery, 14th International Congress: 303-8.

Stergiou, N., S. Ristanis, et al. (2007). "Tibial rotation in anterior cruciate ligament (ACL)-deficient and ACL-reconstructed knees: a theoretical proposition for the development of osteoarthritis." Sports Med 37(7): 601-13.

Sugita, T. and A. A. Amis (2001). "Anatomic and biomechanical study of the lateral collateral and popliteofibular ligaments." The American journal of sports medicine 29(4): 466-72.

Tamez-Pena, J. G., J. Farber, et al. (2012). "Unsupervised Segmentation and Quantification of Anatomical Knee Features: Data From the Osteoarthritis Initiative." Biomedical Engineering, IEEE Transactions on 59(4): 1177-1186.

Tashman, S., D. Collon, et al. (2004). "Abnormal rotational knee motion during running after anterior cruciate ligament reconstruction." Am J Sports Med 32(4): 975-83.

Tashman, S., S. Kopf, et al. (2008). "The Kinematic Basis of ACL Reconstruction." Oper Tech Sports Med 16(3): 116-118.

Taylor, W. R., M. O. Heller, et al. (2004). "Tibio-femoral loading during human gait and stair climbing." Journal of orthopaedic research : official publication of the Orthopaedic Research Society 22(3): 625-32.

Thelen, D. G. (2003). "Adjustment of muscle mechanics model parameters to simulate dynamic contractions in older adults." J Biomech Eng 125(1): 70-7.

Thelen, D. G. and F. C. Anderson (2006). "Using computed muscle control to generate forward dynamic simulations of human walking from experimental data." J Biomech 39(6): 1107-15.

Thelen, D. G., F. C. Anderson, et al. (2003). "Generating dynamic simulations of movement using computed muscle control." Journal of Biomechanics 36(3): 321-328.

Thelen, D. G., F. C. Anderson, et al. (2003). "Generating dynamic simulations of movement using computed muscle control." J Biomech 36(3): 321-8.

Thelen, D. G., K. W. Choi, et al. (2014). "Co-Simulation of Neuromuscular Dynamics and Knee Mechanics during Human Walking." J Biomech Eng 1(10): 4026358.

Thelen, D. G., K. W. Choi, et al. (2014). "Co-Simulation of Neuromuscular Dynamics and Knee Mechanics during Human Walking." Journal of biomechanical engineering.

Volokh, K. Y., E. Y. Chao, et al. (2007). "On foundations of discrete element analysis of contact in diarthrodial joints." Mol Cell Biomech 4(2): 67-73.

Werner, F. W., D. C. Ayers, et al. (2005). "The effect of valgus/varus malalignment on load distribution in total knee replacements." Journal of biomechanics 38(2): 349-55.

Williams, A., S. Barrus, et al. (2005). An efficient and robust ray-box intersection algorithm. ACM SIGGRAPH 2005 Courses. Los Angeles, California, ACM: 9.

Wilson, D. and J. O'Connor (1997). "A three-dimensional geometric model of the knee for the study of joint forces in gait." Gait & Posture.

Wilson, D. R., J. D. Feikes, et al. (1998). "Ligaments and articular contact guide passive knee flexion." Journal of biomechanics 31(12): 1127-36.

Yamaguchi, G. T. and F. E. Zajac (1989). "A planar model of the knee joint to characterize the knee extensor mechanism." Journal of Biomechanics 22: 1-10.

Yushkevich, P. A., J. Piven, et al. (2006). "User-guided 3D active contour segmentation of anatomical structures: significantly improved efficiency and reliability." Neuroimage 31(3): 1116-28.